This is a preprint, the final version is subject to change, of the American Mineralogist (MSA)
Cite as Authors (Year) Title. American Mineralogist, in press.
(DOI will not work until issue is live.) DOI: http://dx.doi.org/10.2138/am-2017-5970

Revision 2

Hydrothermal alteration of monazite-(Ce) and chevkinite-(Ce) from the Sin Quyen Fe-Cu-LREE-Au deposit, northwestern Vietnam

Xiao-Chun Li[a], Mei-Fu Zhou[a*]

a, Department of Earth Sciences, The University of Hong Kong, Hong Kong SAR, China

*Corresponding author. E-mail:mfzhou@hku.hk; Phone: (+852) 2857 8251

This is a preprint, the final version is subject to change, of the American Mineralogist (MSA)
Cite as Authors (Year) Title. American Mineralogist, in press.
(DOI will not work until issue is live.) DOI: http://dx.doi.org/10.2138/am-2017-5970

ABSTRACT

The Sin Quyen deposit in northwestern Vietnam is composed of Fe-Cu-LREE-Au ore bodies hosted in Proterozoic metapelite. There are massive and banded replacement ores with variable amounts of monazite-(Ce) and chevkinite-(Ce) crystals, which have undergone fluid-induced alteration. Monazite-(Ce) and chevkinite-(Ce) were deposited from high-temperature fluids in the early ore-forming stage, but became thermodynamically unstable, and thus were altered to other phases in later ore-forming stages. The alteration of monazite-(Ce) formed a three-layered corona texture, which commonly has relict monazite-(Ce) in the core, newly-formed fluorapatite in the mantle, and newly-formed allanite-(Ce) in the rim. In some cases, the original monazite-(Ce) was completely consumed, forming a core of polygonal fluorapatite crystals rimmed by allanite-(Ce) crystals. The formation of allanite-(Ce) and fluorapatite at the expense of monazite-(Ce) indicates that the later-stage fluids had high Ca/Na ratios and relatively low temperatures. Chevkinite-(Ce) was variably replaced by an assemblage of allanite-(Ce) + aeschynite-(Ce) ± bastnäsite-(Ce) ± columbite-(Fe) ± ilmenite. The replacement of chevkinite-(Ce) by mainly allanite-(Ce) and aeschynite-(Ce) required low-temperature, Ca-, LREE-, and Nb-rich metasomatic fluids, probably with relatively low f_{O2}.

Mass balance calculations were made to investigate the hydrothermal element mobility. It is assumed that Th was immobile during the alteration process of monazite-(Ce). Light (and middle) REE from La to Tb, U, As and Ge were variably lost relative to Th, while heavy REE from Dy to Lu, HFSE (e.g., Nb, Ta, Zr and Hf) and Sr were variably gained relative to Th. Regarding the alteration of chevkinite-(Ce), some major elements in chevkinite-(Ce), such as Ti, La, and Ce, were obviously removed from the system during alteration, whereas Ca, Al, Nb, U, and HREE were needed to be variably supplied by the metasomatic fluids. Concerning the hydrothermal mobility of trace elements, previous studies demonstrated that REE and HFSE can be commonly reserved in the system during alteration, consistent with the traditionally assumed immobile nature of these elements. In contrast, this study shows that REE and HFSE can be mobilized on at least the hundreds of micrometers scale.

This may be related to the high flux and strong chemical reactivity of the metasomatic fluids.

Key words: monazite, chevkinite, alteration, element mobility, Sin Quyen

INTRODUCTION

Accessory minerals are significant carriers of rare earth elements (REE), high-field strength elements (HFSE, e.g., Ti, Nb and Ta), and actinides (Th and U). It has been widely documented that these minerals may experience hydrothermal alteration, during which new mineral assemblages can be formed and complex compositional variations can be produced (e.g., Poitrasson et al., 1996, 2002; Smith et al., 1999; Geisler et al., 2007; Seydoux-Guillaume et al., 2012; Li et al., 2015). It is important to understand element mobility during fluid/mineral interaction, because it can help to determine the availability of elements, especially rare metals, to hydrothermal fluid and thus allow for the mineralizing potential of the fluid to be estimated. In addition, REE and HFSE have been widely used to trace petrological processes and geodynamic environments, so it is necessary to have a proper understanding of the possible effects of alteration before geochemical tracing is attempted.

Over the past two decades, many experimental studies of the hydrothermal alteration of accessory minerals have shown that the alteration products of accessory minerals depend on the temperature, pressure, texture, and composition of the host rocks, and the composition of metasomatic fluids (e.g., Geisler et al., 2001; Harlov et al., 2005, 2011; Budzyń et al., 2011; Richard et al., 2015). Therefore, the alteration of accessory minerals may bear important information on the evolutionary history of their host rocks.

Monazite [(Ce,LREE)PO_4] is a common accessory mineral in silica-rich, Ca-poor rocks (e.g., Bea, 1996; Forster, 1998), and typically hosts a significant amount of light REE (LREE, elements from La to Eu) and Th. The chevkinite-group minerals [$(REE,Ca)_4Fe^{2+}(Fe^{2+},Fe^{3+},Ti)_2Ti_2(Si_2O_7)_2O_8$] occur in a diversity of igneous,

metamorphic and metasomatic rocks, and are most common in alkaline to peralkaline silica-oversaturated felsic rocks (Macdonald and Belkin, 2002; Macdonald et al., 2009). They typically have high concentrations of LREE and HFSE (Nb and Ti). Hydrothermal alteration of monazite and chevkinite-group minerals has been documented to be widespread in magmatic and metamorphic rocks (e.g., Poitrasson et al., 1996; Finger et al. 1998; Broska et al., 2005; Rasmussen and Muhling, 2007; Upadhyay and Pruseth, 2012; Macdonald et al., 2015a and references therein). In fact, monazite and chevkinite-group minerals can also be formed during hydrothermal mineralization process. Such a process is commonly associated with high fluid fluxes with varied fluid compositions, which may lead to complex alteration of accessory minerals. However, there are few studies concerning the alteration of monazite or chevkinite-group minerals from hydrothermal deposits.

The Sin Quyen mine in northwestern Vietnam is a LREE-rich IOCG-type deposit (Fig. 1; McLean, 2001). In this deposit, the LREE are hosted mainly in allanite-(Ce) [$(Ca,REE)_2(Fe,Al)_3(SiO_4)_3(OH)$], and there are also subordinate proportions of monazite-(Ce) and chevkinite-(Ce). Monazite-(Ce) and chevkinite-(Ce) were formed in the relatively early mineralization stage, and they were altered by later-stage ore-forming fluids. The alteration products from monazite-(Ce) and chevkinite-(Ce) are very complex, and some products have not been documented in previous studies. In this study, we present textural and compositional features of monazite-(Ce), chevkinite-(Ce) and their corresponding alteration products. On this basis, the nature of the fluids that induced the alteration of monazite-(Ce) and chevkinite-(Ce) is discussed. Furthermore, mass balance calculations are made to investigate the mobility of elements, especially REE and HFSE, during the alteration process.

DEPOSIT GEOLOGY

In northwestern Vietnam, a Proterozoic metamorphic complex widely occurs (Fig. 1). The protoliths of the metamorphic complex include Archean to Paleoproterozoic granitoids and Paleoproterozoic to Neoproterozoic sedimentary rocks. These rocks have been metamorphosed from greenschist to amphibolite facies.

The metamorphic complex is intruded by Neoproterozoic to Mesozoic plutons, and is unconformably covered by the Paleozoic-early Triassic sedimentary rocks (Fig. 1). The Sin Quyen deposit is hosted by the Proterozoic metamorphic complex. In the Sin Quyen deposit, economic mineralization occurs in an elongate, northwest-trending zone, which has a width of 150 to 300 m, a length of approximately 2.5 km, and a depth that varies between 200 and 600 m (Fig. 2a). The mining district is divided into two parts by the Ngoi Phat River, namely the eastern district and the western district. Exploration in the 1990s showed that this deposit contains 52.8 Mt ore @ 0.91 wt.% Cu, 0.7 wt.% LREE (La, Ce, Pr and Nd), and 0.44 g/t Au (McLean, 2001). The ores occur mainly as massive or banded replacement bodies hosted in mica schist and locally marble (Figs. 2b and 3a). The occurrence of the ore bodies is controlled mainly by NW-striking faults or shear zones. The ores have experienced variable degrees of post-ore deformation, but the main ore and gangue mineral assemblages and textures have been well-preserved.

Three main stages of alteration and mineralization are identified in the Sin Quyen deposit: (I) pre-ore Na-(Fe) alteration; (II) Ca-(K) alteration and associated Fe-LREE mineralization; and (III) Cu-Au mineralization (Zhou et al., 2014; Li, 2016). The pre-ore Na-(Fe) alteration typically involves replacement of the mica schist by albite (Figs. 3b, c and d). The albite alteration appears to have been very intense close to the ore bodies, forming “albitite” veins or masses less than 1 meter away from the economic mineralization (Figs. 2b and 3b), but the alteration intensity decreases with distance from the ore bodies. Minor amounts of rutile, magnetite, monazite-(Ce), and chevkinite-(Ce) were formed together with albite in this stage.

The Na-(Fe) alteration was superimposed by Ca-(K) alteration and associated Fe-LREE mineralization. The Ca-(K) alteration is characterized by the formation of amphibole and lesser amounts of fluorapatite and biotite (Figs. 3e and f). The Fe mineralization is represented by abundant magnetite, and the LREE mineralization is characterized by abundant allanite-(Ce). Magnetite and allanite-(Ce) occur as either single crystals or aggregates in close association with amphibole, fluorapatite, and biotite (Figs. 3e and f). It is notable that most allanite-(Ce) crystals have experienced

alteration, forming dark rims in BSE images (Figs. 3f and g). The dark rims have variable thicknesses, and their boundaries with the bright cores are commonly sharp and irregular. The interiors of a few allanite-(Ce) crystals may also contain some dark patches. Minor amounts of Ti-, Nb-, and U-bearing minerals, such as ilmenite [$FeTiO_3$] columbite ($FeNb_2O_6$), pyrochlore [$(Na,Ca)_2Nb_2O_6(OH,F)$], aeschynite [$(Ce,Ca)(Ti,Nb)_2(O,OH)_6$], uraninite (UO_2), and samarskite [$(Y,Fe,U)(Nb,Ta)_5O_4$], were also formed in this stage (Fig. 3h).

The following Cu-Au mineralization is characterized by the formation of abundant sulfide minerals, chalcopyrite, pyrrhotite, pyrite, and cubanite. Gold is uniformly fine-grained and associated with sulfide minerals. The gangue minerals in this stage are mainly biotite and quartz.

Hydrothermal monazite-(Ce) and hydrothermal zircon have U-Pb ages of 836 ± 18 and 841 ± 12 Ma, respectively, which represents the timing of the mineralization at the Sin Quyen deposit (Li, 2016). Based on alteration mineralogy and isotopic compositions, it is proposed that the mineralization has a close genetic association with magmatic-hydrothermal fluids exsolved from Neoproterozoic subduction-related magmatic intrusions (Li, 2016).

SAMPLING AND ANALYTICAL METHODS

We collected twelve monazite-(Ce)- and chevkinite-(Ce)-bearing samples from the western mining district, including ten ore samples and two albitite samples. Among the ten ore samples, eight were collected from three separated ore bodies, and the remaining two were collected from the ore piles. The albitite samples were collected from the alteration halos adjacent to the ore bodies. The main features of the investigated samples are listed in Table 1.

Polished sections of each sample were investigated using petrographic and metallographic microscopes, and were further examined using the back-scattered electron (BSE) mode on a Hitachi S3400N VP scanning electron microprobe (SEM) (The University of Hong Kong), using a 10 μm electron beam at an accelerating voltage of 20 kV.

The major element contents of the minerals were analyzed using a JEOL JXA-8100 electron microprobe (EMP) at the State Key Laboratory for Mineral Deposits Research, Nanjing University. The analyses were performed using a 20 kV accelerating voltage and a 20 nA beam current. The beam spot diameter was set at 1 or 2 μm. The analyzing crystals were PET (P, Nb, U, Th, Ti, Y, Ca, K, and Cl), LIF (Ta, La, Ce, Pr, Nd, Sm, Gd, Dy, Er, Yb, Fe, and Mn), LDE1 (F), and TAP (Si, Al, Mg, and Na). The Kα line was chosen for the analyses of P, Si, Ti, Al, Fe, Mn, Mg, Ca, Na, K, F, and Cl. The Lα line was chosen for Nb, Ta, La, Ce, Y, and Yb. The Lβ line was chosen for Pr, Nd, Sm, Gd, Dy, and Er. The Mα line was chosen for Th and U. The counting times of peaks are 10 s for F, Cl, Na, and K, 20 to 60 s for other elements. Background intensities were measured on both sides of the peak for half of the peak time. The standards are apatite for P, Nb metal for Nb, Ta metal for Ta, uraninite for U, huttonite for Th, hornblende for Si, Fe, Mg, and Ca, $MnTiO_3$ for Ti and Mn, monazite for La, Ce, Pr, Nd, and Sm, synthesized REE-phosphates for Gd, Dy, Er, Yb, and Y, garnet for Al, K-feldspar for K, albite for Na, topaz for F, and $Ba_5(PO_4)_3(OH, Cl)$ for Cl. All data were corrected using standard ZAF correction procedures. A representative selection of the EMP analytical data are listed in Table 2, and the whole dataset can be found in the Supplemental Material.

The mineral trace element analyses were performed using a RESOlution M-50 laser ablation (LA) system coupled to an Agilent 7500a type inductively coupled plasma-mass spectrometer (ICP-MS) at the Guangzhou Institute of Geochemistry, Chinese Academy of Sciences. Detailed analytical protocols were given by Tu et al. (2011). Analyses were performed on thin sections, with a beam diameter of 32 um and a repetition rate of 4 Hz. The counting times were ~20 s for the background analysis, and ~45 s for the sample analysis. The glass standard NIST 610 was used as an external calibration standard, and was analyzed twice after 8 sample analyses (2 NIST610 + 8 samples + 2 NIST610). Calcium was used as the internal standard for fluorapatite and allanite-(Ce), Ce was used for monazite-(Ce), and Si was used for chevkinite-(Ce). The absolute contents of CaO, Ce_2O_3, and SiO_2 were determined by EMP analyses. Precision based on repeated analysis of standards is better than 10 %.

Data reduction was performed by the software ICPMSDataCal (Liu et al., 2008). Representative LA-ICP-MS trace element data are listed in Table 3, and the whole dataset can be found in the Supplemental Material.

The *in-situ* Sm-Nd isotopic compositions of allanite-(Ce) were measured using a Neptune multi-collector (MC) ICP-MS, equipped with a Geolas 193 nm excimer laser ablation system at the Institute of Geology and Geophysics, Chinese Academy of Sciences. The analytical protocol follows that described by Yang et al. (2014). The analyses were conducted on thin sections, with a spot size of 32 um and a repetition rate of 6 Hz. Each spot analysis consists of ~20 s background acquisition and ~60 s sample data acquisition. Every ten sample analyses were followed by two Namaqua monazite reference material measurements for external calibration, utilizing the reference values: $^{147}Sm/^{144}Nd$: 0.0977 ± 0.0002; $^{143}Nd/^{144}Nd$: 0.511896 ± 0.000032 (Liu et al., 2012). The isobaric interference of ^{144}Sm on ^{144}Nd is significant. We used the measured $^{147}Sm/^{149}Sm$ ratio to calculate the Sm fractionation factor and the measured ^{147}Sm intensity using the natural $^{147}Sm/^{144}Sm$ ratio to estimate the Sm interference on mass 144. The interference-corrected $^{146}Nd/^{144}Nd$ ratio can then be used to calculate the Nd fractionation factor. Finally, the $^{147}Sm/^{144}Nd$, $^{143}Nd/^{144}Nd$ and $^{145}Nd/^{144}Nd$ ratios were normalized using the exponential law. The raw data were exported offline and the whole data-reduction procedure was performed using an in-house Excel VBA (Visual Basic for Applications) macro program. The apatite standard AP2 was measured as an external standard to monitor the accuracy of the analytical procedure, yielding weighted mean $^{147}Sm/^{144}Nd$ and $^{143}Nd/^{144}Nd$ ratios of 0.0764 ± 0.0004 of 0.51101 ± 0.00002, respectively. These values are consistent, within uncertainties, with the reported values of 0.0764 ± 0.0002 and 0.511007 ± 0.000030, respectively (Yang et al., 2014). The *in-situ* Sm-Nd isotopic data are listed in Supplemental Material.

ALTERATION TEXTURE OF MONAZITE-(CE) AND CHEVKINITE-(CE)

Monazite-(Ce)

Pristine, unaltered monazite-(Ce) is very rare in the Sin Quyen deposit. Most

241 crystals have undergone hydrothermal alteration, resulting in a distinct concentric
242 three-layered corona texture. The center of the corona is comprised of one or more
243 relict monazite-(Ce) crystals (Figs. 4a and b), which appear fairly homogeneous in
244 back scattered electron (BSE) images (Fig. 4c). The proportional volume of
245 monazite-(Ce) to the rest of the coronas varies from ~5 to ~70%. The monazite-(Ce)
246 crystals are euhedral to anhedral, and have variable sizes (10 to 200 μm in length).
247 They may contain some euhedral to subhedral albite, magnetite, and quartz inclusions
248 (Fig. 4d). The monazite-(Ce) is surrounded by a continuous or discontinuous
249 fluorapatite [$Ca_5(PO_4)_3F$] mantle of variable thicknesses (Figs. 4a, b and d). The
250 boundary between the monazite-(Ce) and fluorapatite is embayed and corroded, and
251 the shape of the fluorapatite mantle is typically irregular. Magnetite, allanite-(Ce), and
252 U-bearing phases may occur in the fluorapatite zone. The fluorapatite mantle is
253 further surrounded by a rim of allanite-(Ce). The allanite-(Ce) rim contains either a
254 single crystal (e.g., Figs. 4a and b), or multiple crystals (e.g., Figs. 4d and e). Small
255 islands of fluorapatite are usually identified in the allanite-(Ce) zone (Fig. 4e).
256 Allanite-(Ce) rims are typically irregular in shape, with variable thicknesses. The
257 margins and, in a few cases, the interiors of the allanite-(Ce) commonly show low and
258 patchy levels of brightness under BSE imaging (Fig. 4). The BSE-dark regions have
259 sharp boundaries with the BSE-bright regions. It is notable that the fluorapatite and
260 allanite-(Ce) may occur together in the interior of monazite-(Ce), generally with
261 fluorapatite adjacent to monazite-(Ce) (Figs. 4d and e). Thus, it appears that the
262 interior of some monazite-(Ce) crystals have also been partially replaced. It is also
263 notable that some corona textures do not have monazite-(Ce) cores. Instead, they have
264 cores of fluorapatite crystals surrounded by allanite-(Ce) crystals, indicating that the
265 original monazite-(Ce) was completely consumed (Fig. 4f). The
266 monazite-(Ce)-fluorapatite-allanite-(Ce) corona textures mainly occur in the
267 albite-rich ore samples (Fig. 3c), but they can also be observed in albitite close to the
268 ore bodies. When identified, the outermost allanite-(Ce) rims are in planar contact
269 with, or occur as spiky or lobate protrusions into, the surrounding minerals, such as
270 albite, magnetite, and biotite (Fig. 4).

Alteration of monazite that involved the formation of similar corona textures has been previously documented in metapelitic to granitic rocks (e.g., Finger et al., 1998; Broska et al., 2005; Ondrejka et al., 2012; Upadhyay and Pruseth, 2012; Lo Pò et al., 2016). In those corona textures, the apatite zone adjacent to relict monazite commonly has a euhedral to subhedral shape, testifying that the apatite directly replaced primary monazite (Finger et al., 1998; Upadhyay and Pruseth, 2012). In contrast, fluorapatite zones in this study are commonly irregular in shape with variable thicknesses, which may be due to the higher mobility of P in the alteration process. The other corona textures are also different from our samples in that they have many small Th-rich phases in the apatite zone. Thorium was released from primary Th-rich monazite. The monazite-(Ce) in this study is poor in Th (see next section), so Th-rich phases are only rarely observed in the corona textures.

Chevkinite-(Ce)

In the Sin Quyen deposit, almost all chevkinite-(Ce) crystals have been subjected to hydrothermal alteration, and the altered chevkinite-(Ce) has been invariably mantled by allanite-(Ce) (Fig. 5a). In rare cases, the partially altered monazite-(Ce) and chevkinite-(Ce) crystals are mantled together by allanite-(Ce) (Fig. 5b). The allanite-(Ce) mantles have different thicknesses, and may contain some magnetite and uraninite crystals. The outermost part of the allanite-(Ce) mantle usually appears darker with patchy levels of grey in BSE images (Fig. 5). The chevkinite-(Ce)-allanite-(Ce) assemblages are mostly present in the albite-rich ore samples, but they may also occur as disseminations in a biotite-rich matrix or in albitite (Fig. 3d).

The extent of chevkinite-(Ce) alteration differs from grain to grain. The least altered crystals are fairly homogeneous in the BSE images, and they may show a spatial association with sparse secondary allanite-(Ce) and aeschynite-(Ce) crystals (Fig. 5c). The slightly altered chevkinite-(Ce) crystals have rims replaced by secondary allanite-(Ce) and aeschynite-(Ce) (Fig. 5d). The secondary allanite-(Ce) is crystalographically continuous with the allanite-(Ce) mantle, i.e., they belong to the

same crystal. The aeschynite-(Ce) forms small (mostly < 2 μm in length), anhedral crystals at the contacts between chevkinite-(Ce) and allanite-(Ce). Sometimes aeschynite-(Ce) grows as plate-like crystals at right angles to the contacts between the chevkinite-(Ce) and allanite-(Ce) mantle. Crystals with more extensive alteration have broader margin areas replaced by secondary allanite-(Ce) and aeschynite-(Ce) (Fig. 5e). In this case, aeschynite-(Ce) is present as small patches set in a matrix of secondary allanite-(Ce). The more severely altered crystals have interiors replaced by secondary allanite-(Ce) and aeschynite-(Ce) (Fig. 5f). Both secondary allanite-(Ce) and aeschynite-(Ce) occur as small (< 2 μm), anhedral crystals intergrown with each other. Pseudomorphic outlines are preserved for rare completely altered crystals (Fig. 5g). In addition to allanite-(Ce) and aeschynite-(Ce), bastnäsite-(Ce), columbite-(Fe), and ilmenite are also locally present as alteration products. The appearance of bastnäsite-(Ce) is similar to that of aeschynite-(Ce), forming small (mostly < 5 μm), anhedral crystals disseminated in the matrix of secondary allanite-(Ce). Columbite-(Fe) and ilmenite commonly form relatively large (5 to 15 μm), subhedral to anhedral crystals intergrown with allanite-(Ce) and aeschynite-(Ce). Although most altered chevkinite-(Ce) crystals have a similar alteration assemblages, i.e., allanite-(Ce) + aeschynite-(Ce) ± bastnäsite-(Ce) ± columbite-(Fe) ± ilmenite, there are also some exceptions. For example, in one sample, in addition to allanite-(Ce) and aeschynite-(Ce), ilmenite is also one of the major alteration products (Fig. 5g). In another sample, chevkinite-(Ce) is replaced dominantly by secondary allanite-(Ce), with rare aeschynite-(Ce) (Fig. 5h).

Several studies have addressed the alteration of chevkinite from syenitic to granitic intrusions. During alteration, the newly-formed chevkinite may be enriched in Ti, and depleted in Si, REE, and Fe compared to the primary phase (Baginski et al., 2015, and references therein). The alteration can also lead to the formation of new mineral assemblages, such as allanite + ilmenite + titanite + epidote (Jiang, 2006), allanite + rutile + titanite (Macdonald et al., 2015b), and bastnäsite-(Ce) + ilmenite + columbite-(Fe) (Macdonald et al., 2015a). To our knowledge, the transition from chevkinite-(Ce) to mainly allanite-(Ce) and aeschynite-(Ce) has not been documented

before.

MINERAL COMPOSITIONS

Common allanite-(Ce)

"Common allanite-(Ce)" denotes the allanite-(Ce) grains unrelated to the alteration of monazite-(Ce) or chevkinite-(Ce) (Figs. 3e and f). In general, these common allanite-(Ce) grains are homogeneous in composition (Fig. 6), and have an average composition of $(Ca_{1.07}Ce_{0.48}La_{0.30}Nd_{0.05}Pr_{0.03})_{\Sigma 1.93}(Al_{1.62}Fe^{3+}_{0.72}Fe^{2+}_{0.71}Mg^{2+}_{0.12})_{\Sigma 3.17}(Si_{0.97}O_4)_3(OH)$.

The LA-ICP-MS data are in good agreement with the EMP analytical data for the LREE (Tables 2 and 3). The concentrations of heavy REE (HREE: elements from Gd to Lu) and Y vary from 923 to 1432 ppm. In the chondrite-normalized REE plots, they show steeply right-inclined profiles ($(La/Yb)_N$ = 1155 to 2369), with negative Eu anomalies (Eu/Eu* = 0.44 to 0.70) (Fig. 7a). Besides (HREE+Y), common allanite-(Ce) also contains moderate amounts of Th (121 to 521 ppm), U (42.0 to 332 ppm), V (73.9 to 165 ppm), As (74.5 to 97.9 ppm), Ge (150 to 185 ppm), Ti (770 to 6523 ppm), and Sr (41.1 to 262 ppm). Germanium and As contents generally show positive correlations.

Common fluorapatite

"Common fluorapatite" denotes the fluorapatite grains unrelated to the alteration of monazite-(Ce) (Fig. 3f). In addition to CaO and P_2O_5, common fluorapatite also contains 1.7 to 3.5 wt.% F, minor SiO_2 (below detection limit to 0.69 wt.%), and FeO (0.03 to 0.47 wt.%). The average composition is $Ca_{5.04}P_{2.96}O_{12}(F_{0.66}OH_{0.34})$.

Common fluorapatite has variable (REE + Y) (3792 to 20171 ppm), which generally show positive correlation with the concentration of Si. Thus, REE^{3+} and Y^{3+} are principally charge-balanced through the coupled substitution: $Si^{4+} + (REE+ Y)^{3+} = P^{5+} + Ca^{2+}$ (Roeder et al., 1987; Pan and Fleet, 2002). Although the common fluorapatite grains have variable REE concentrations, their chondrite-normalized REE patterns are similar, with a nearly flat profile from La to Pr, a slightly right-inclined

361 profile from Nd to Dy, and a slightly left-inclined to nearly flat profile from Ho to Lu
362 (Fig. 7b). Besides (REE+Y), common fluorapatite also contains moderate Sr (493 to
363 1111 ppm), U (20.4 to 246 ppm), As (40.4 to 316 ppm), and Ge (6.33 to 36.4 ppm),
364 and minor amounts of Th (0.58 to 16.9 ppm).
365
366 **Monazite-(Ce) and minerals associated with its alteration**
367 *Monazite-(Ce)*
368 Different monazite-(Ce) grains have almost indistinguishable major element
369 contents. Apart from $LREE_2O_3$ and P_2O_5, they also contain minor amounts of ThO_2 (<
370 0.66 wt. %), CaO (< 0.52 wt. %), and SiO_2 (0.04 to 0.47 wt. %), indicative of very
371 minor huttonite ($ThSiO_4$) and brabantite [$CaTh(PO_4)_2$] substitutions (Fig. 8a). Their
372 average composition is $(Ce_{0.53}La_{0.35}Nd_{0.07}Pr_{0.04}))_{\Sigma 0.99}P_{1.00}O_4$.
373 Monazite-(Ce) grains have (HREE+Y) ranging from 2644 to 4422 ppm. They
374 have steeply right-inclined chondrite-normalized REE profiles ($(La/Yb)_N$ = 6150 to
375 17974), with moderately negative Eu anomalies (Eu/Eu* = 0.52 to 0.63) (Fig. 7c).
376 Besides (HREE+Y), they are also rich in U (340 to 1536 ppm), Th (337 to 2420 ppm),
377 Ge (488 to 581 ppm), and As (308 to 760 ppm).
378 *Fluorapatite*
379 Fluorapatite crystals from corona textures have similar major element contents as
380 common fluorapatite, but their contents of F are slightly higher (2.6 to 3.6 wt.%).
381 Their average composition is $Ca_{5.07}P_{2.95}O_{12}(F_{0.82}OH_{0.18})$.
382 They contain 5733 to 18794 ppm (REE + Y), 492 to 906 ppm Sr, 10.4 to 208 ppm
383 U, 0.44 to 53.8 ppm Th, 13.2 to 154 ppm As, and 8.55 to 35.4 ppm Ge, similar to
384 those of common fluorapatite (Table 3). Their chondrite-normalized REE profiles also
385 resemble those of common fluorapatite (Fig. 7c).
386 *Allanite-(Ce)*
387 Allanite-(Ce) crystals from different corona textures display little spread in major
388 element contents (Fig. 6). Their average composition can be expressed as
389 $(Ca_{1.03}Ce_{0.48}La_{0.31}Nd_{0.06}Pr_{0.03})_{\Sigma 1.91}(Al_{1.63}Fe^{3+}_{0.64}Fe^{2+}_{0.78}Mg_{0.10})_{\Sigma 3.15}(Si_{0.97}O_4)_3(OH)$,
390 notably similar to that of common allanite-(Ce).

They have (HREE+Y) (964 to 2171 ppm), U (67.8 to 311 ppm), Th (180 to 917 ppm), As (75.8 to 104), V (44.5 to 148 ppm), Co (8.81 to 21.6 ppm), and Sr (33.4 to 263 ppm) similar to those of common allanite-(Ce), but their concentrations of Ge (156 to 210 ppm), Ti (3229 to 14470 ppm), and Nb (0.99 to 7.76) are generally higher than those of common allanite-(Ce) (Table 3). Their chondrite-normalized REE patterns are similar to those of common allanite-(Ce) (Fig. 7c).

Chevkinite-(Ce) and minerals associated with its alteration

Chevkinite-(Ce)

Chevkinite-group minerals have a general formula, $A_4BC_2D_2(Si_2O_7)_2O_8$, where the dominant cations in each site are: A = Ca and REE; B = Fe^{2+}; C = Fe^{3+}, Fe^{2+}, Ti, Nb, D = Ti (Macdonald and Belkin, 2002). Chevkinite-(Ce) crystals from the Sin Quyen deposit have an average composition of $(Ce_{1.93}La_{1.18}Ca_{0.45}Nd_{0.36}Pr_{0.15})_{\Sigma 4.07}$ $Fe(Fe_{1.26}Ti_{0.47}Nb_{0.25}Al_{0.07}Mg_{0.06})_{\Sigma 2.11}Ti_2(Si_{2.02}O_7)_2O_8$. There is a negative correlation between (Ca+Ti) and (REE + divalent and trivalent cations content in the C site), implying a substitution scheme of [$Ca_A^{2+} + Ti_C^{4+} \rightarrow REE_A^{3+} + M_C^{3+,2+}$] (Fig. 8b; Macdonald and Belkin, 2002).

They contain 2964 to 4567 ppm (HREE+Y), and have a chondrite-normalized REE diagram with steeply right-inclined LREE profile ($(La/Eu)_N$ = 41 to 71), slightly concave-up HREE profile, and slightly to moderately negative Eu anomalies (Eu/Eu* = 0.55 to 0.83) (Fig. 7d). They are also rich in a series of other trace elements, including U (577 to 2265), Th (562 to 1899 ppm), Zr (153 to 1290 ppm), Ge (317 to 430 ppm), Ta (89.2 to 357 ppm), Sc (61.6 to 267 ppm), V (91.2 to 273 ppm), Cr (56.6 to 625 ppm), As (154 to 238 ppm), Sn (122 to 768 ppm), W (193 to 358 ppm), and Sr (125 to 674 ppm).

Allanite-(Ce)

Both secondary allanite-(Ce) replacing chevkinite-(Ce), and allanite-(Ce), which forms a mantle around altered chevkinite-(Ce), have relatively constant major element contents (Fig. 6). Their average compositions are $(Ca_{1.02}Ce_{0.47}La_{0.29}Nd_{0.06}Pr_{0.04})_{\Sigma 1.88}(Al_{1.59}Fe^{3+}_{0.76}Fe^{2+}_{0.74}Mg_{0.10})_{\Sigma 3.19}(Si_{0.96}O_4)_3(OH)$, and

421 $(Ca_{0.10}Ce_{0.50}La_{0.30}Nd_{0.06}Pr_{0.03})_{\Sigma 1.89}(Al_{1.54}Fe^{3+}_{0.76}Fe^{2+}_{0.78}Mg_{0.10})_{\Sigma 3.18}(Si_{0.96}O_4)_3(OH)$,
422 respectively, which are almost indistinguishable from each other. It is notable that
423 these compositions are very similar to those of common allanite-(Ce) and allanite-(Ce)
424 in corona textures (Fig. 6).

425 Allanite-(Ce) mantles have trace element concentrations and
426 chondrite-normalized REE patterns similar to those of common allanite-(Ce) and
427 allanite-(Ce) in corona textures (Table 3; Fig. 7d). Notable exceptions are Ge (160 to
428 223 ppm), As (84.8 to 120 ppm), Ti (5160 to 13501 ppm), and Nb (3.31 to 43.9 ppm),
429 which are generally higher in the allanite-(Ce) mantles (Table 3).

430 *Aeschynite-(Ce)*

431 The aeschynite-group mineral has a general formula of AB_2O_6, where A = REE,
432 Ca, Th, U and Fe, and B = Nb, Ti and Ta (Ercit, 2005). Regarding aeschynite-(Ce) in
433 this study, the A site is occupied by variable LREE (0.47 to 0.93 a.p.f.u.), Ca (0.02 to
434 0.39 a.p.f.u.), and U (0.01 to 0.07 a.p.f.u.) (Fig. 8c). All the analyses have Ce as the
435 major cation except for one, in which Ca is the major cation. The B site contains
436 variable Nb (0.61 to 1.24 a.p.f.u.) and Ti (0.72 to 1.45 a.p.f.u.) (Fig. 8d). Overall,
437 aeschynite-(Ce) has highly variable compositions. However, we were unable to find
438 any relationship between composition and textural position.

439

440 **Altered domains in allanite-(Ce)**

441 The altered (BSE-dark) domains in allanite-(Ce) have obviously higher CaO and
442 Al_2O_3, and lower $LREE_2O_3$, FeO, and MgO than the unaltered domains. If the altered
443 and unaltered allanite-(Ce) domains are taken together, it can be observed that their
444 LREE is negatively correlated with Ca (Fig. 8e). Their [REE^{3+} + (Fe^{2+}, Mg^{2+})] and
445 [Ca^{2+} + (Al, Fe^{3+})] show a negative correlation as well (Fig. 8f). Such relationships
446 are indicative of the following coupled substitution [REE^{3+} + (Fe^{2+}, Mg^{2+}) → Ca^{2+} +
447 (Al, Fe^{3+})] in the various allanite-(Ce) domains.

448

449 ***In-situ* Sm-Nd isotope composition of allanite-(Ce)**

450 The different allanite-(Ce) domains, including common allanite-(Ce),

allanite-(Ce) in monazite-(Ce) alteration coronas, and allanite-(Ce) mantles around chevkinite, have similar Sm-Nd isotopic compositions (Fig. 9). Their $^{147}Sm/^{144}Nd$ and $^{143}Nd/^{144}Nd$ ratios vary from 0.0359 to 0.0508 and from 0.51147 to 0.51170, respectively. At an age of 840 Ma, their $\varepsilon_{Nd}(t)$ values vary from -5.8 to -1.4, mostly clustered between -4.0 and -2.0.

DISCUSSION

Paragenetic interpretations

Formation and alteration of monazite-(Ce)

The majority of altered monazite-(Ce) crystals occur in albite-rich ore samples or albitite (Fig. 3c). Also, some monazite-(Ce) crystals contain euhedral to subhedral inclusions of albite (Fig. 4d). These observations suggest that monazite-(Ce) was largely formed during stage I. The fluorapatite and allanite-(Ce) in the corona textures have compositions rather similar to the common fluorapatite and allanite-(Ce), respectively, which implies that they were formed in similar environments. The spatial association between the allanite-(Ce) rim and magnetite suggests that the two phases were formed at the same stage (stage II) (Figs. 4a and e). Thus, the alteration of monazite-(Ce) may have occurred during stage II.

The three-layered corona texture might have been produced in two ways: 1) the monazite-(Ce) was replaced/overgrown by a fluorapatite mantle, which was further replaced/overgrown by an allanite-(Ce) rim; or 2) dissolution of monazite-(Ce), accompanied by the simultaneous growth of fluorapatite mantle and allanite-(Ce) rim. A key difference between these two mechanisms is the relative sequence of fluorapatite and allanite-(Ce). In the ore samples, common fluorapatite and allanite-(Ce) usually form individual grains associated with the minerals of stage II (e.g., magnetite, amphibole and biotite), and they do not have any special textural relationships with each other (Figs. 3e and f). Thus, there is no evidence to show that fluorapatite was paragenetically earlier than allanite-(Ce) in this deposit. On this basis, we propose that the fluorapatite and allanite-(Ce) in the corona textures were produced at the same time. We speculate that when monazite-(Ce) reacted with fluids,

its major components, P and REE, were released into the fluid. Phosphorus was immediately combined with Ca in the fluids, forming fluorapatite close to the reaction front. The REE were then transported out for a short distance, and combined with Si, Fe, Al and other trace elements, forming allanite-(Ce). During the reaction process, the fluorapatite front generally advanced inward into the monazite, whereas allanite-(Ce) formed as a fringe outward from monazite-(Ce).

The allanite-(Ce) in corona textures commonly has margins and, less commonly, part of the interiors being altered, with the removal of REE and Fe, and the addition of Ca and Al. In fact, common allanite-(Ce) and the allanite-(Ce) mantled chevkinite-(Ce) underwent similar styles of alteration. The timing of this alteration is uncertain. It may have occurred either shortly or long after the formation of allanite-(Ce). We note that the crystal orientation of the altered region remains the same as the primary allanite-(Ce) crystal, and that there are sharp compositional interfaces between the altered and unaltered regions. Textures such as these are interpreted to result from compositional alteration driven by fluid-aided coupled dissolution-reprecipitation (cf. Putnis, 2002, 2009; Harlov et al., 2005, 2011; Harlov and Hetherington, 2010).

Formation and alteration of chevkinite-(Ce)

Textural observations show that chevkinite-(Ce) has been replaced by secondary allanite-(Ce) and aeschynite-(Ce), and that the altered chevkinite-(Ce) is further mantled by allanite-(Ce) (Fig. 5). There is no physical boundary or obvious compositional discrepancy between the secondary allanite-(Ce) and the allanite-(Ce) mantle, indicating that they were formed at the same time, i.e., the alteration of chevkinite-(Ce) was accompanied by the growth of the allanite-(Ce) mantle. It is notable that the secondary allanite-(Ce) and allanite-(Ce) mantle have chemical and Sm-Nd isotopic compositions similar to the common allanite-(Ce) (Figs. 6 and 9). Also, magnetite and uraninite may occur as inclusions in allanite-(Ce) mantles (Figs. 5c and e). Therefore, the alteration of chevkinite-(Ce), together with the formation of allanite-(Ce) mantle, may have occurred during the main Fe-LREE mineralization stage (stage II). It is obvious that the chevkinite-(Ce) should have crystallized earlier. The common occurrence of altered chevkinite-(Ce) in the albite-rich ore samples or

511 albitite suggests that chevkinite-(Ce) was, at least in part, precipitated during stage I
512 (Fig. 3d). Thus, as in the case with monazite-(Ce), chevkinite-(Ce) may have formed
513 mainly during stage I, and undergone hydrothermal alteration during stage II. This
514 sequence is consistent with the coexistence of partially altered monazite-(Ce) and
515 chevkinite-(Ce) in the allanite-(Ce) mantle (Fig. 5b).
516
517 **Nature of the metasomatic fluids**
518 Several studies have documented that monazite breakdown corresponds with the
519 formation of metamorphic allanite in rocks with a moderate to high Ca content
520 (Finger et al, 1998; Ferry, 2000; Wing et al., 2003; Rasmussen and Muhling, 2009).
521 Thermodynamic modeling shows that elevating the bulk-rock CaO content or Ca/Na
522 ratio will extend the stability field of allanite over monazite (Janots et al., 2007; Spear,
523 2010). In the case of granitic rocks, monazite generally occurs in peraluminous
524 granites with a relatively low Ca content; whereas allanite tends to occur in weakly
525 peraluminous to metaluminous granites with a relatively high Ca content (Montel,
526 1993; Broska et al., 2005; Catlos et al., 2008). In metasomatic experiments, the
527 conversion of monazite to allanite/epidote can occur only in the presence of Ca-rich
528 fluids with very high Ca/Na ratios (Budzyń et al., 2011). These phenomena
529 consistently indicate that a low-Ca environment favors monazite stability, whereas a
530 high-Ca environment favors allanite stability. In the Sin Quyen deposit, both sodic
531 and calcic alterations were well developed, indicating that the primary ore-forming
532 fluids had high activity of both Na and Ca. However, sodic alteration during
533 albitisation would consume large amounts of Na, and lead to a gradual increase in the
534 Ca/Na ratio of the fluid. It can be expected that at a certain point, monazite-(Ce)
535 formed in the early stage may not be in equilibrium with a later-stage Na-poor, but
536 Ca-rich fluid, such that it was partially altered to form allanite-(Ce) and fluorapatite.
537 Previous studies concerning the importance of temperature in monazite-allanite
538 relationships indicate a thermal window for allanite stability more or less between 250
539 and 550 ^{o}C, depending on the whole-rock composition (e.g., Gieré and Sorensen 2004;
540 Krenn and Finger, 2007; Janots et al., 2006, 2007). With increasing metamorphic

grade, allanite breaks down to monazite under lower amphibolite facies conditions (Janots et al., 2008). In the Sin Quyen deposit, the temperature of the ore-forming fluid decreased from the early Na alteration stage (579 to 588 °C), to the Fe-REE mineralization stage (466 to 559 °C), and further decreased during the latest Cu-Au mineralization stage (377 °C) (Li, 2016). This fluid cooling process possibly could further facilitate the transition from monazite-(Ce) to allanite-(Ce).

Chevkinite and allanite can occur together in calcalkaline to alkaline felsic intrusions. Chevkinite commonly crystallizes at higher temperatures than allanite-(Ce) (Robinson and Miller, 1999; Vlach and Gualda, 2007; Macdonald et al., 2013). In the Sin Quyen deposit, the formation of chevkinite at a relatively early stage indicates that in hydrothermal environments it may also favor high-temperature conditions. Cooling of fluids, together with increased Ca activity, may result in the replacement of chevkinite-(Ce) by allanite-(Ce). Information on the relationships between chevkinite and aeschynite is rather scarce, but the composition of the metasomatic fluids can be inferred from related precipitating minerals. We note that allanite, columbite, and pyrochlore were precipitated during stage II (Fig. 3h), indicating that the fluids in this stage had high LREE and Nb activities. The high activity of these elements would prompt their combination with Ti released from the breakdown of chevkinite-(Ce), producing aeschynite-(Ce) rather than other Ti-bearing phases (e.g., ilmenite, rutile, and titanite). In our study, the composition of aeschynite-(Ce) is highly heterogeneous, particularly regarding Nb and Ti (Fig. 8d). Niobium and Ti are generally considered to be immobile in hydrothermal fluids. However, their mobility can be largely increased if F is present in the fluid (Rapp et al., 2010; Timofeev et al., 2015; Tanis et al., 2016). It is also shown that they can be mobilized in Cl-bearing fluids, but the mobility is much lower than in F-bearing fluids (Rapp et al., 2010; Tanis et al., 2015). The gangue minerals in the Sin Quyen deposit are dominantly Cl-bearing silicates, amphibole, and biotite. Although some minerals may contain minor amounts of F, F-rich minerals, such as fluorite or bastnäsite, are rarely encountered. These observations are indicative of the Cl-rich, but F-poor nature of the ore-forming fluids. In such fluids, Nb and Ti may not be able to be homogenized efficiently, and thereby

their contents in aeschynite-(Ce) show large ranges. It can also explain why ilmenite may also become one of the major alteration products from chevkinite-(Ce), i.e., highly Ti-rich environment (Fig. 5g). Likewise, aeschynite-(Ce) may be nearly absent from the alteration products, i.e., extremely Nb-poor environment (Fig. 5h). Some information regarding the oxygen fugacity (f_{O2}) of the fluids can be deduced from the Fe-Ti-oxides. The local presence of rutile during stage I suggest that at that stage the f_{O2} was relatively high but did not exceed the magnetite-hematite buffer (Zhao et al., 1999). The local presence of ilmenite in the chevkinite-(Ce) alteration assemblage pointed to lower f_{O2} during stage II. Scaillet and Macdonald (2001) reported that the stability field of chevkinite in peralkaline felsic rocks expands as a function of an increasing oxidation state, implying that the formation of chevkinite may favor relatively oxidized environments. If so, a transition to lower f_{O2} may facilitate the breakdown of chevkinite-(Ce) during the later stages.

Mass balance calculation for element changes

Alteration of monazite-(Ce)

From the compositions of the monazite-(Ce), fluorapatite and allanite-(Ce), it is obvious that input of some elements, such as Si, Al, Ca and Fe, is necessary during the alteration of monazite-(Ce) to allanite-(Ce) and fluorapatite. Gain and loss of other elements might also have taken place. Mass balance calculations, on the basis of weight proportions and compositions of dissolved monazite-(Ce) and newly-formed fluorapatite and allanite-(Ce), are required to determine the element mobility. However, the fluorapatite and allanite-(Ce) in the corona textures have various shapes, and their distributions are different from case to case, making it difficult to determine the original shape and, thereby, the weight proportion of dissolved monazite-(Ce). In this case, the calculation was carried out in the following way. First, the relative area proportions of fluorapatite and allanite-(Ce) were measured by point counting. It is assumed that the area proportion can approximately represent the volume proportion. Using their respective densities (fluorapatite: 3.19 g/cm^3; allanite-(Ce): 3.75 g/cm^3), the weight proportions for the fluorapatite and allanite-(Ce) were estimated. Then,

601 using the weight proportions and compositions of fluorapatite and allanite-(Ce), the
602 average composition of the fluorapatite-allanite-(Ce) mixture zone was calculated.
603 Furthermore, it is assumed that Th was immobile during the alteration process, and on
604 this basis, the concentration of Th in the mixture zone was normalized to the same
605 value as that of monazite-(Ce). The remaining elements were accordingly normalized
606 as well. Finally, an enrichment factor for one certain element, defined as the ratio of
607 the normalized content of that element in the fluorapatite-allanite-(Ce) mixture zone
608 to that in monazite-(Ce), was calculated to determine the relative gain or loss of that
609 element.

610 The area measurements were conducted on fifteen corona textures. The resulting
611 area ratios of fluorapatite to allanite-(Ce) vary from 21:79 to 39:61, corresponding to
612 weight ratios of 18:82 to 35:65. The enrichment factors were calculated for three
613 coronas, one with the lowest fluorapatite/allanite-(Ce) area ratio, one with the highest
614 fluorapatite/allanite-(Ce) area ratio, and one with an intermediate ratio (Table 4; Fig.
615 10). For all the three coronas, the major elements in monazite-(Ce), La, Ce, Pr, and
616 Nd, were variably lost relative to Th. The trace elements, Sm, Eu, Gd, As, Ge, and U,
617 were also lost relative to Th. HREE (from Ho to Lu), HFSE (Nb, Ta, Ti, Zr and Hf),
618 and Sr were variably gained relative to Th. Phosphorus shows different mobilization
619 behaviors. It increased relative to Th in the highest fluorapatite/allanite-(Ce) ratio case,
620 whereas it was lost relative to Th in the other two cases.

621 *Alteration of chevkinite-(Ce)*

622 For the mass balance calculation, it is first assumed that only the secondary
623 allanite-(Ce) and aeschynite-(Ce) coexisting zone was originally occupied by
624 chevkinite-(Ce), i.e., the alteration is a volume-constant replacement reaction. Then,
625 the relative area proportions of secondary allanite-(Ce) and aeschynite-(Ce) were
626 measured, and it is assumed that the area proportion can represent the volume
627 proportion. Based on corresponding densities (chevkinite-(Ce): 4.61 g/cm^3;
628 aeschynite-(Ce): 4.52 g/cm^3; allanite-(Ce): 3.75 g/cm^3), the weight proportions for
629 dissolved chevkinite-(Ce), and newly-formed allanite-(Ce) and aeschynite-(Ce) were
630 estimated. Furthermore, the mass fractions of elements within the individual phases

631 were calculated by multiplying the weight proportion with the composition of each
632 phase. Finally, an enrichment factor for one certain element, defined as the ratio of the
633 mass fractions of that element in (allanite-(Ce) + aeschynite-(Ce)) to that in
634 chevkinite-(Ce), was calculated to determine the gain or loss of that element.

635 The calculations were made for two alteration systems (Table 5; Fig. 11), in
636 which aeschynite-(Ce) crystals are relatively homogeneous in composition. In the two
637 cases, some major elements in chevkinite-(Ce), including Ti, La, and Ce, were
638 obviously removed from the alteration system, and Si, Fe, and Pr were moderately to
639 slightly removed from the alteration system. However, some elements, such as Al, Ca,
640 Mg, Nb, U, Y, and Yb, needed to be externally supplied by the metasomatic fluids.

641 *Spatial scale of elemental mobility*

642 The above mass balance calculations show that LREE from La to Nd could be
643 partially removed from the monazite-(Ce) alteration system, and LREE from La to Pr
644 and Ti could be variably removed from the chevkinite-(Ce) alteration system, i.e.,
645 these elements show hydrothermal mobility, at least, on the hundreds of micrometers
646 scale. We note that abundant allanite and minor Ti-bearing phases (e.g., ilmenite and
647 aeschynite) occur in the ore samples, but LREE- and Ti-rich phases are rarely
648 observed in the rocks several meters away from the ore bodies. Thus, the LREE and
649 Ti released from the alteration systems were transported for less than a few meters,
650 before they were incorporated into new phases.

651

652 **A linkage between ore-fluid evolution, REE-mineral alteration and element**
653 **mobilization**

654 In the Sin Quyen deposit, monazite-(Ce) and chevkinite-(Ce) were mainly
655 deposited from a high-temperature, Na-rich fluid in the early Na-(Fe) alteration stage
656 (Fig. 12a). During later hydrothermal evolution, the Na activity of the fluids was
657 decreased, but the Ca activity generally kept constant. Consequently, the Ca/Na ratio
658 of the fluid was gradually increased. In addition, the fluid temperature gradually
659 decreased. Monazite-(Ce) and chevkinite-(Ce) were not stable in the presence of
660 cooler, Ca-rich fluids, and underwent partial to complete dissolution (Fig. 12b).

661 Phosphorus released during the breakdown of monazite-(Ce) was combined with Ca
662 from the fluids to form fluorapatite adjacent to the alteration front. A portion of the
663 released REE were transported out for a short distance, and re-incorporated into
664 allanite-(Ce) around fluorapatite. Titanium, released during the breakdown of
665 chevkinite-(Ce), was combined with Nb and REE to form aeschynite-(Ce) in, or very
666 close to, the previous zone of dissolved chevkinite-(Ce). The remaining elements
667 were incorporated into the newly-formed allanite-(Ce) close to the alteration system.
668 During the alteration processes of monazite-(Ce) and chevkinite-(Ce), some elements
669 were removed from the systems. However, they were not transported for long
670 distances, but were reincorporated into new phases in the mineralization zones. In the
671 further later ore-forming stage or long after the ore-forming event, different
672 allanite-(Ce) domains underwent further alteration, resulting in a decrease in REE and
673 Fe, and an increase in Ca and Al (Fig. 12c).
674

675 **IMPLICATION**

676 Previous studies concerning element mobility show that the traditionally
677 assumed hydrothermally immobile elements, such as REE and HFSE, can be largely
678 reserved in the alteration systems (e.g., Finger et al., 1998; Jiang, 2006; Upadhyay
679 and Pruseth, 2012; Macdonald et al., 2015a). In contrast, here these elements show
680 hydrothermal mobility on a scale of at least hundreds of micrometers, although the
681 mass balance calculations may have some uncertainties. For example, the area
682 percentage made by point counting may not represent the real volume percentage; the
683 Th may not be absolutely immobile during the alteration of monazite-(Ce); the
684 volume may not remain unchanged during the breakdown of chevkinite-(Ce); and the
685 average composition of only a few aeschynite-(Ce) grains may not be totally
686 representative of all the crystals.

687 In the Sin Quyen deposit, the metasomatic fluids had high contents of Cl^- and
688 HS^-, as evidenced by the occurrence of abundant Cl-bearing silicates and sulfides in
689 the ores. These ligands are recognized as effective mediums in aiding the transport
690 and mobility of a series of elements, even if these elements are traditionally assumed

691 to be hydrothermally inert (Williams-Jones and Migdisov, 2014 and references
692 therein). Thus, the metasomatic fluids had the potential to ensure the effective
693 dissolution of accessory minerals. In addition, many other elements in the ore-forming
694 fluids at Sin Quyen had high activities. Such fluids can pervasively flush the rocks
695 allowing for a high fluid/rock ratio. In this case, the local chemical environment for
696 the growth of newly formed minerals will be little influenced by the dissolution of
697 primary minerals, but is largely controlled by the composition of the metasomatic
698 fluids. In our samples, the fluorapatite and allanite-(Ce) in the monazite-(Ce)
699 alteration coronas have compositions very similar to the common fluorapatite and
700 allanite-(Ce), respectively. Even if As, Ge, Th, and U are enriched in monazite-(Ce),
701 these elements are not particularly enriched in fluorapatite and allanite-(Ce) in the
702 coronas. Also, the REE patterns of fluorapatite and allanite-(Ce) in the corona textures
703 resemble those of common fluorapatite and allanite-(Ce), respectively, but are
704 different from that of monazite-(Ce). Moreover, the secondary allanite-(Ce), after
705 chevkinite-(Ce), has compositions similar to that of common allanite-(Ce). These
706 facts indicate that the chemistry of metasomatic fluids is a main factor controlling the
707 composition of the alteration products, which in turn determines the gain and loss of
708 elements during alteration.

709 In order to investigate element mobility during fluid/rock interaction, it is
710 necessary to take into account the equilibrium between minerals and metasomatic
711 fluids, which is determined by the alteration temperature, pressure, redox conditions
712 and potential ligands present in the fluid. It follows that the commonly assumed inert
713 elements, such as HREE and HFSE, are potentially mobile during metasomatic
714 processes, which must be taken into account when interpreting the geochemistry of
715 the rocks that have undergone metasomatic alteration.

716

717 **ACKNOWLEDGEMENTS**

718 We would like to express our thanks to Prof. Wenlan Zhang from Nanjing University,
719 Dr. Congying Li from Guangzhou Institute of Geochemistry, Chinese Academy of
720 Sciences, and Prof. Yueheng Yang from Institute of Geology and Geochemistry,

Chinese Academy of Sciences for their help with data collection. Prof. Raymond MacDonald and Dr. Emilie Janots are greatly appreciated for their constructive reviews. Dr. Daniel E. Harlov is gratefully acknowledged for his editorial handling. This study was supported by a grant from State Key Laboratory for Mineral Deposits Research, Nanjing University (21-16-01), and a grant from Key Laboratory of Mineralogy and Metallogeny, Guangzhou Institute of Geochemistry (KLMM20150205).

REFERENCES

Bagiński, B., Macdonald, R., Dzierżanowski, P., Zozulya, D., and Kartashov, P.M. (2015) Hydrothermal alteration of chevkinite-group minerals: products and mechanisms. Part 1. Hydration of chevkinite-(Ce). Mineralogical Magazine, 79, 1019-1037.

Bea, F. (1996) Residence of REE, Y, Th and U in granites and crustal protoliths: implications for the chemistry of crustal melts. Journal of Petrology, 37, 521-551.

Broska, I., Williams, C.T., Janák, M., and Nagy, G. (2005) Alteration and breakdown of xenotime-(Y) and monazite-(Ce) in granitic rocks of the Western Carpathians, Slovakia. Lithos, 82, 71-83.

Budzyń, B., Harlov, D.E., Williams, M.L., and Jercinovic, M.J. (2011) Experimental determination of stability relations between monazite, fluorapatite, allanite, and REE-epidote as a function of pressure, temperature, and fluid composition. American Mineralogist, 96, 1547-1567.

Catlos, E.J., Baker, C.B., Cemen, I., and Ozerdem, C. (2008) Whole rock major element influences on monazite growth: examples from igneous and metamorphic rocks in the Menderes Massif, western Turkey. Mineralogia, 39, 7-30.

Ercit, T.S. (2005) Identification and alteration trends of granitic-pegmatite-hosted (Y,REE,U,Th)-(Nb,Ta,Ti) oxide minerals: a statistical approach. The Canadian Mineralogist, 43, 1291-1303.

Ferry, J.M. (2000) Patterns of mineral occurrence in metamorphic rocks. American Mineralogist, 85, 1573-1588.

Finger, F., Broska, I., Roberts, M.P., and Schermaier, A. (1998) Replacement of primary monazite

751 by apatite-allanite-epidote coronas in an amphibolite facies granite gneiss from the eastern Alps.
752 American Mineralogist, 83, 248-258.
753 Forster, H.J. (1998) The chemical composition of REE–Y–Th–U rich accessory minerals in
754 peraluminous granites of the Erzgebirge–Fichtelgebirge region, Germany: part I. The
755 monazite-(Ce)-brabantite solid solution series. American Mineralogist, 83, 259-272.
756 Geisler, T., Ulonska, M., Schleicher, H., Pidgeon, R.T., and van Bronswijk, W. (2001) Leaching
757 and differential recrystallization of metamict zircon under experimental hydrothermal
758 conditions. Contributions to Mineralogy and Petrology, 141, 53-65.
759 Geisler, T., Schaltegger, U., and Tomaschek, F. (2007) Re-equilibration of zircon in aqueous fluids
760 and melts. Elements, 3, 43-50.
761 Gieré, R. and Sorensen, S.S. (2004) Allanite and other REE-rich epidote group minerals. Review
762 in Mineralogy and geochemistry, 56, 431-493.
763 Harlov, D.E., Wirth, R., and Forster, H.J. (2005) An experimental study of
764 dissolution–reprecipitation in fluorapatite: fluid infiltration and the formation of monazite.
765 Contribution to Mineralogy and Petrology, 150, 268-286.
766 Harlov, D.E. and Hetherington, C.J. (2010) Partial high-grade alteration of monazite using
767 alkali-bearing fluids: experiment and nature. American Mineralogist, 95, 1105-1108.
768 Harlov, D.E., Wirth, R., and Hetherington, C.J. (2011) Fluid-mediated partial alteration in
769 monazite: the role of coupled dissolution–reprecipitation in element redistribution and mass
770 transfer. Contribution to Mineralogy and Petrology, 162, 329-348.
771 Krenn, E. and Finger, F., (2007) Formation of monazite and rhabdophane at the expense of allanite
772 during Alpine low temperature retrogression of metapelitic basement rocks from Crete, Greece,
773 microprobe data and geochronological implications. Lithos, 95 (1-2), 130-147.
774 Li, X.C. and Zhou, M.F. (2015) Multiple stages of hydrothermal REE remobilization recorded in
775 fluorapatite in the Paleoproterozoic Yinachang Fe-Cu-(REE) deposit, Southwest China.
776 Geochimica et Cosmochimica Acta, 166, 53-73.
777 Li, X.C. (2016) Neoproterozoic Fe-Cu-REE deposits in southwestern China and northwestern
778 Vietnam. Ph.D. Thesis, The University of Hong Kong.
779 Liu, Y.S., Hu, Z.C., Gao, S., Günther, D., Xu, J., Gao, C.G., and Chen, H.H. (2008) In situ analysis
780 of major and trace elements of anhydrous minerals by LA-ICP-MS without applying an internal

781 standard. Chemical Geology, 257, 34-43.

782 Liu, Z.C., Wu, F.Y., Yang, Y.H., Yang, J.H., and Wilde, S.A. (2012) Neodymium isotopic
783 compositions of the standard monazites used in U–Th–Pb geochronology. Chemical Geology,
784 334, 221-239.

785 Lo Pò, D., Braga, R., Massonne, H.J., Molli, G., Montanini, A., and Theye, T. (2016)
786 Fluid-induced breakdown of monazite in medium-grade metasedimentary rocks of the
787 Pontremoli basement (Northern Apennines, Italy). Journal of Metamorphic Geology, 34,
788 63-84.

789 Macdonald, R. and Belkin, H.E. (2002) Compositional variation in minerals of the chevkinite
790 group. Mineralogical Magazine, 66, 1075-1098.

791 Macdonald, R., Belkin, H.E., Wall, F., and Bagiński, B. (2009) Compositional variation in the
792 chevkinite group: new data from igneous and metamorphic rocks. Mineralogical Magazine, 73,
793 777-796.

794 Macdonald, R., Baginski, B., and Dzierzanowski P. (2013) Chevkinite-group minerals in UK
795 Palaeogene granites: Understanding REE-bearing accessory phases. The Canadian Mineralogist,
796 51, 333-347.

797 Macdonald, R., Bagiński, B., Kartashov, P.M., Zozulya, D., Dzierżanowski, P., and Jokubauskas,
798 P., (2015a) Hydrothermal alteration of a chevkinite-group mineral to a bastnäsite-(Ce)-ilmenite-
799 columbite-(Fe) assemblage:interaction with a F-, CO_2-rich fluid. Mineralogical Magazine, 109,
800 659-678.

801 Macdonald, R., Bagiński, B., Kartashov, P.M., Zozulya, D., and Dzierżanowski, P. (2015b)
802 Hydrothermal alteration of chevkinite-group minerals. Part 2. Metasomatite from the Keivy
803 massif, Kola Peninsula, Russia. Mineralogical Magazine, 79, 1039-1059.

804 McLean, R.N. (2001) The Sin Quyen iron oxide-copper-gold-rare earth oxide mineralization of
805 North Vietnam. In: Porter TM (ed) Hydrothermal iron oxide copper–gold & related deposits: a
806 global perspective. PGC, Adelaide, pp 293–301.

807 Montel, J.M. (1993) A model for monazite/melt equilibrium and application to the generation of
808 granitic magmas. Chemical Geology, 110, 127-146.

809 Janots, E., Negro, F., Brunet, F., Goffe, B., Engi, M., and Bouybaouene, M. L. (2006) Evolution of
810 the REE mineralogy in HP–LT metapelites of the Sebtide complex, Rif, Morocco: monazite

811 stability and geochronology. Lithos, 87, 214-234.

812 Janots, E., Brunet, F., Goffè, B., Poinssot, C., Burchard, M., and Cemiĉ, L. (2007)
813 Thermochemistry of monazite-(La) and dissakisite-(La): implications for monazite and allanite
814 stability in metapelites. Contributions to Mineralogy and Petrology, 154, 1-14.

815 Janots, E., Engi, M., Berger, J., Allaz, J., Schwarz, O., and Spandler, C. (2008) Prograde
816 metamorphic sequence of REE minerals in pelitic rocks of the Central Alps: implications for
817 allanite-monazite-xenotime phase relations from 250 to 610 °C. Journal of Metamorphic
818 Geology, 26, 509-526.

819 Jiang, N. (2006) Hydrothermal alteration of chevkinite-(Ce) in the Shuiquangou syenitic intrusion,
820 northern China. Chemical Geology, 227, 100-112.

821 Ondrejka, M., Uher, P., Putiš, M., Broska, I., Bačík, P., Konečný, P., and Schmiedt, I. (2012)
822 Two-stage breakdown of monazite by post-magmatic and metamorphic fluids: An example
823 from the Veporic orthogneiss, Western Carpathians, Slovakia. Lithos, 142-143, 245-255.

824 Pan, Y. and Fleet, M.E. (2002) Composition of the apatite-group minerals: substitution
825 mechanisms and controlling factors. In Phosphates: Geochemical, Geobiological, and Materials
826 Importance (eds. M. J. Kohn, J. Rakovan and J. M. Hughes), 48, 13-49.

827 Poitrasson, F., Chenery, S., and Bland, D.J. (1996) Contrasted monazite hydrothermal alteration
828 mechanisms and their geochemical implications. Earth and Planetary Science Letters, 145,
829 79-96.

830 Poitrasson, F. (2002) In-situ investigations of allanite hydrothermal alteration: examples from
831 calc-alkaline and anorogenic granites of Corsica (southeast France). Contribution to Mineralogy
832 and Petrology, 142, 485-500.

833 Putnis, A. (2002) Mineral replacement reactions: from macroscopic observations to microscopic
834 mechanisms. Mineralogical Magazine, 66, 689-708.

835 Putnis, A. (2009) Mineral replacement reactions. Reviews in Mineralogy and Geochemistry, 70,
836 87-124.

837 Rapp, J.F., Klemme, S., Butler, I.B., and Harley, S.L. (2010) Extremely high solubility of rutile in
838 chloride and fluoride-bearing metamorphic fluids: An experimental investigation. Geology, 38,
839 323-326.

840 Rasmussen, B. and Muhling, J.R. (2007) Monazite begets monazite: evidence for dissolution of

detrital monazite and reprecipitation of syntectonic monazite during low-grade regional metamorphism. Contribution to Mineralogy and Petrology, 154, 675-689.

Rasmussen, B. and Muhling, J.R. (2009) Reactions destroying detrital monazite in greenschist-facies sandstones from the Witwatersrand basin, South Africa. Chemical Geology, 264, 311-327.

Richard, A., Montel, J., Leborgne, R., Peiffert, C., Cuney, M., and Cathelineau, M. (2015) Monazite alteration in H_2O ± HCl ± NaCl ± $CaCl_2$ Fluids at 150 ^oC and p_{sat}: Implications for uranium deposits. Minerals, 5, 693-706.

Robinson, D.M. and Miller, C.F. (1999) Record of magma chamber processes preserved in accessory mineral assemblages, Aztec Wash pluton, Nevada. American Mineralogist, 84, 1346-1353.

Roeder, P.L., MacArthur, D., Ma, X.P., Palmer, G.R., and Mariano, A.N. (1987) Cathodoluminescence and microprobe study of rare-earth elements in apatite. American Mineralogist, 72, 801-811.

Scaillet, B. and Macdonald, R. (2001) Phase relations of peralkaline silicic magmas and petrogenetic implications. Journal of Petrology, 42, 825-845.

Seydoux-Guillaume, A.M., Montel, J.M., Bingen, B., Bosse, V., de Parseval, P., Paquette, J.L., Janots, E., and Wirth, R. (2012) Low-temperature alteration of monazite: Fluid mediated coupled dissolution-precipitation, irradiation damage, and disturbance of the U-Pb and Th-Pb chronometers. Chemical Geology, 330-331, 140-158.

Smith, M.P., Henderson, P., and Zhang P.S. (1999) Reaction relationships in the Bayan Obo Fe–REE–Nb deposit, Inner Mongolia, China: implications for the relative stability of rare earth element phosphates and fluorocarbonates. Contribution to Mineralogy and Petrology, 134, 294-310.

Škoda, R. and Novák, M. (2007) Y, REE, Nb, Ta, Ti-oxide (AB_2O_6) minerals from REL-REE euxenite-subtype pegmatites of the Trebič Pluton, Czech Republic; substitutions and fractionation trends. Lithos, 95, 43-57.

Tanis, E.A., Simon, A.C., Tschauner, O., Chow, P., Xiao, Y., Burnley, P., Cline, C.J., Hanchar, J.M., Pettke, T., Shen, G., and Zhao, Y. (2015) The mobility of Nb in rutile-saturated NaCl and NaF-bearing aqueous fluids from 1-6.5 GPa and 300-800 ^oC. American Mineralogist, 100,

1600-1609.

Tanis, E.A., Simon, A., Zhang, Y.X., Chow, P., Xiao, Y.M., Hanchar, J.M., Tschauner, O., and Shen, G.Y. (2016) Rutile solubility in NaF-NaCl-KCl-bearing aqueous fluids at 0.5-2.79 GPa and 250-650 ^{o}C. Geochimica et Cosmochimica Acta, 177, 170-181.

Timofeev, A., Migdisov, A.A., and Williams-Jones, A.E. (2015) An experimental study of the solubility and speciation of niobium in fluoride-bearing aqueous solutions at elevated temperature. Geochimica et Cosmochimica Acta, 158, 103-111.

Tu, X.L., Zhang, H., Deng, W.F., Ling, M.X., Liang, H.Y., Liu, Y., and Sun W.D. (2011) Application of RESOlution in-situ laser ablation ICP-MS in trace element analyses. Geochimica 10, 83-98 (in Chinese with English Abstract).

Upadhyay, D. and Pruseth, K.L. (2012) Fluid-induced dissolution breakdown of monazite from Tso Morari complex, NW Himalayas: evidence for immobility of trace elements. Contribution to Mineralogy and Petrology, 164, 303-316.

Vlach, S.R.F. and Gualda, G.A.R. (2007) Allanite and chevkinite in A-type granites and syenites of the Graciosa Province, southern Brazil. Lithos, 97, 98-121.

Williams-Jones, A.E. and Migdisov, A.A. (2014) Experimental Constraints on the Transport and Deposition of Metals in Ore-Forming Hydrothermal Systems. Society of Economic Geologists, Inc. Special Publication, 18, 77-95.

Wing, B., Ferry, J.M., and Harrison, T.M. (2003) Prograde destruction and formation of monazite and allanite during contact and regional metamorphism of pelites: petrology and geochronology. Contributions to Mineralogy and Petrology, 145, 228-250.

Yang, Y.H., Wu, F.Y., Yang, J.H., Chew, D.M., Xie, L.W., Chu, Z.Y., Zhang, Y.B., and Huang, C. (2014) Sr and Nd isotopic compositions of apatite reference materials used in U-Th-Pb geochronology. Chemical Geology, 385, 35-55.

Zhao, D., Essene, E.J., and Zhang, Y. (1999) An oxygen barometer for rutile-ilmenite assemblages: oxidation state of metasomatic agents in the mantle. Earth and Planetary Science Letters, 166, 127-137.

Zhou, M.F., Zhao, X.F., Chen, W.T., Li, X.C., Wang, W., Yan, D.P., and Qiu H.N. (2014) Proterozoic Fe–Cu metallogeny and supercontinental cycles of the southwestern Yangtze Block, southern China and northern Vietnam. Earth-Science Reviews, 139, 59-82.

901

902 **Figure captions**

903

904 Fig. 1 Geological map of the northwestern Vietnam region, showing the location of
905 the Sin Quyen deposit.

906

907 Fig. 2 (a) Simplified geological map of the Sin Quyen deposit. (b) Cross section A-B
908 located in (a). Note that the stars represent the approximate locations of the ore and
909 albitite samples.

910

911 Fig. 3 (a) A lenticular replacement orebody hosted in mica-schist. (b) A sample
912 containing both albitite (white domain) and Fe-Cu-LREE ore (black domain). Note
913 that the albitite is superimposed by later stage ore and gangue minerals. (c)
914 Monazite-(Ce) alteration corona textures in albitite. (d) Chevkinite-(Ce)-allanite-(Ce)
915 assemblages in albite-rich sample. (e) The main minerals include amphibole,
916 magnetite, and allanite-(Ce) in stage II. (f) Common fluorapatite grains in the ore
917 sample. Because fluorapatite and biotite have nearly indistinguishable levels of
918 brightness under BSE imaging, the outlines of the fluorapatite crystals are marked by
919 dotted yellow lines. (g) Magnification of the box area in Fig. 3e, showing that the
920 margins and part of the interior of the allanite-(Ce) grains are altered, forming
921 variably darker domains. (h) Uraninite, columbite-(Fe), and pyrochlore were
922 deposited together with allanite-(Ce) during stage II.
923 Abbreviations: Ab-albite, Aln-allanite-(Ce), Amp-amphibole, Ap-fluorapatite,
924 Bt-biotite, Ccp-chalcopyrite, Chev-chevkinite-(Ce), Col-columbite-(Fe),
925 Mgt-magnetite, Pcl-pyrochlore, Urn-uraninite.

926

927 Fig. 4 (a) A typical corona texture, with one monazite-(Ce) crystal in the core,
928 continuous fluorapatite in the mantle, and allanite-(Ce) in the rim. The allanite-(Ce)
929 rim occurs as lobate protrusions into the surrounding magnetite. (b) A typical corona
930 texture, with several monazite-(Ce) crystals in the core, discontinuous fluorapatite in

931 the mantle, and allanite-(Ce) in the rim. Note that the shapes of the fluorapatite mantle
932 and allanite-(Ce) rim are very irregular. (c) The same zone as Fig. 5b, but with low
933 brightness. Note that monazite-(Ce) is homogeneous in brightness. A U-rich mineral
934 is present in the fluorapatite mantle. (d) Monazite-(Ce) contains euhedral to subhedral
935 albite and magnetite inclusions. Part of the monazite-(Ce) interior was replaced by
936 fluorapatite and allanite-(Ce). (e) The three corona systems show very close spatial
937 relationships. In one of them, the monazite-(Ce) has interiors being replaced by
938 fluorapatite and allanite-(Ce). The newly-formed fluorapatite tend to occur adjacent to
939 the monazite-(Ce). (f) A corona texture lacking a core of monazite-(Ce), but with a
940 core of polygonal fluorapatite crystals surrounded by an allanite-(Ce) rim.
941 Abbreviations: Mnz-monazite-(Ce), Qz-quartz. Other abbreviations are the same as
942 those in Fig. 3.
943
944 Fig. 5 (a) Several variably altered chevkinite-(Ce) crystals are mantled by
945 allanite-(Ce). (b) Altered monazite-(Ce) and chevkinite-(Ce) crystals are mantled
946 together by allanite-(Ce). (c) A slightly altered chevkinite-(Ce) crystal, mantled by
947 allanite-(Ce). Sparse secondary allanite-(Ce) and aeschynite-(Ce) crystals can be
948 observed in or adjacent to the chevkinite-(Ce) (marked by red arrows). The
949 allanite-(Ce) mantle contains some magnetite inclusions. (d) The rim of
950 chevkinite-(Ce) is replaced by secondary allanite-(Ce) and aeschynite-(Ce), and the
951 altered chevkinite-(Ce) is mantled by allanite-(Ce). Note that there is no physical
952 boundary between secondary allanite-(Ce) and allanite-(Ce) mantle. (e) A
953 chevkinite-(Ce) has broader areas being replaced by secondary allanite-(Ce) and
954 aeschynite-(Ce) (marked by red arrow). The altered chevkinite-(Ce) is further mantled
955 by allanite-(Ce). Several uraninite crystals occur as inclusions in the allanite-(Ce)
956 mantle. (f) The interiors of chevkinite-(Ce) are partially replaced by secondary
957 allanite-(Ce) and aeschynite-(Ce). (g) A chevkinite-(Ce) crystal has been completely
958 replaced, and its pseudomorphic outline is preserved. The alteration products mainly
959 consist of allanite-(Ce), aeschynite-(Ce), and ilmenite, with sparse bastnäsite-(Ce). (h)
960 A chevkinite-(Ce) crystal is partially replaced by secondary allanite-(Ce), and the

961 altered chevkinite-(Ce) is further mantled by allanite-(Ce).

962 Abbreviations: Aes-aeschynite-(Ce), Aln(m)-allanite-(Ce) mantle around chevkinite,
963 Aln(s)-secondary allanite-(Ce) replacing chevkinite-(Ce), Bast-bastnäsite-(Ce),
964 Ilm-ilmenite. Other abbreviations are the same as those in Figs. 3 and 4.

965

966 Fig. 6 Plots of the dominant cations in the A (a) and the M (b) sites of allanite-(Ce).
967 Note that there are no obvious compositional discrepancies between different
968 allanite-(Ce) domains.

969

970 Fig. 7 (a) Chondrite-normalized REE profiles for common allanite-(Ce). (b)
971 Chondrite-normalized REE profiles for common fluorapatite. (c)
972 Chondrite-normalized REE profiles for the phases in monazite-(Ce) alteration coronas,
973 including monazite-(Ce), fluorapatite, and allanite-(Ce). The average composition of
974 common allanite-(Ce) (grey dashed line) and fluorapatite (black dashed line) are also
975 shown for comparison. (d) Chondrite-normalized REE profiles for chevkinite-(Ce),
976 aeschynite-(Ce), secondary allanite-(Ce), and allanite-(Ce) mantle. The average
977 composition of common allanite-(Ce) (grey dashed line) is also shown for comparison.
978 Note that the plotted data for secondary allanite-(Ce) and aeschynite-(Ce) were
979 obtained by EMP, whereas those for other phases were obtained by LA-ICP-MS.

980

981 Fig. 8 (a) Brabantite Ca(Th, U)REE_{-2} *vs*. huttonite (Th, U)Si$REE_{-1}P_{-1}$ exchange in
982 monazite shown in the plot 4*(Th + U + Si) *vs*. 4*(REE + Y + P). (b) The relationship
983 between (Ca+Ti) and (REE + divalent and trivalent cations in the C site) for
984 chevkinite-(Ce) indicates the coupled substitution scheme of [Ca_A^{2+} + Ti_C^{4+} →
985 REE_A^{3+} + $M_C^{3+,2+}$]. (c) Ternary diagram for cations in the A site for aeschynite-(Ce).
986 The arrow represents the coupled substitution vector: $^{A}Ca^{B}(Nb,Ta)$ $^{A}(Y,REE)_{-1}$ $^{B}Ti_{-1}$
987 (Škoda and Novák, 2007). (d) A cation plot of Nb *vs*. Ti for aeschynite-(Ce). (e) and (f)
988 Correlation plots for different cations in allanite-(Ce), showing the coupled
989 substitution scheme of [REE^{3+} + (Fe^{2+}, Mg^{2+}) → Ca^{2+} + (Al, Fe^{3+})].

990

Fig. 9 Histograms showing $\varepsilon_{Nd}(t)$ values for common allanite-(Ce) (a), for allanite-(Ce) in monazite alteration coronas (b), and for allanite-(Ce) mantles around chevkinite-(Ce) (c).

Fig. 10 Enrichment factors relative to P for selected major and trace elements during the alteration of monazite-(Ce). In (a), (b), and (c), the enrichment factors were calculated based on (fluorapatite/allanite-(Ce))$_{area}$ ratios of 21:79, 31:69, and 39:61, respectively. See text and Table 4 for more details.

Fig. 11 Enrichment factors for selected major and trace elements during the alteration of chevkinite-(Ce). In (a) and (b), the enrichment factors were calculated based on (aeschynite-(Ce)/allanite-(Ce))$_{area}$ ratios of 42:58 and 36:64, respectively. See text and Table 5 for more details.

Fig. 12 Cartoons illustrating the formation and alteration sequence of monazite-(Ce) and chevkinite-(Ce). (a) During the Na alteration stage (stage I), monazite-(Ce) and chevkinite-(Ce) were deposited from high-temperature, Na-rich fluids. (b) During the Fe-REE mineralization stage (stage II), the Ca/Na ratio of the fluid became higher, and the fluid temperature became lower. In the cooler, Ca-rich fluids, monazite-(Ce) was replaced by fluorapatite and allanite-(Ce). Chevkinite-(Ce) was replaced by aeschynite-(Ce) and allanite-(Ce), and at the same time the altered chevkinite was mantled by allanite-(Ce). (c) During the Cu-Au mineralization stage (stage III), different allanite-(Ce) domains underwent further alterations, resulting in decreases of REE and Fe, and increases of Ca and Al. Note that the alteration of allanite-(Ce) may also occur long after the ore-forming event. Mineral abbreviations are the same as those in Figs. 3, 4 and 5.

N

103° 40′

0 10km

22° 40′

22° 30′

Red River

100° E

103° E

106° E

25° N

23° N

21° N

Kunming

China

Vietnam

Hanoi

Laos

200km

Sin Quyen deposit

China

Vietnam

Lao Cai

Cenozoic strata

Mesozoic strata

Paleozoic strata

Proterozoic metamorphic complex

Cenozoic alkaline intrusion

Permian felsic intrusion

Neoproterozoic felsic intrusion

Permian basalt

Permian felsic volcanic rock

Fault

Fig. 1

(a)

Sin Quyen Reverse Fault

A

B

Western Mining District

Eastern Mining District

Ngoi Phat River

N

0 200 400m

(b)

B

A

250m

150m

50m

Ore sample

Albitite sample

Proterozoic Metapelite

Cambrian Strata

Granite

Orebody

Na-Ca-K alteration halo

Fig. 2

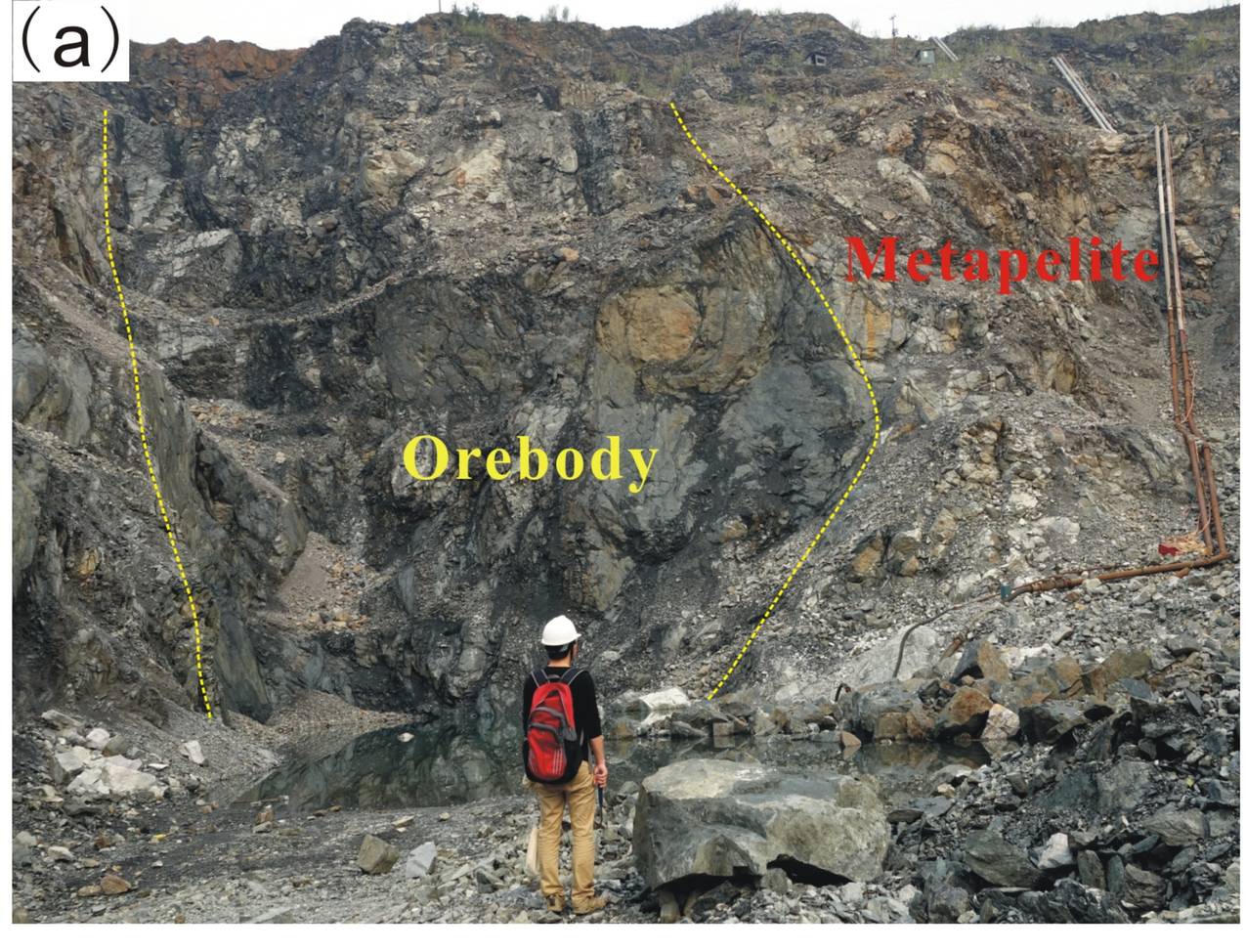
(a)
Metapelite
Orebody

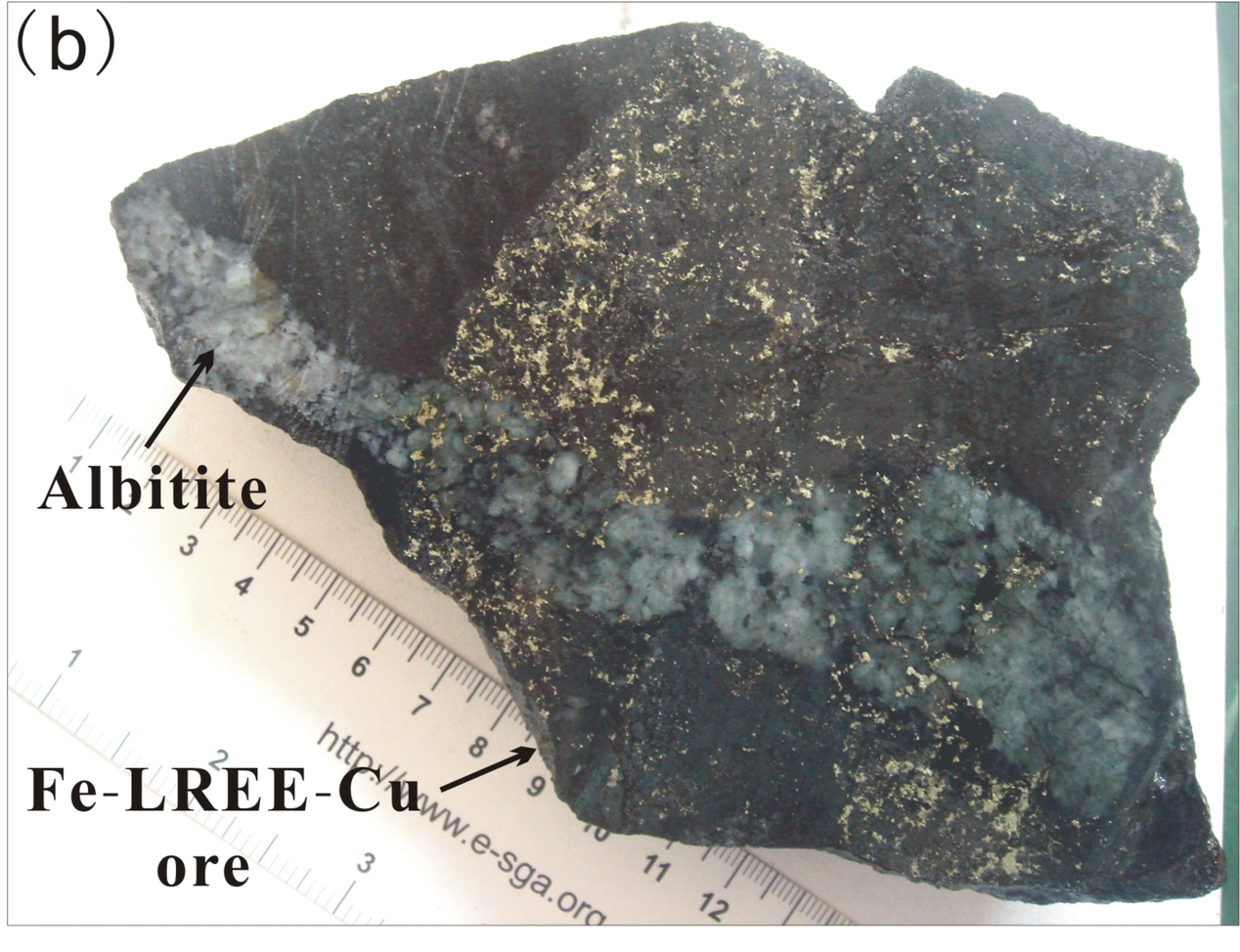
(b)
Albitite
Fe-LREE-Cu
ore

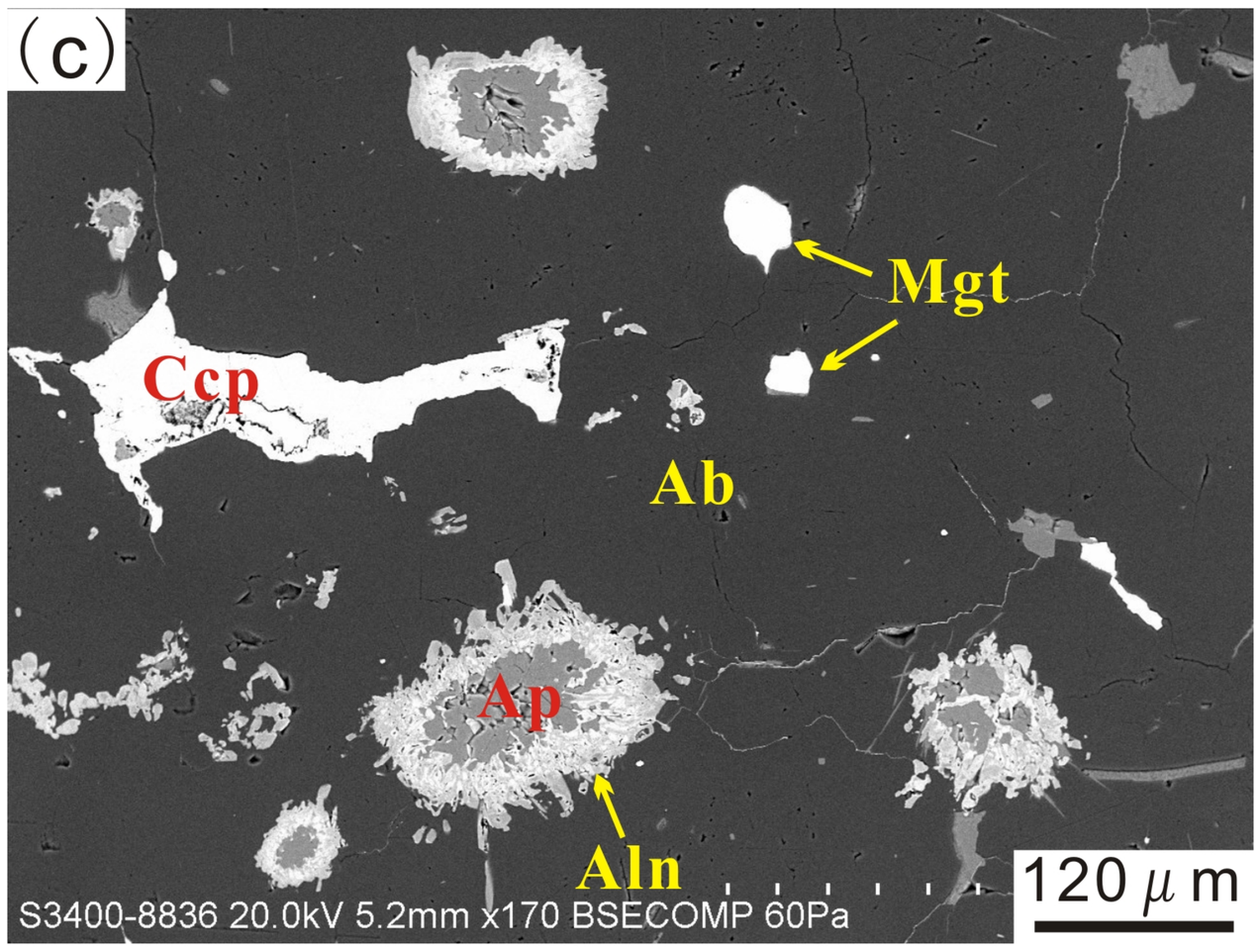
(c)
Mgt
Ccp
Ab
Ap
Aln
120 μm
S3400-8836 20.0kV 5.2mm x170 BSECOMP 60Pa

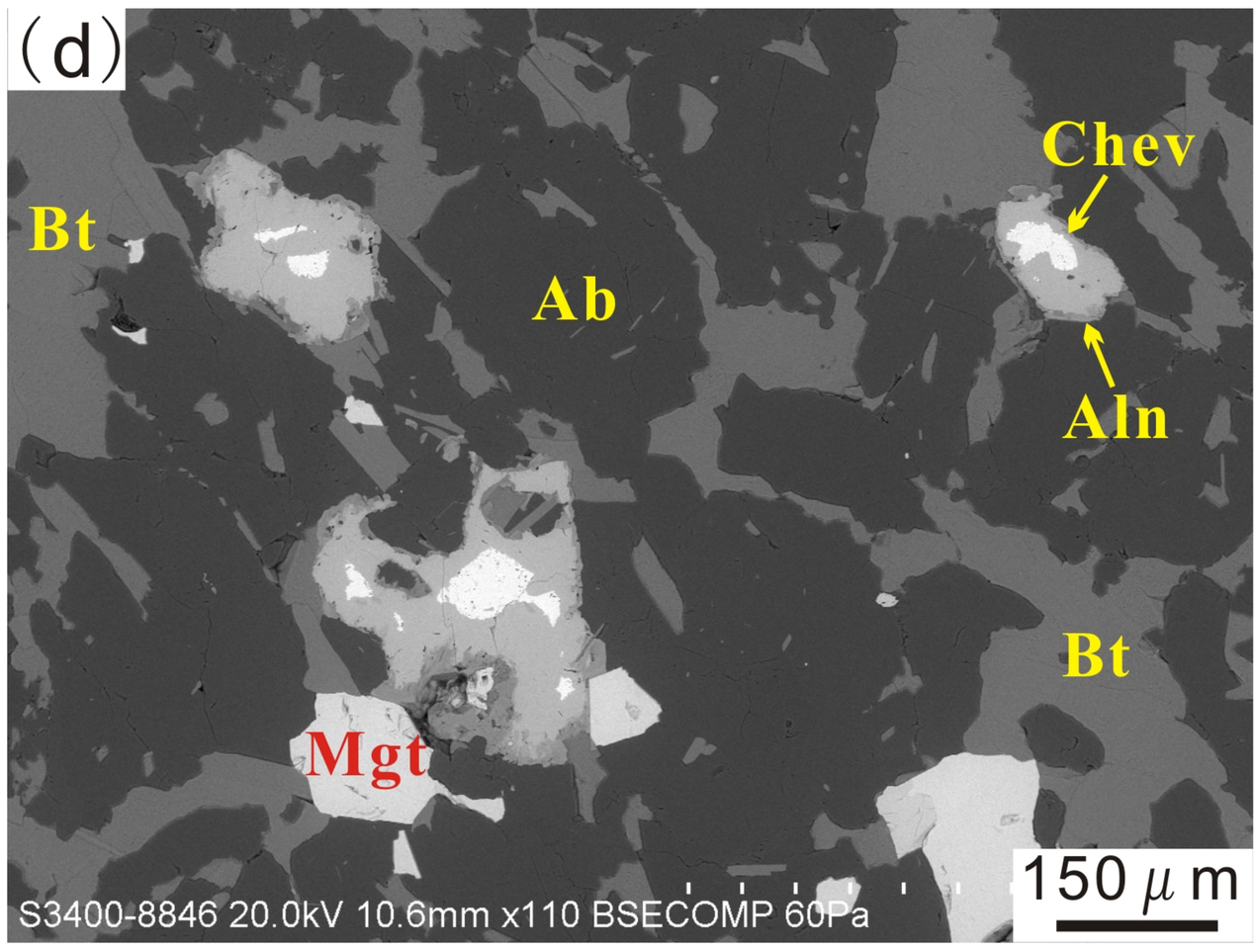
(d)
Chev
Bt
Ab
Aln
Bt
Mgt
150 μm
S3400-8846 20.0kV 10.6mm x110 BSECOMP 60Pa

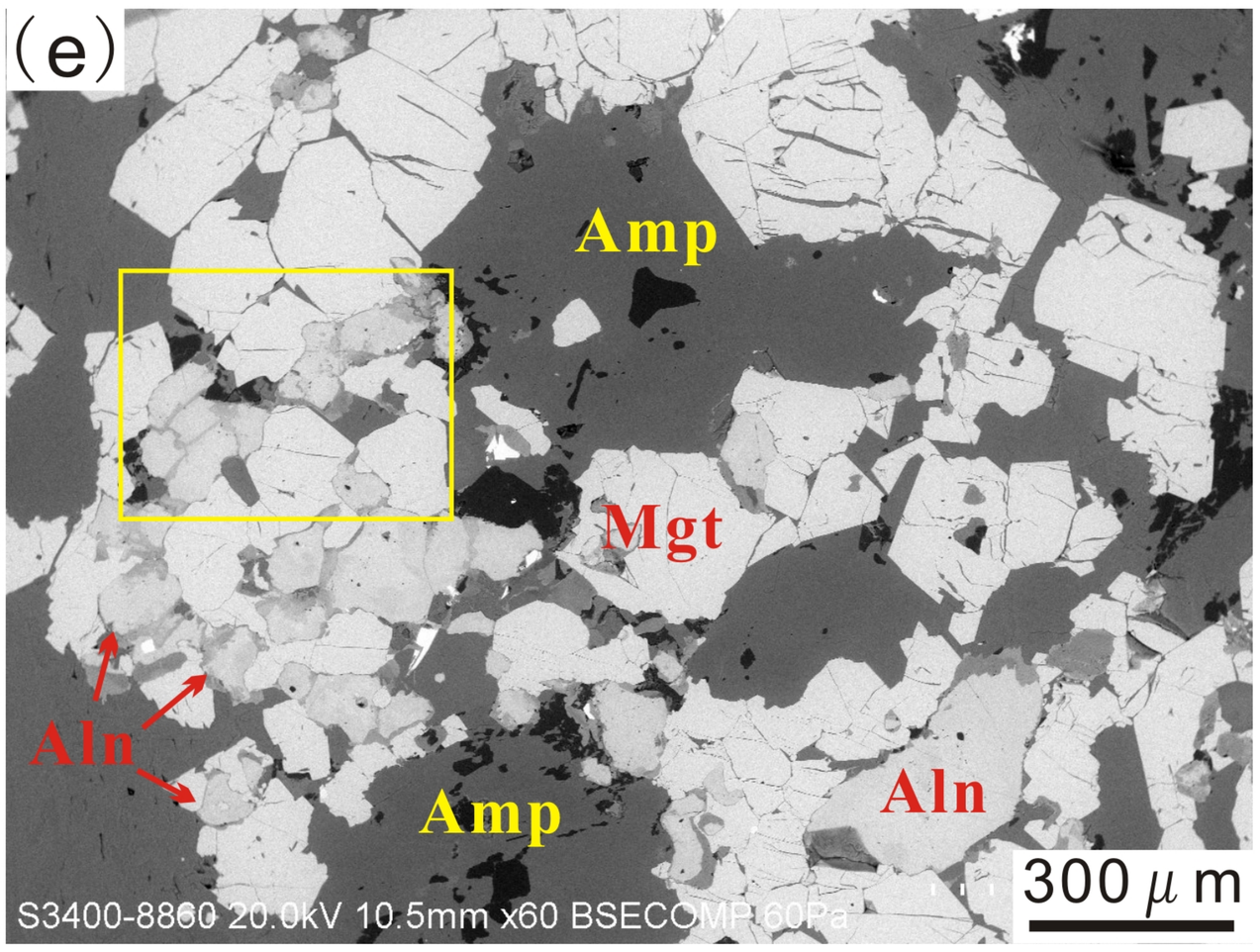
(e)
Amp
Mgt
Aln
Amp
Aln
300 μm
S3400-8860 20.0kV 10.5mm x60 BSECOMP 60Pa

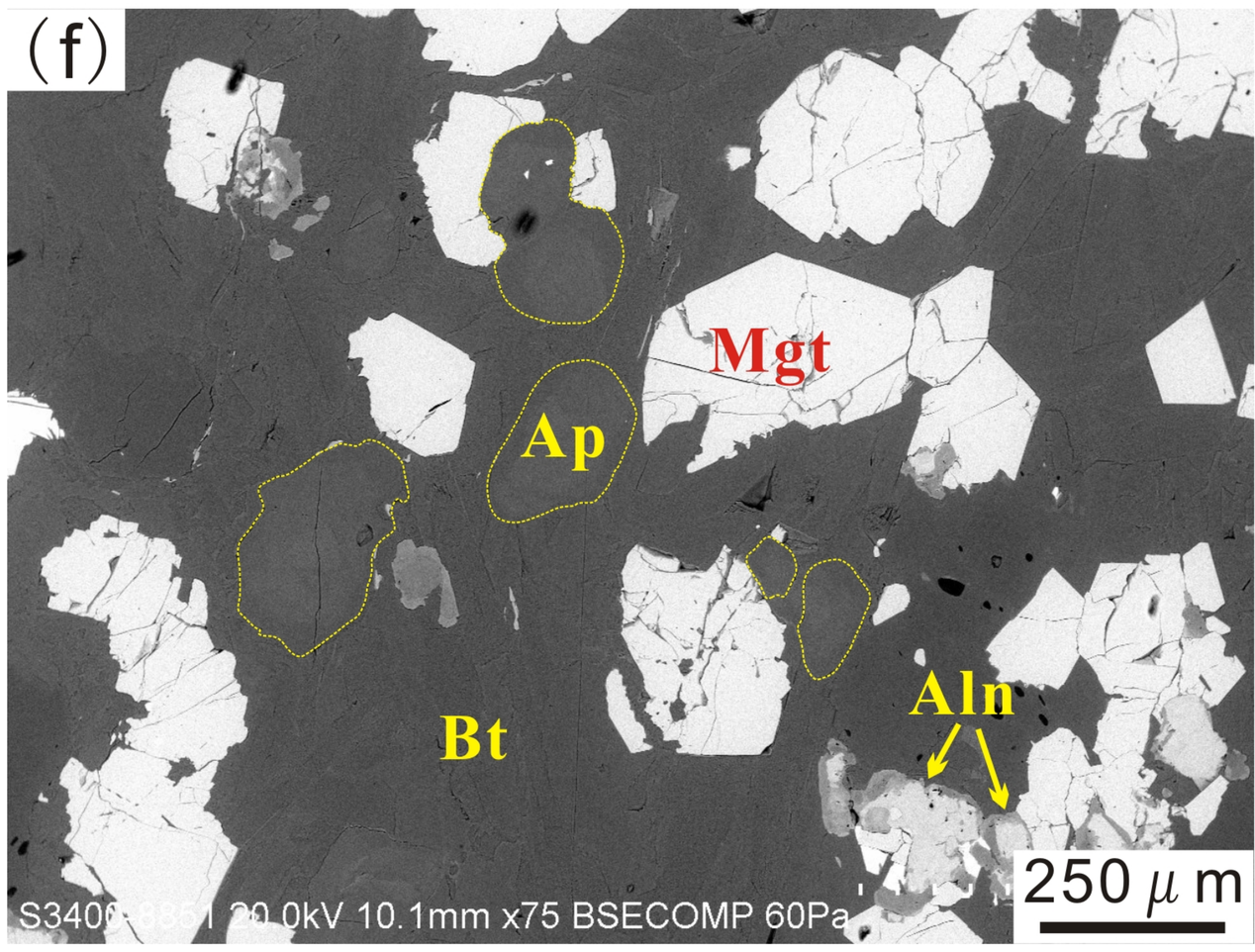
(f)
Mgt
Ap
Bt
Aln
250 μm
S3400-8851 20.0kV 10.1mm x75 BSECOMP 60Pa

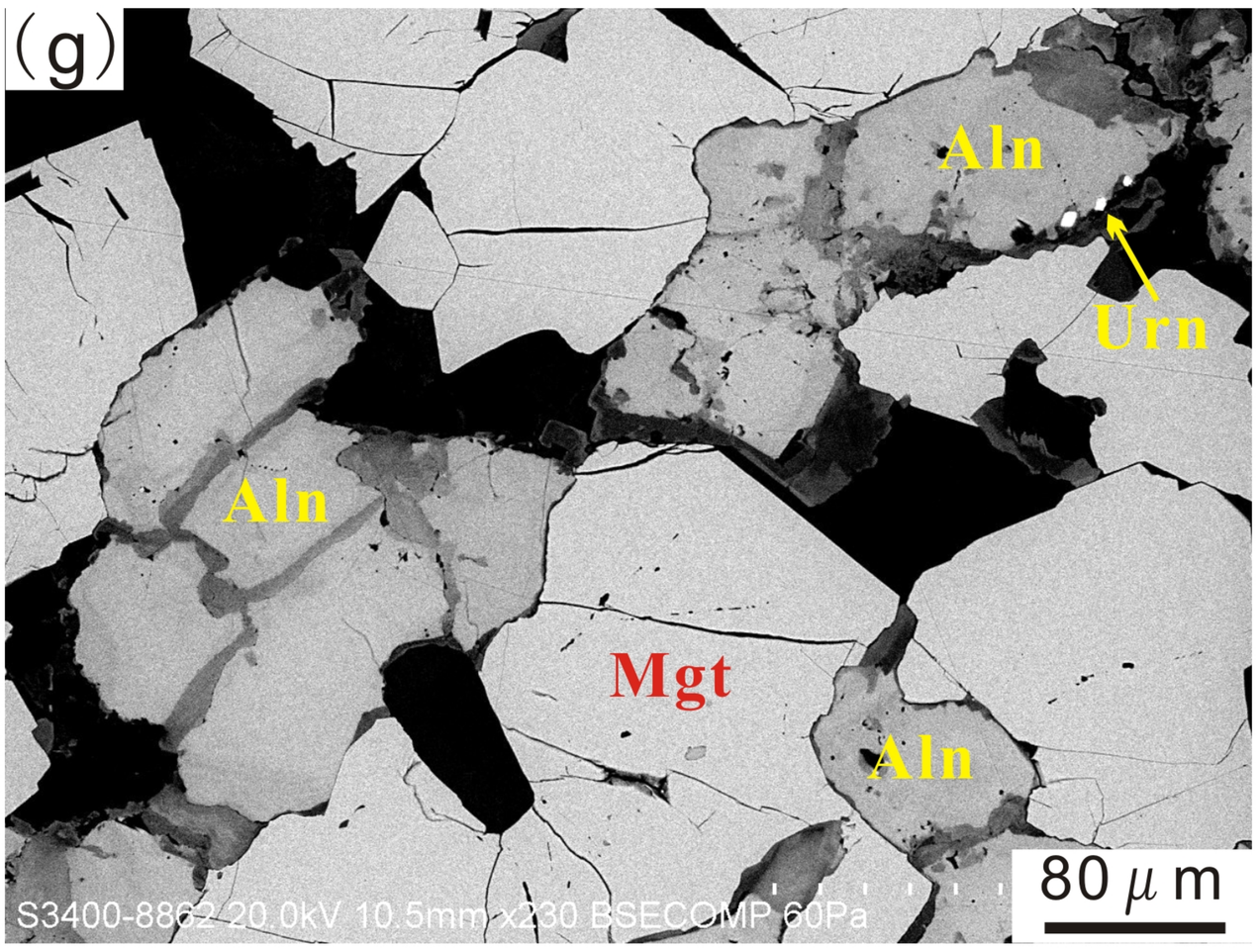
(g)
Aln
Urn
Aln
Mgt
Aln
80 μm
S3400-8862 20.0kV 10.5mm x230 BSECOMP 60Pa

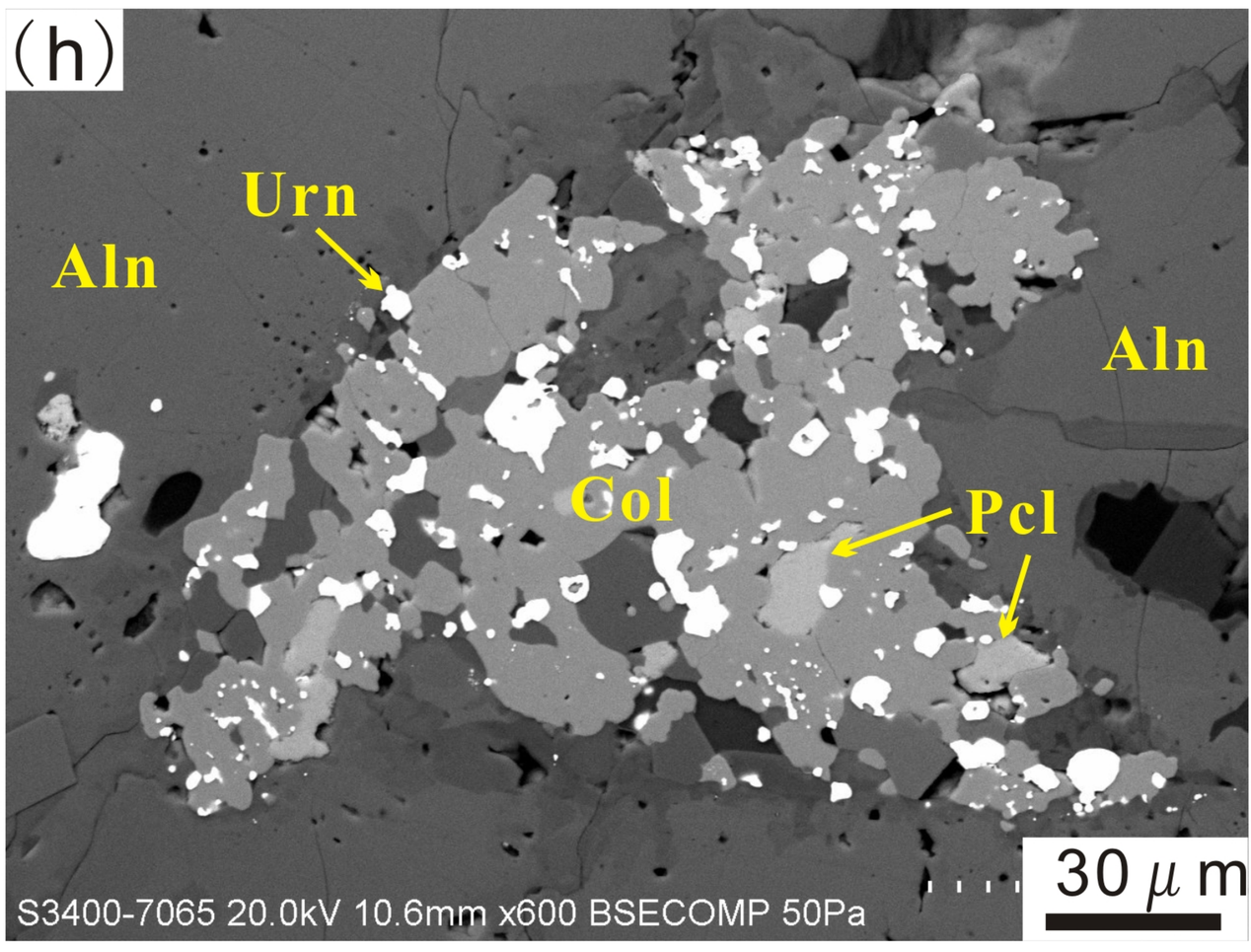
(h)
Urn
Aln
Aln
Col
Pcl
30 μm
S3400-7065 20.0kV 10.6mm x600 BSECOMP 50Pa

Fig. 3

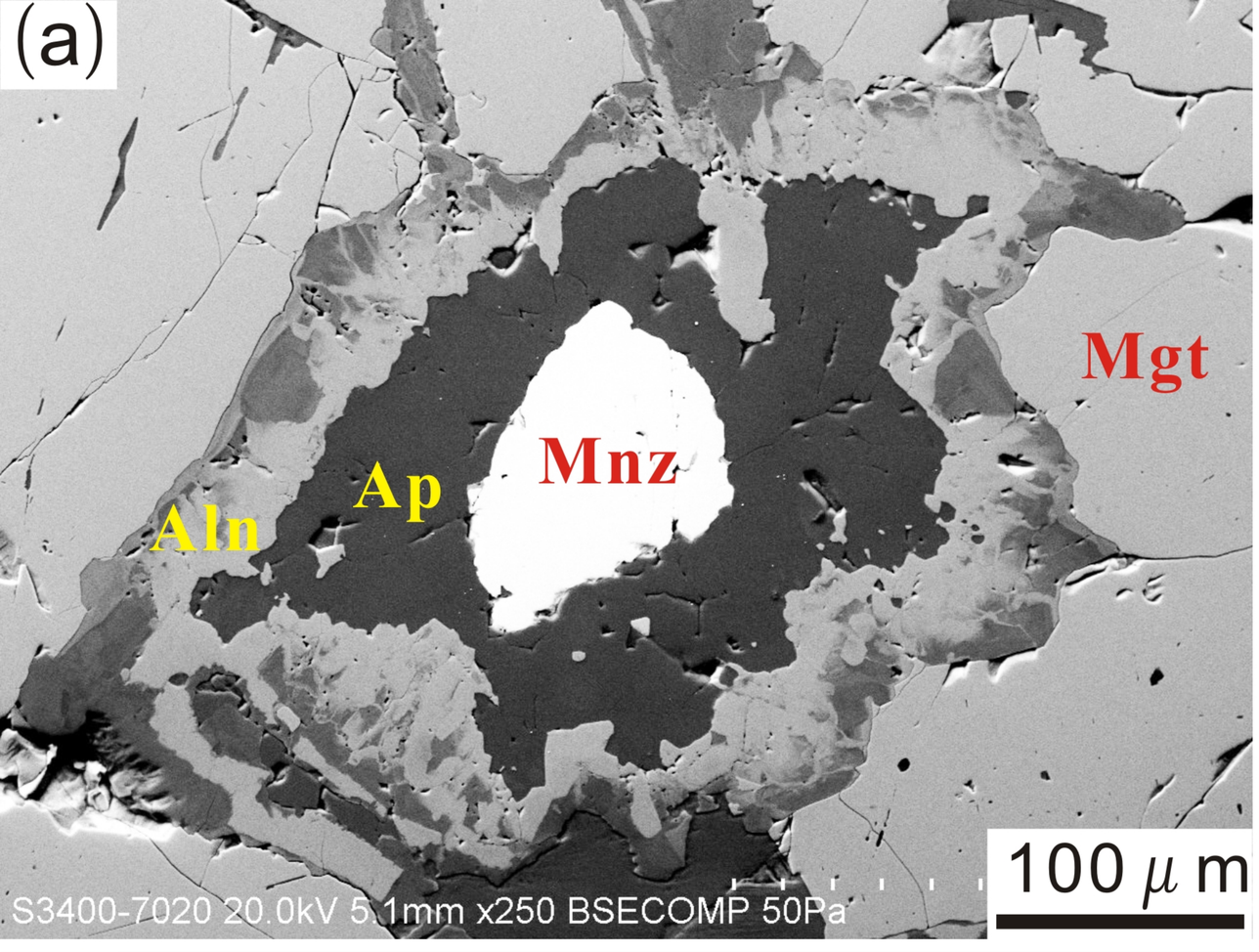
(a)
Aln
Ap
Mnz
Mgt
100 μm
S3400-7020 20.0kV 5.1mm x250 BSECOMP 50Pa

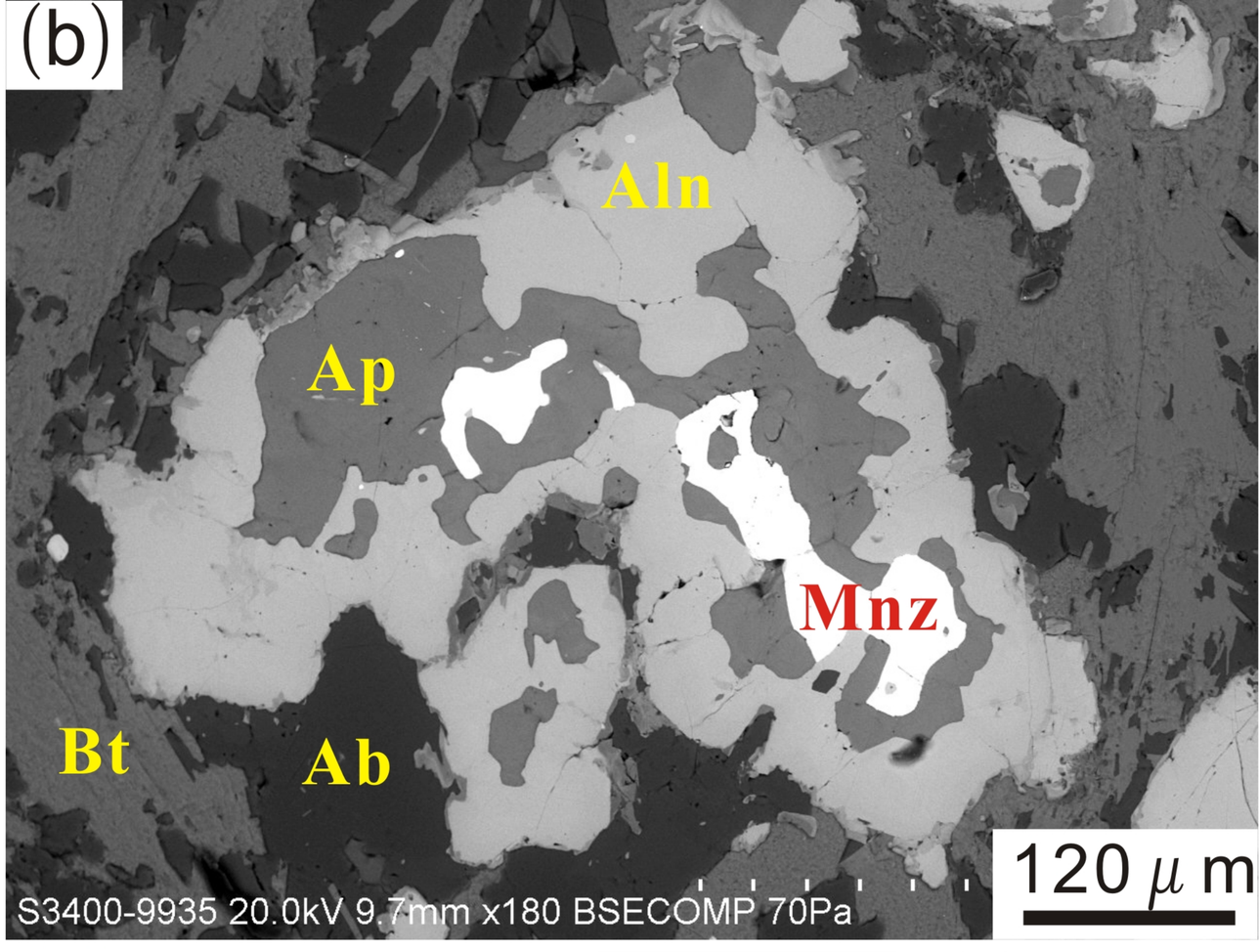
(b)
Aln
Ap
Mnz
Bt
Ab
120 μm
S3400-9935 20.0kV 9.7mm x180 BSECOMP 70Pa

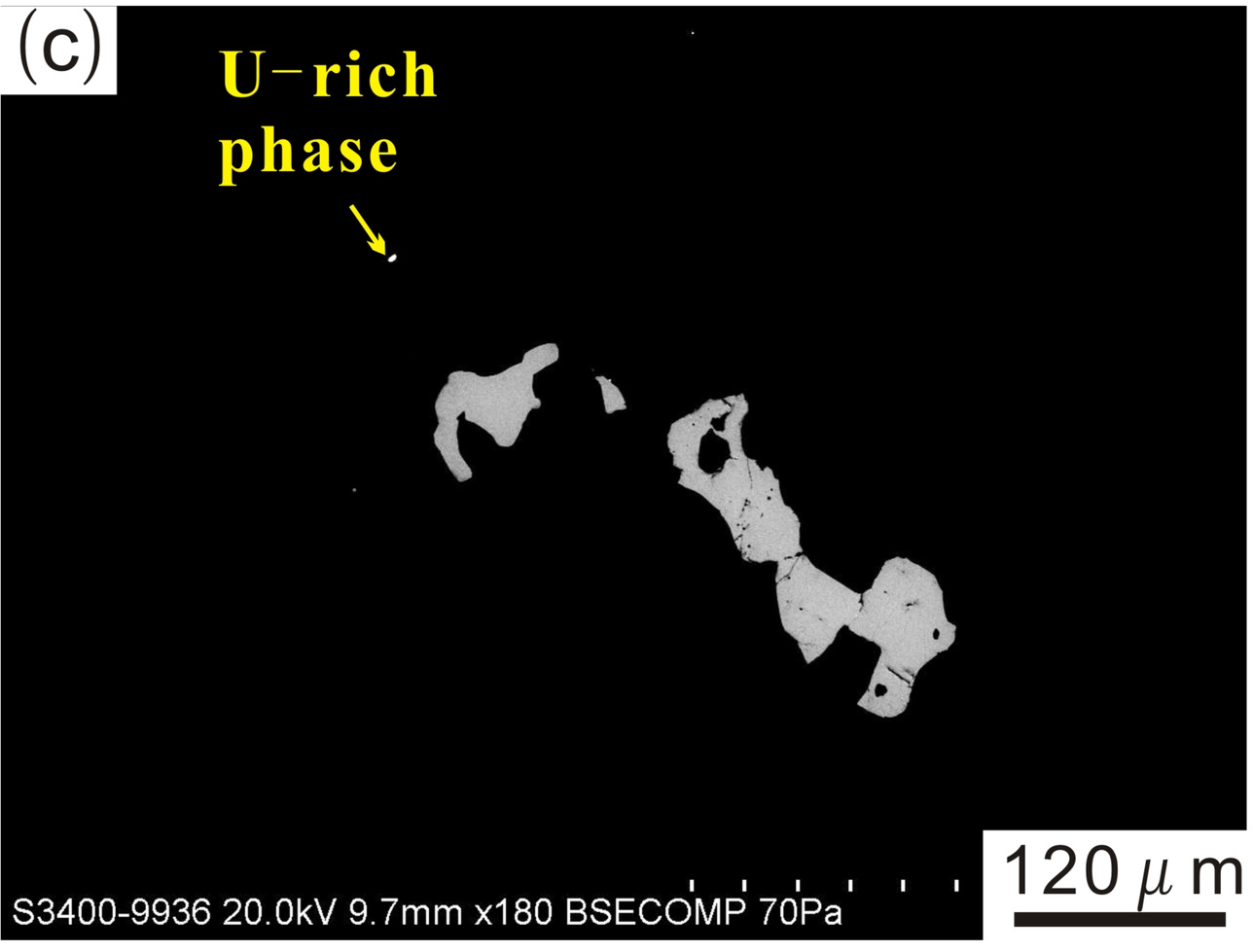
(c)
U-rich phase
120 μm
S3400-9936 20.0kV 9.7mm x180 BSECOMP 70Pa

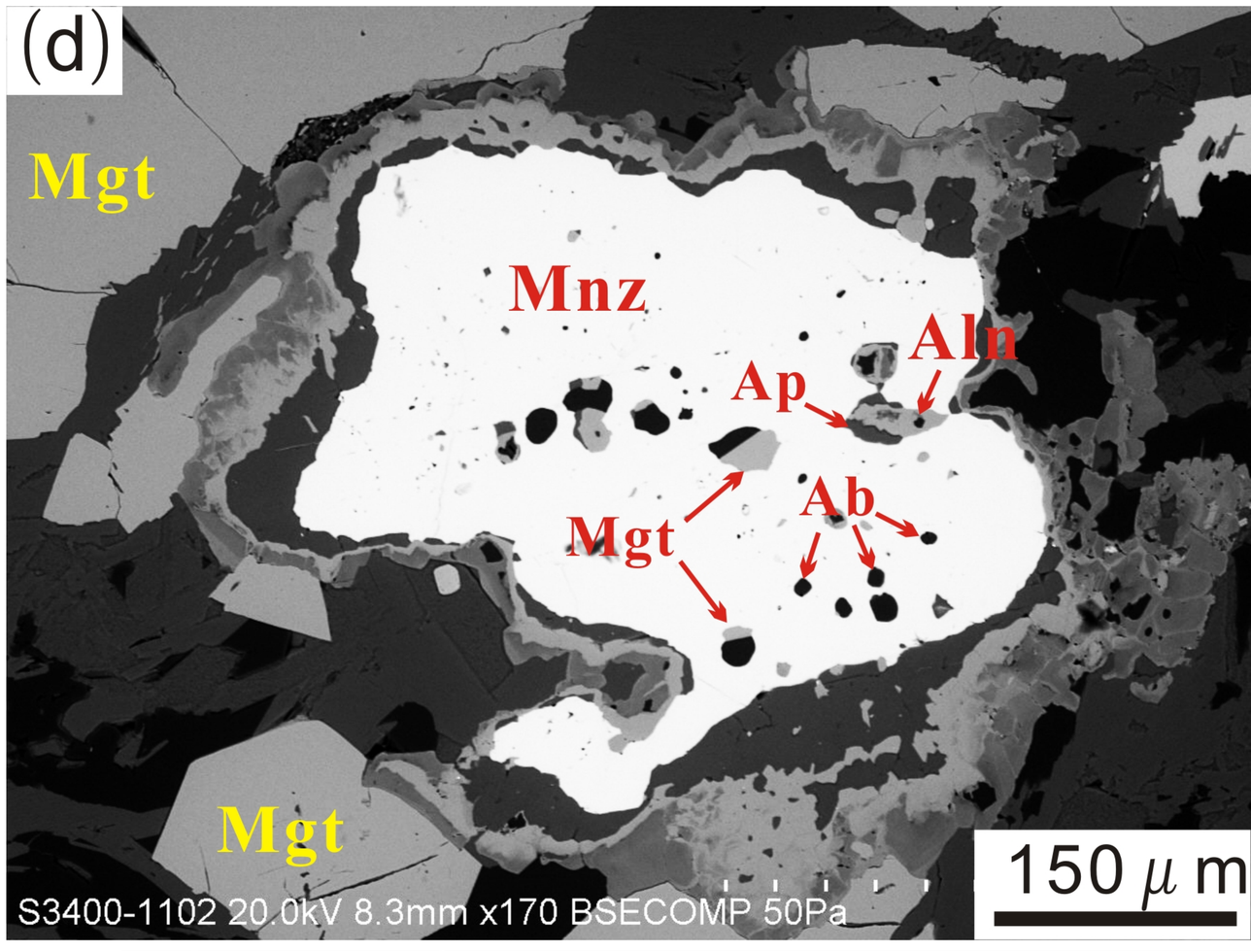
(d)
Mgt
Mnz
Aln
Ap
Ab
Mgt
Mgt
150 μm
S3400-1102 20.0kV 8.3mm x170 BSECOMP 50Pa

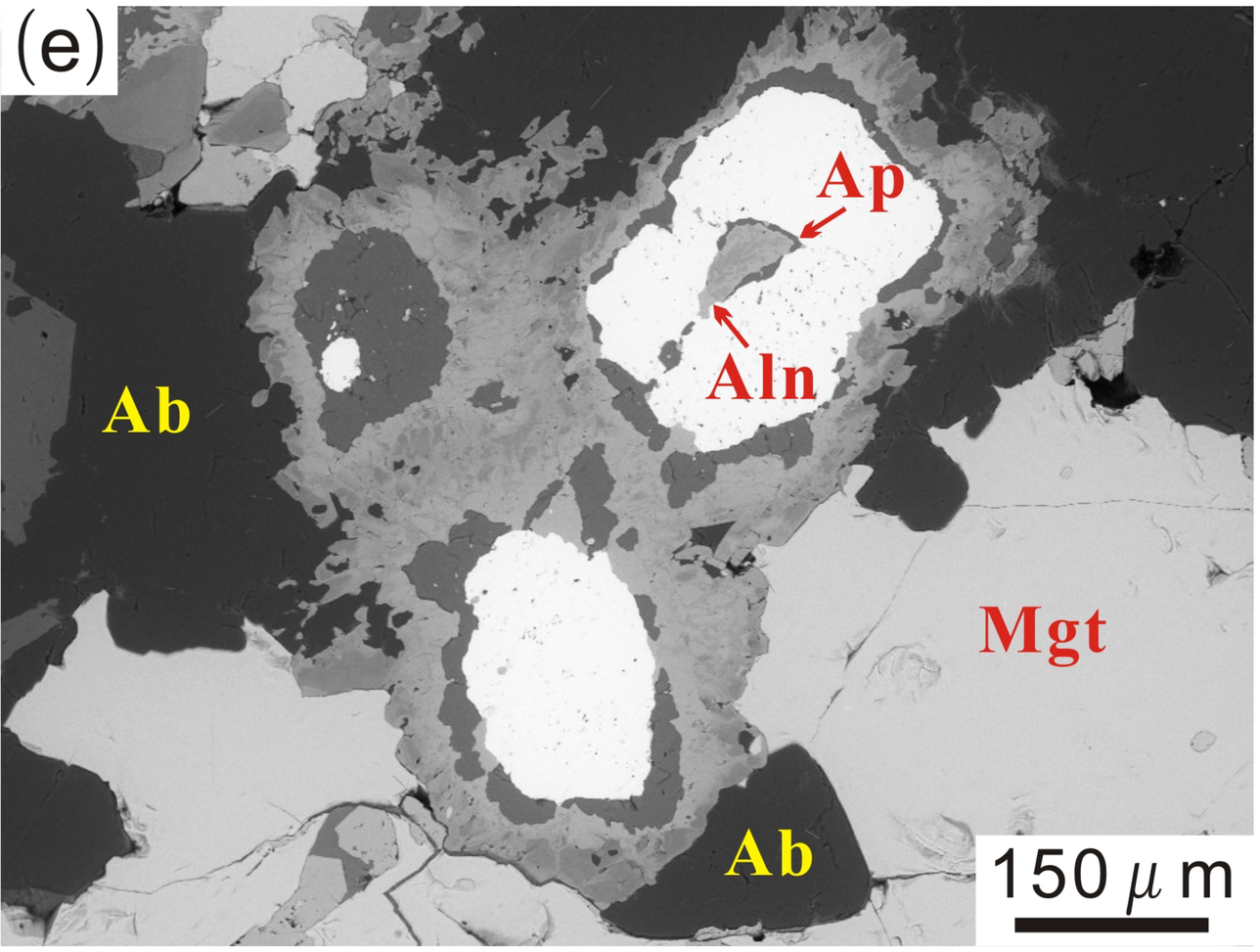
(e)
Ap
Aln
Ab
Mgt
Ab
150 μm

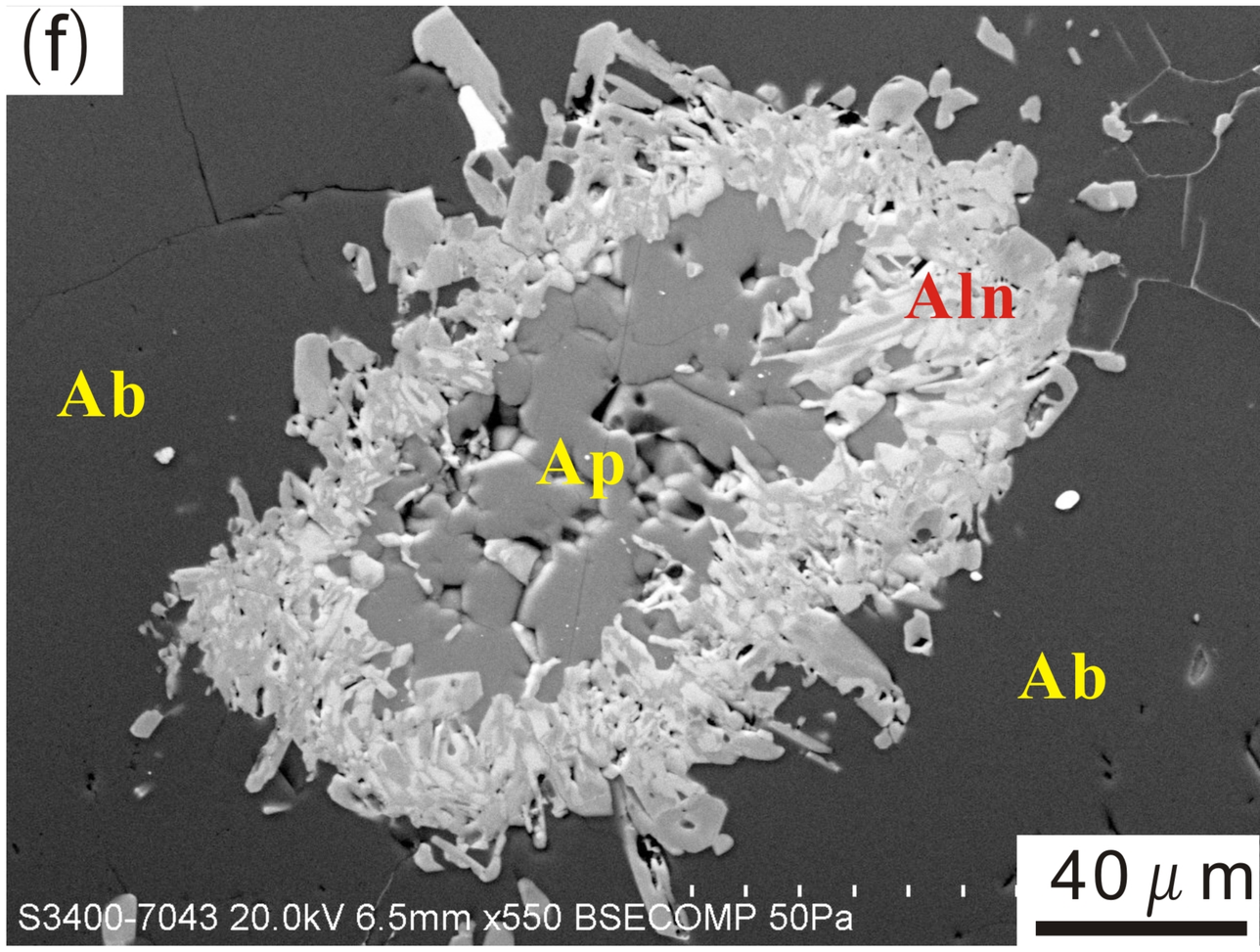
(f)
Aln
Ab
Ap
Ab
40 μm
S3400-7043 20.0kV 6.5mm x550 BSECOMP 50Pa

Fig. 4

(a)
Mgt
Aln(m)
Chev
Aes
80 μm
S3400-7080 20.0kV 8.4mm x320 BSECOMP 50Pa

(b)
Aln(m)
Chev
Ap
Mnz
200 μm
S3400-0472 20.0kV 9.5mm x120 BSECOMP 50Pa

(c)
Aln(m)
Chev
Mgt
50 μm
S3400-7084 20.0kV 6.5mm x450 BSECOMP 50Pa

(d)
Aln(s)
Chev
Aes
Aln(m)
20 μm
S3400-7057 20.0kV 6.4mm x1.00k BSECOMP 50Pa

(e)
Urn
Chev
Aln(m)
Aln(s)
Aes
50 μm
S3400-7042 20.0kV 7.4mm x350 BSECOMP 50Pa

(f)
Aln(m)
Aes
Aln(s)
20 μm
S3400-7078 20.0kV 7.7mm x950 BSECOMP 50Pa

(g)
Aln(m)
Bast
Ilm
Aes
Aln(s)
50 μm
S3400-7009 20.0kV 5.3mm x450 BSECOMP 50Pa

(h)
Aln(m)
Chev
Aln(s)
Mgt
150 μm
S3400-7036 20.0kV 5.5mm x150 BSECOMP 50Pa

Fig. 5

(a)

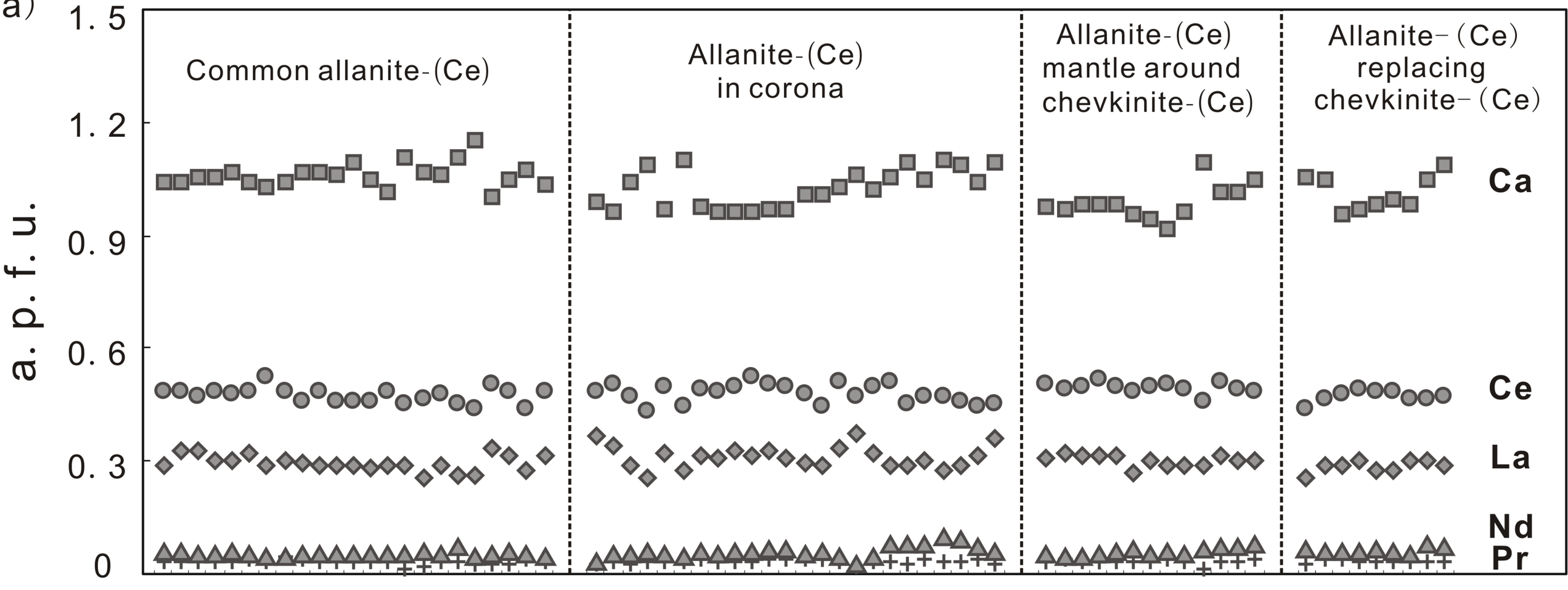
1. 5
1. 2
0. 9
0. 6
0. 3
0
a. p. f. u.
Common allanite-(Ce)
Allanite-(Ce) in corona
Allanite-(Ce) mantle around chevkinite-(Ce)
Allanite-(Ce) replacing chevkinite-(Ce)
Ca
Ce
La
Nd
Pr

(b)

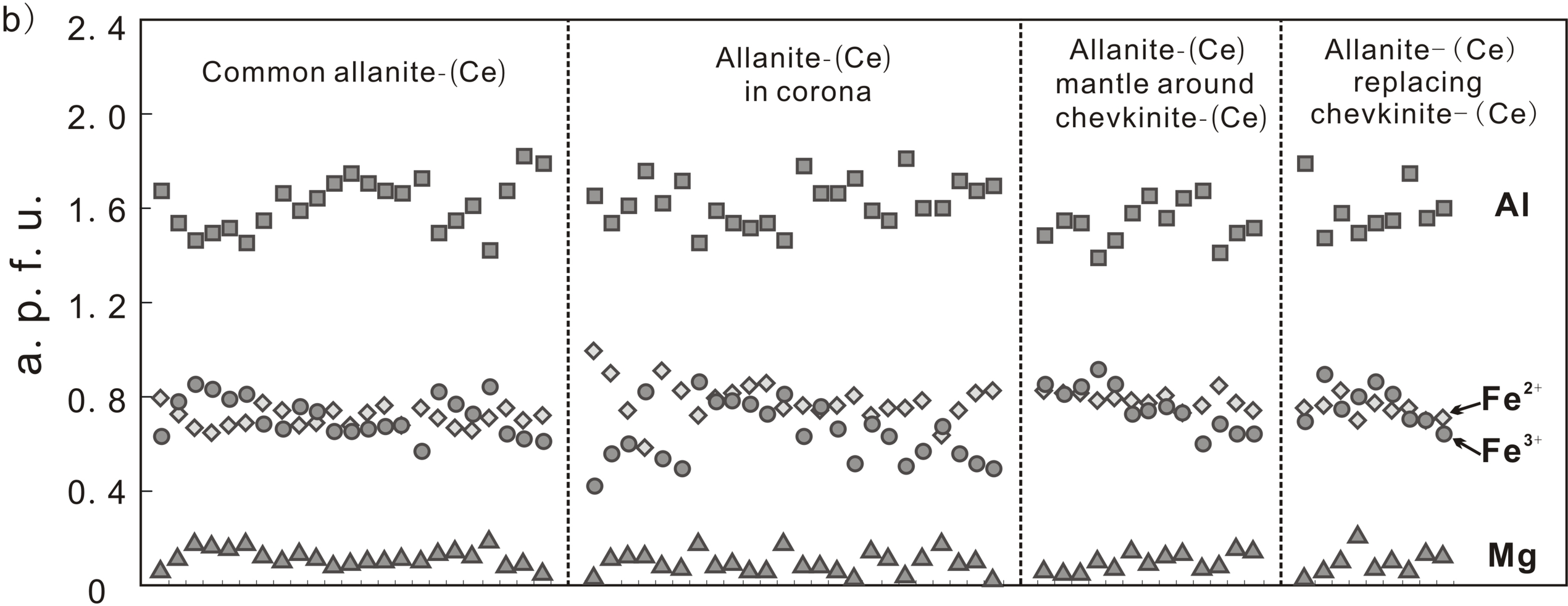
2. 4
2. 0
1. 6
1. 2
0. 8
0. 4
0
a. p. f. u.
Common allanite-(Ce)
Allanite-(Ce) in corona
Allanite-(Ce) mantle around chevkinite-(Ce)
Allanite-(Ce) replacing chevkinite-(Ce)
Al
Fe2+
Fe3+
Mg

Fig. 6

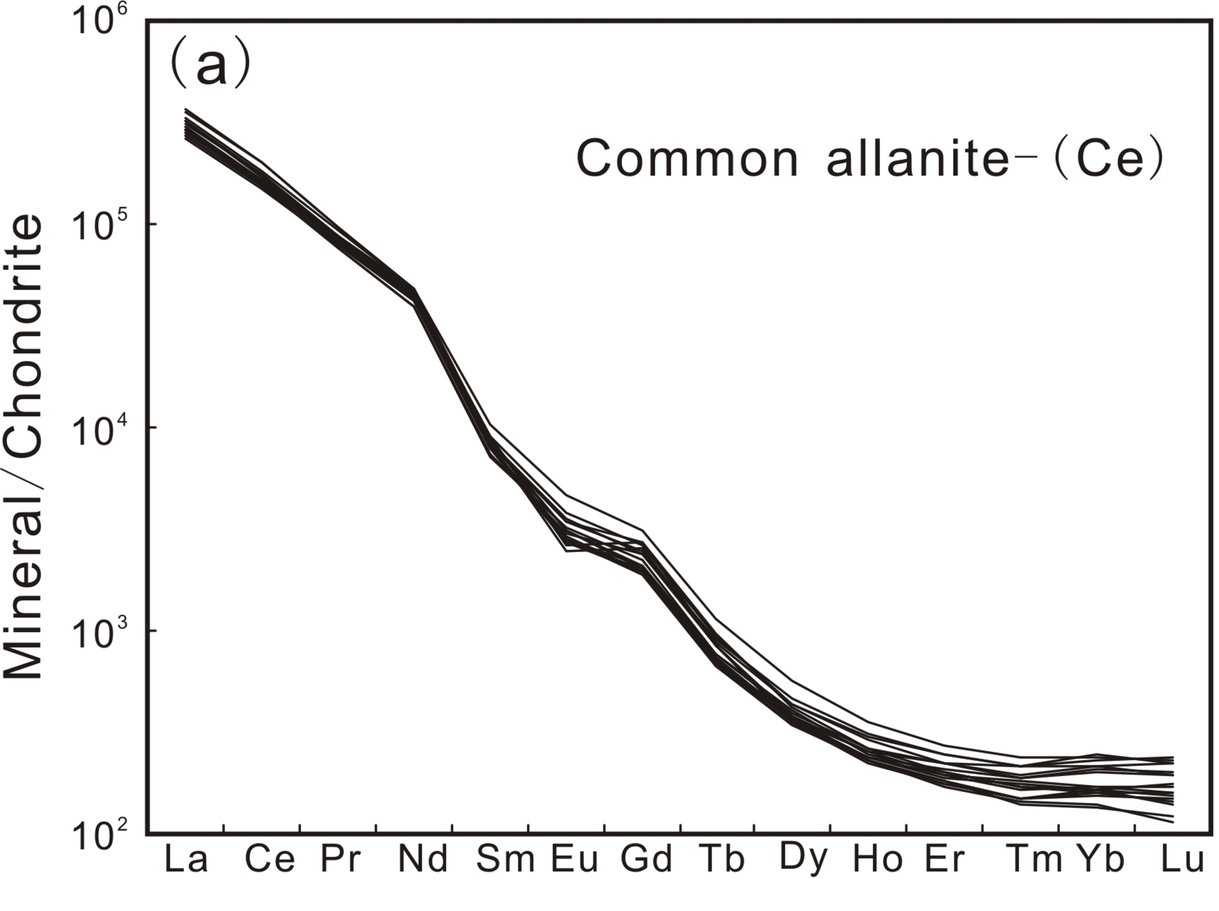
(a)
Common allanite-(Ce)
Mineral/Chondrite
10^6
10^5
10^4
10^3
10^2
La Ce Pr Nd Sm Eu Gd Tb Dy Ho Er Tm Yb Lu

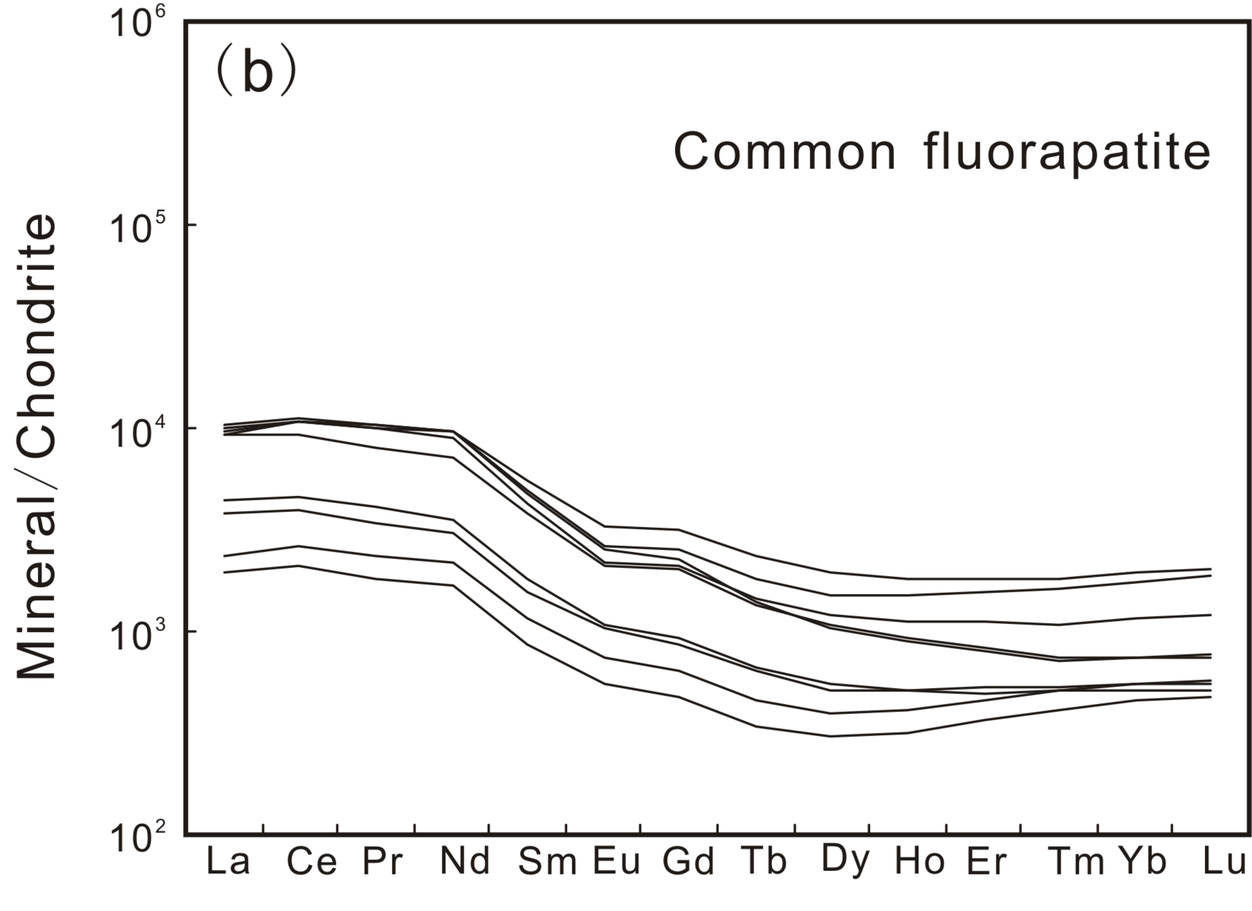
(b)
Common fluorapatite
Mineral/Chondrite
10^6
10^5
10^4
10^3
10^2
La Ce Pr Nd Sm Eu Gd Tb Dy Ho Er Tm Yb Lu

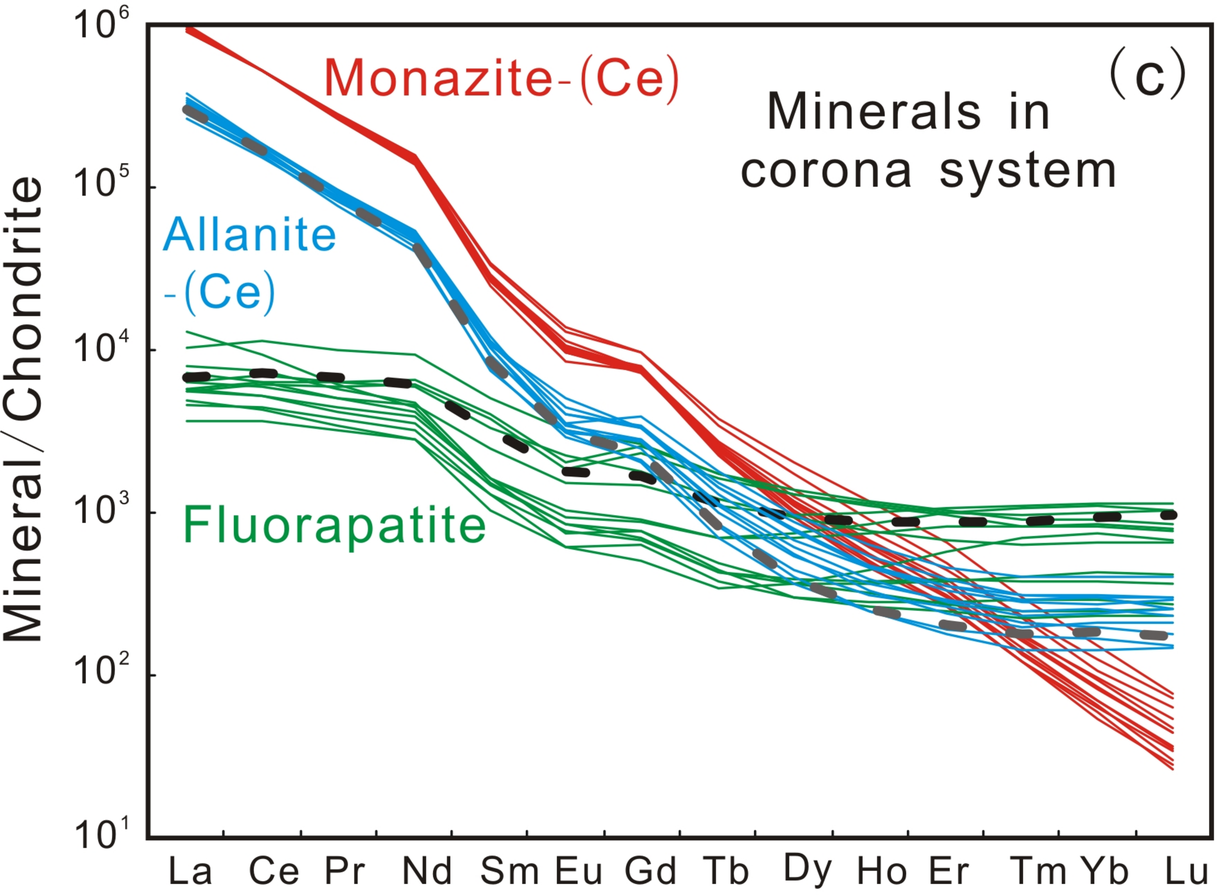
(c)
Minerals in corona system
Monazite-(Ce)
Allanite -(Ce)
Fluorapatite
Mineral/Chondrite
10^6
10^5
10^4
10^3
10^2
10^1
La Ce Pr Nd Sm Eu Gd Tb Dy Ho Er Tm Yb Lu

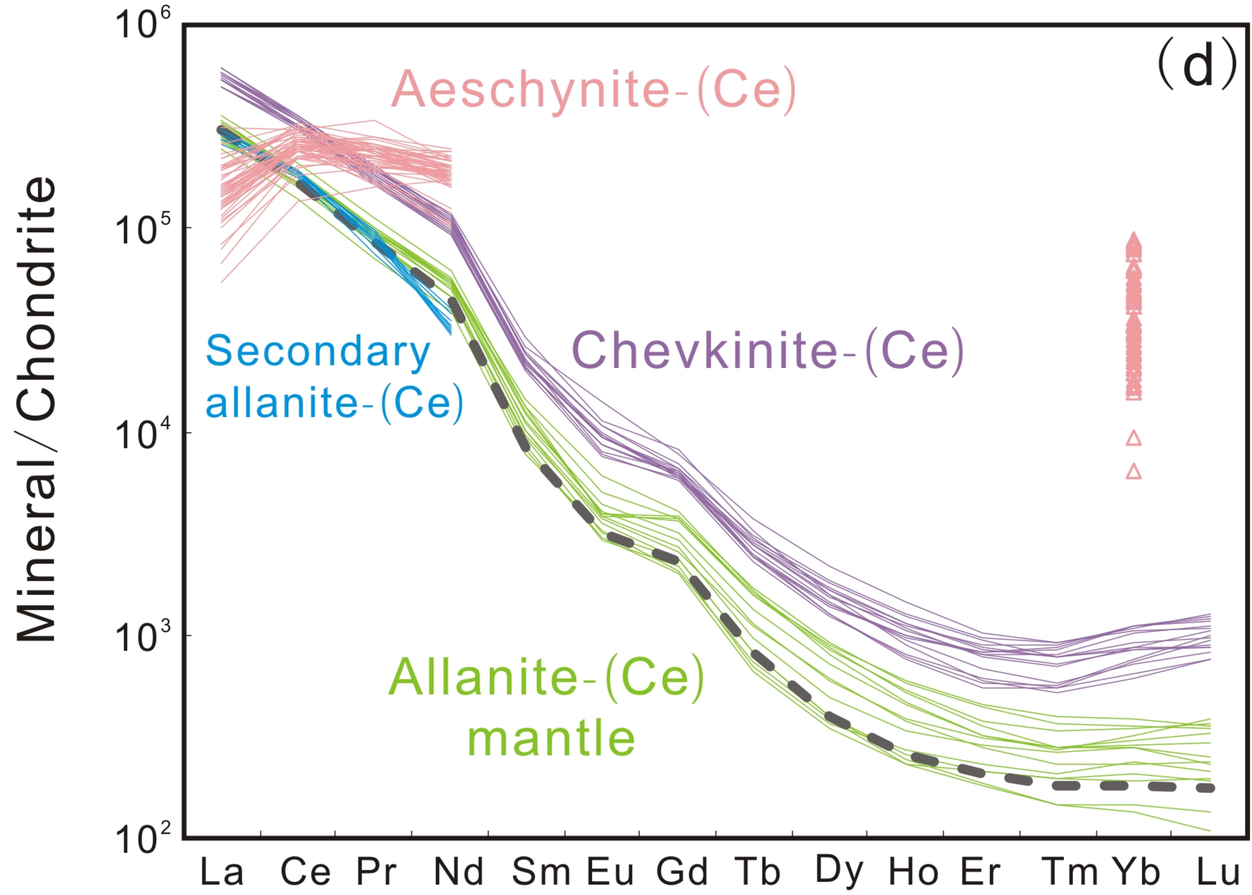
(d)
Aeschynite-(Ce)
Secondary allanite-(Ce)
Chevkinite-(Ce)
Allanite-(Ce) mantle
Mineral/Chondrite
10^6
10^5
10^4
10^3
10^2
La Ce Pr Nd Sm Eu Gd Tb Dy Ho Er Tm Yb Lu

Fig. 7

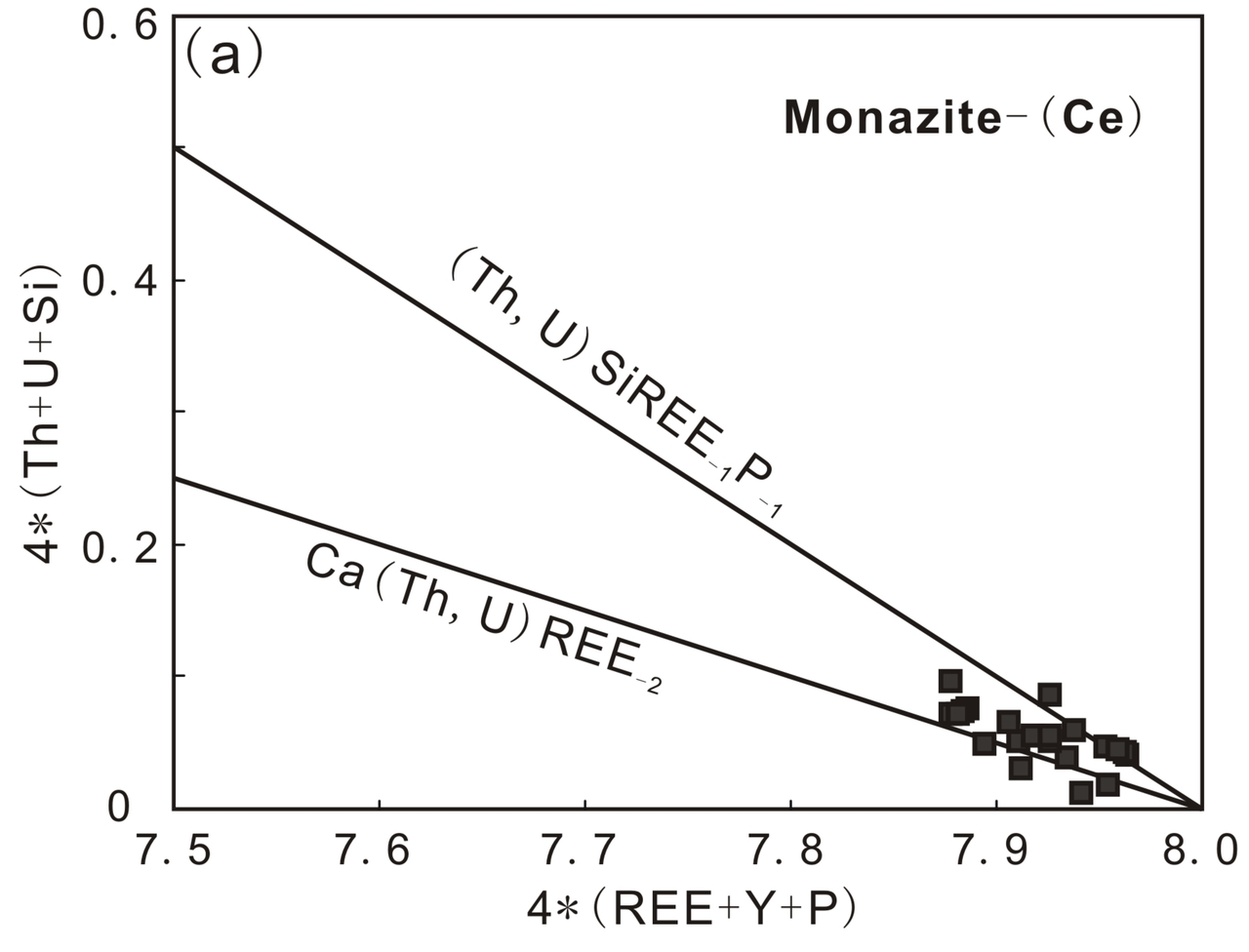
(a)
Monazite-(Ce)
(Th, U) SiREE$_{-1}$P$_{-1}$
Ca (Th, U) REE$_{-2}$
4*(Th+U+Si)
4*(REE+Y+P)
0.6
0.4
0.2
0
7.5
7.6
7.7
7.8
7.9
8.0

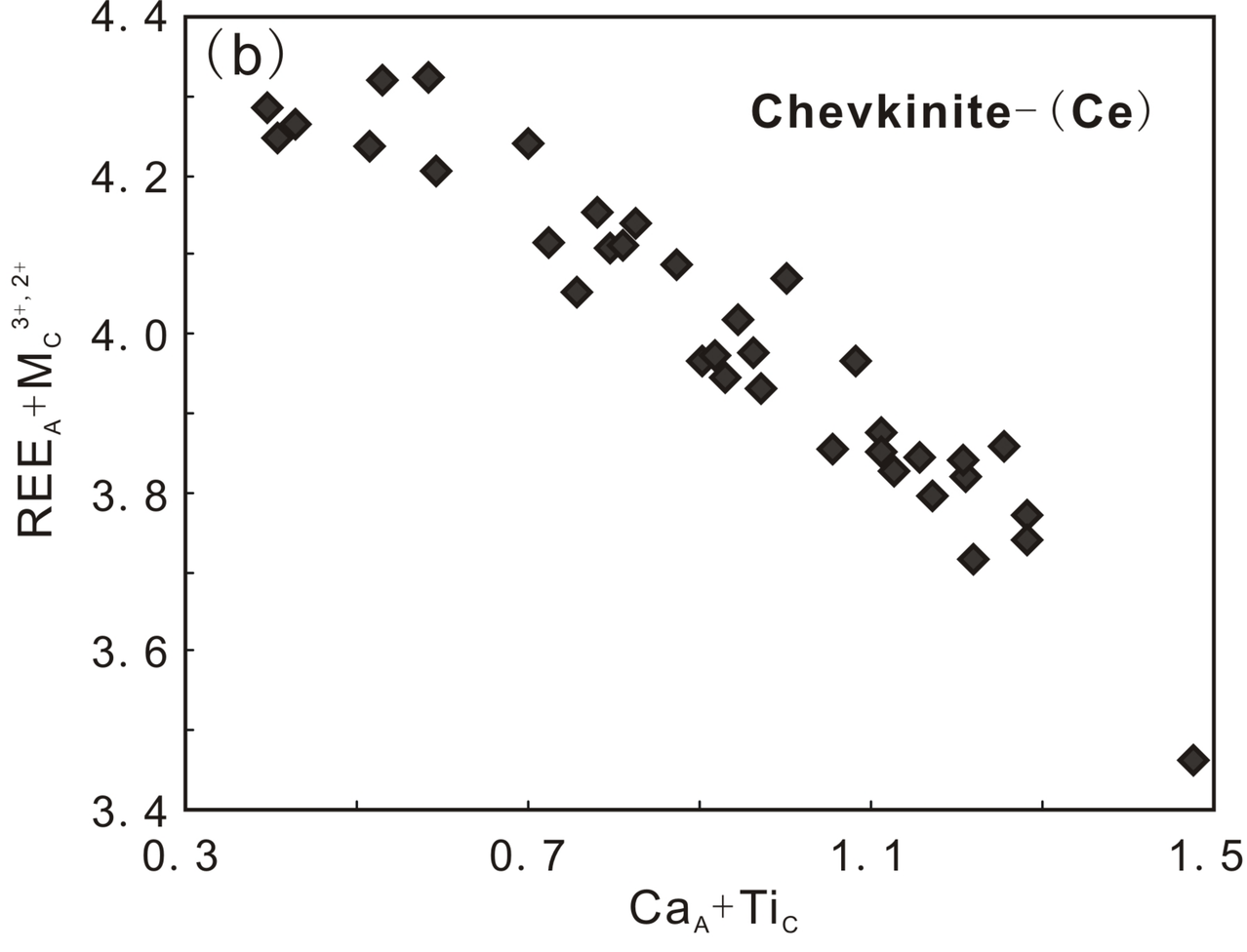
(b)
Chevkinite-(Ce)
REE$_A$+M$_C^{3+,2+}$
Ca$_A$+Ti$_C$
4.4
4.2
4.0
3.8
3.6
3.4
0.3
0.7
1.1
1.5

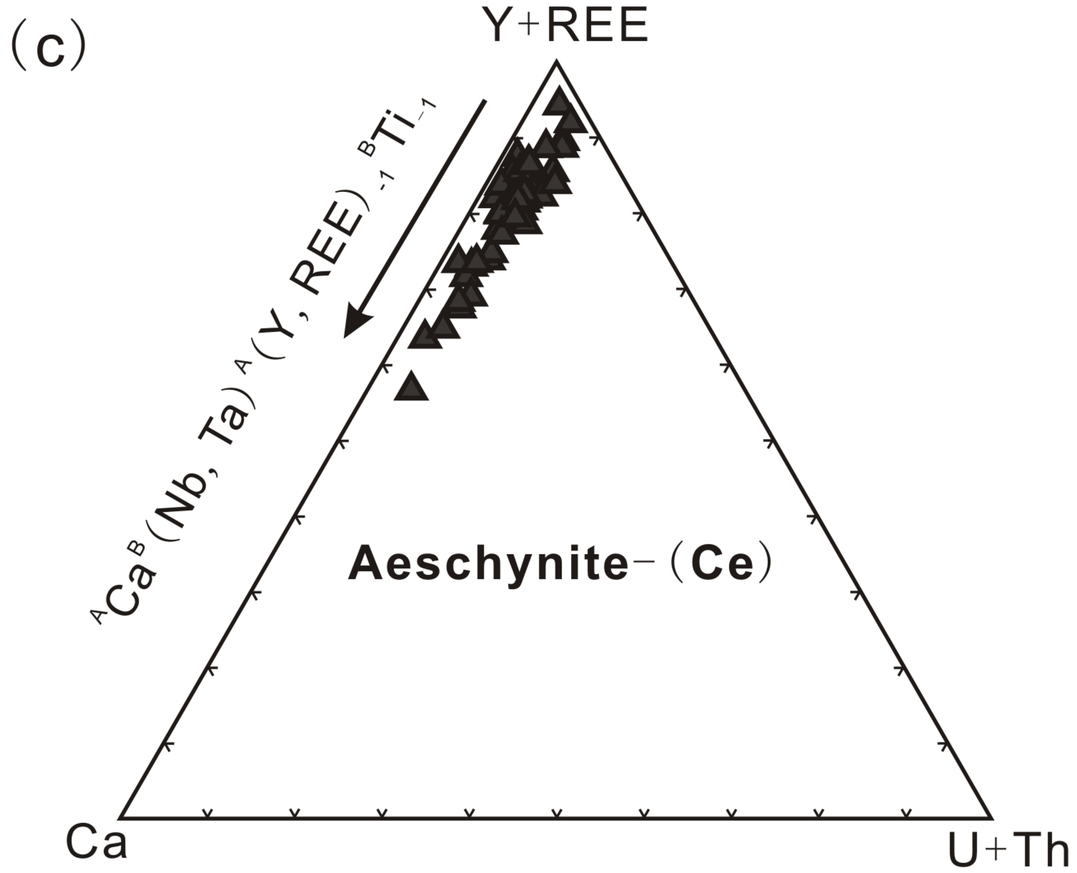
(c)
Y+REE
^{A}Ca^B(Nb, Ta)^A(Y, REE)$_{-1}$^{B}Ti$_{-1}$
Aeschynite-(Ce)
Ca
U+Th

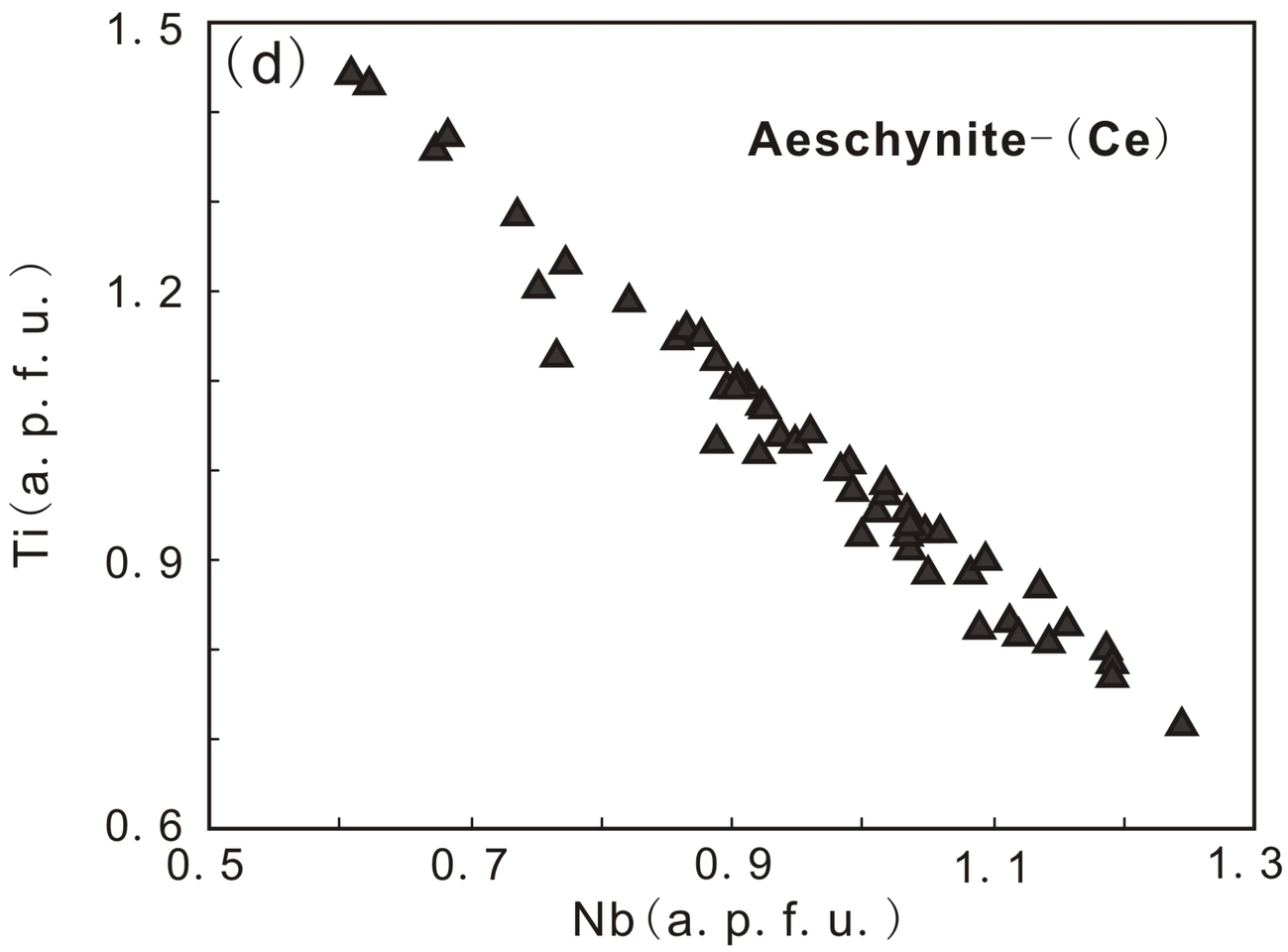
(d)
Aeschynite-(Ce)
Ti (a. p. f. u.)
Nb (a. p. f. u.)
1.5
1.2
0.9
0.6
0.5
0.7
0.9
1.1
1.3

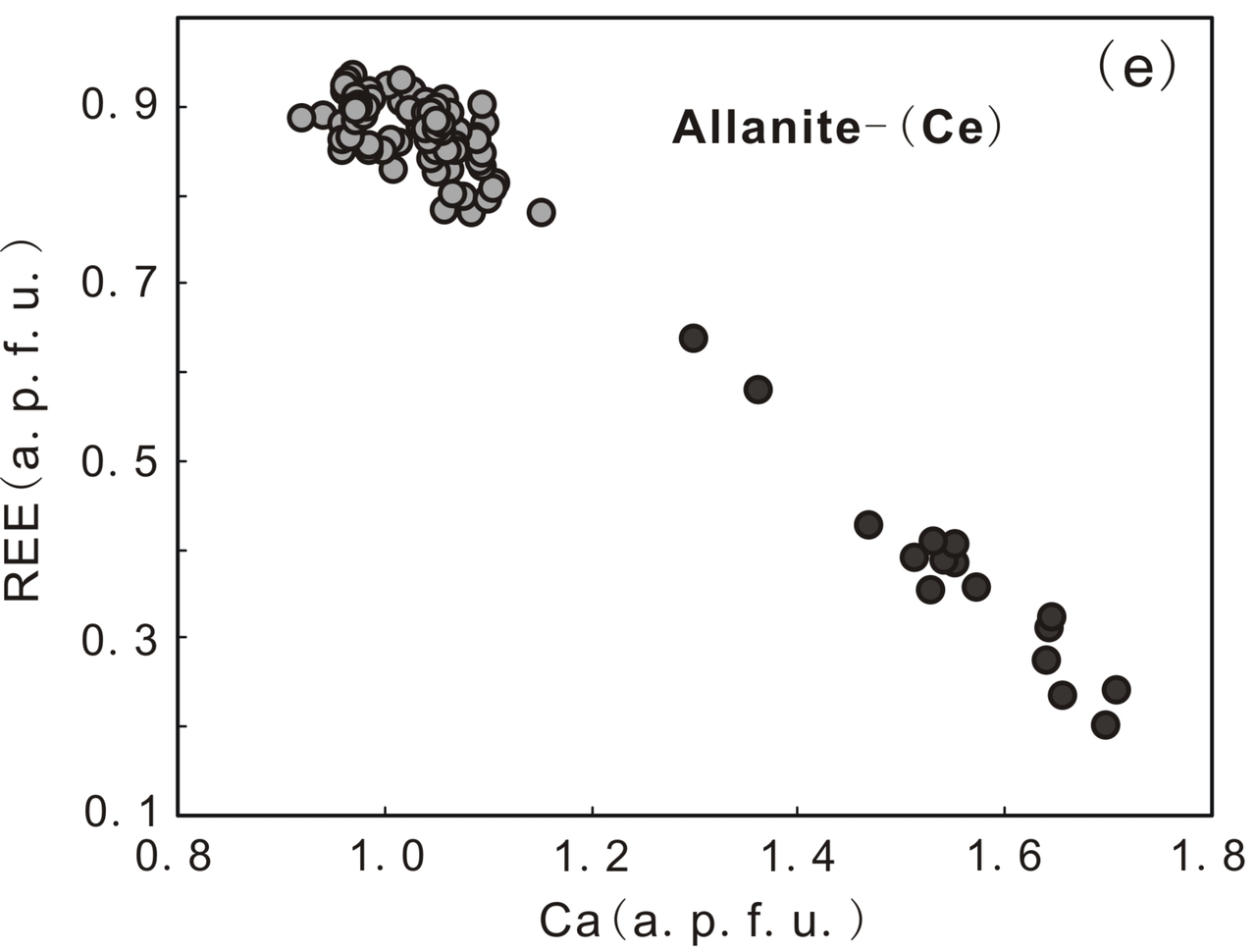
(e)
Allanite-(Ce)
REE (a. p. f. u.)
Ca (a. p. f. u.)
0.9
0.7
0.5
0.3
0.1
0.8
1.0
1.2
1.4
1.6
1.8

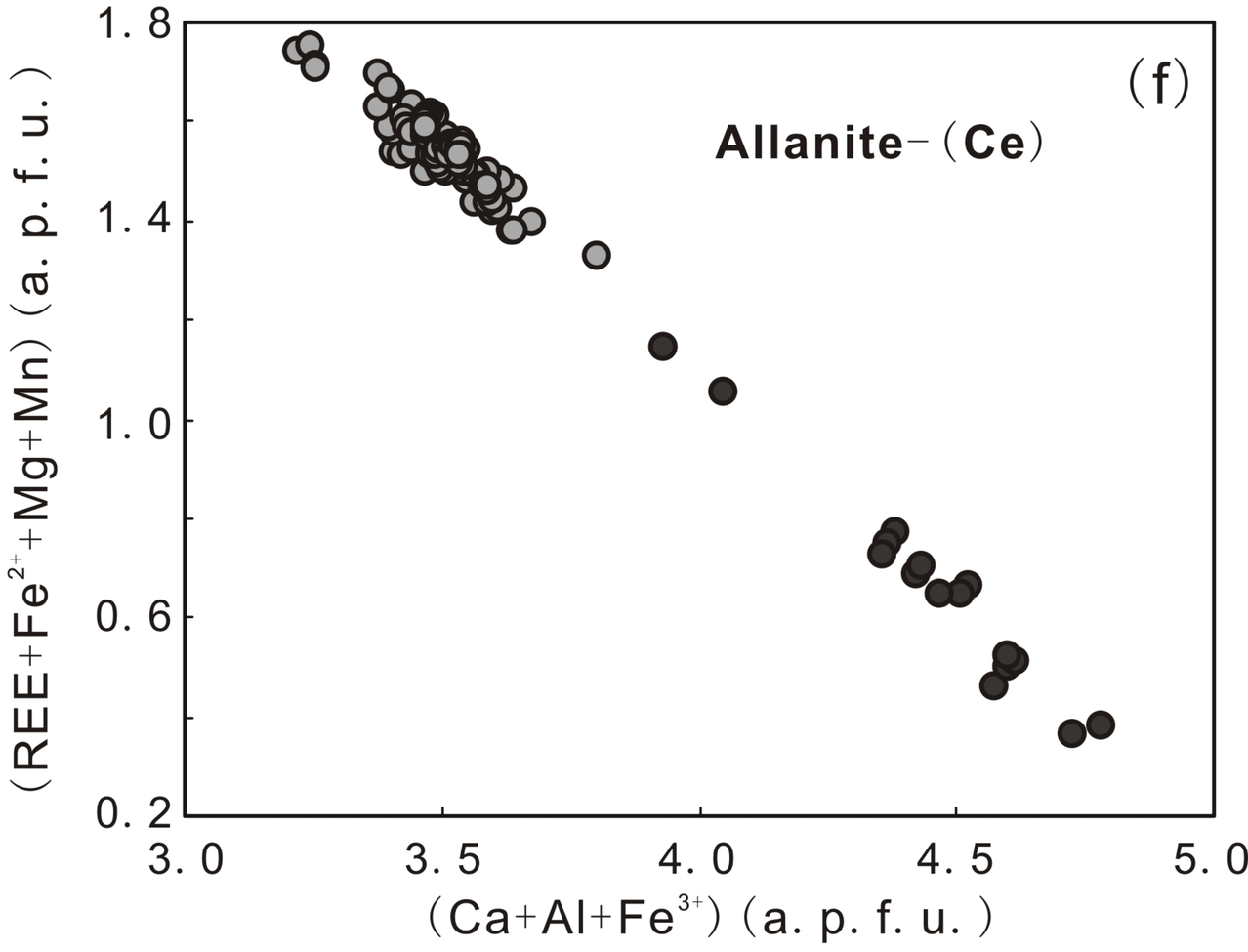
(f)
Allanite-(Ce)
(REE+Fe^{2+}+Mg+Mn) (a. p. f. u.)
(Ca+Al+Fe^{3+}) (a. p. f. u.)
1.8
1.4
1.0
0.6
0.2
3.0
3.5
4.0
4.5
5.0

Fig. 8

N=10

Common allanite-(Ce)

N=6

Allanite-(Ce) in corona

N=8

Allanite-(Ce) mantle around chevkinite-(Ce)

-6 -5 -4 -3 -2 -1 0

$\varepsilon_{Nd}(t)$

Fig. 9

(a)

(Ap:Aln)$_{area}$=21:79

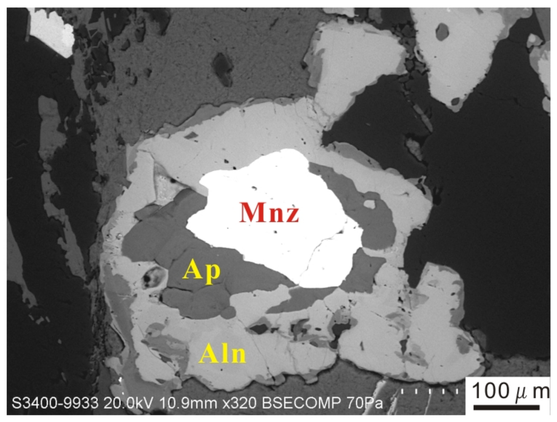

Enrichment factor (relative to Th)

100 / 10 / 1 / 0.1

P 0.64 | La 0.66 | Ce 0.70 | Pr 0.84 | Nd 0.63 | Sm 0.80 | Eu 0.96 | Gd 0.90 | Tb 1.25 | Dy 1.56 | Ho 1.95 | Y 2.06 | Er 2.81 | Tm 5.31 | Yb 10.3 | Lu 19.5 | Nb 8.01 | Ta 11.9 | Zr 5.45 | Hf 3.43 | Sr 86.7 | Ge 0.73 | As 0.50 | U 0.49

(b)

(Ap:Aln)$_{area}$=31:69

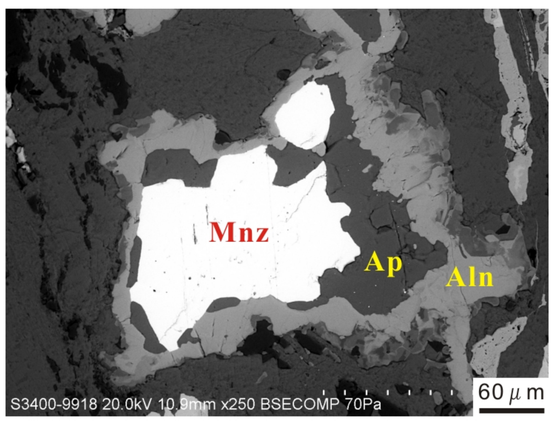

Enrichment factor (relative to Th)

100 / 10 / 1 / 0.1

P 0.75 | La 0.59 | Ce 0.52 | Pr 0.43 | Nd 0.35 | Sm 0.66 | Eu 0.55 | Gd 0.81 | Tb 1.14 | Dy 1.37 | Ho 1.72 | Y 1.72 | Er 2.37 | Tm 4.63 | Yb 8.90 | Lu 16.1 | Nb 3.23 | Ta 6.03 | Zr 4.20 | Hf 10.1 | Sr 66.0 | Ge 0.56 | As 0.51 | U 0.31

(c)

(Ap:Aln)$_{area}$=39:61

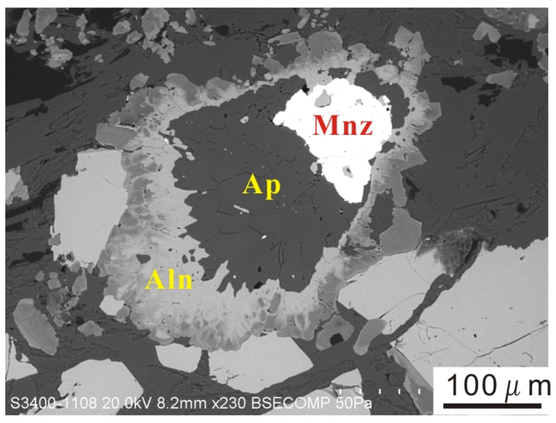

Enrichment factor (relative to Th)

100 / 10 / 1 / 0.1

P 1.19 | La 0.54 | Ce 0.59 | Pr 0.59 | Nd 0.70 | Sm 0.68 | Eu 0.64 | Gd 0.66 | Tb 0.93 | Dy 1.37 | Ho 2.04 | Y 2.05 | Er 3.22 | Tm 6.57 | Yb 13.0 | Lu 24.1 | Nb 5.58 | Ta 5.30 | Zr 3.79 | Hf 11.0 | Sr 77.8 | Ge 0.56 | As 0.29 | U 0.46

Fig. 10

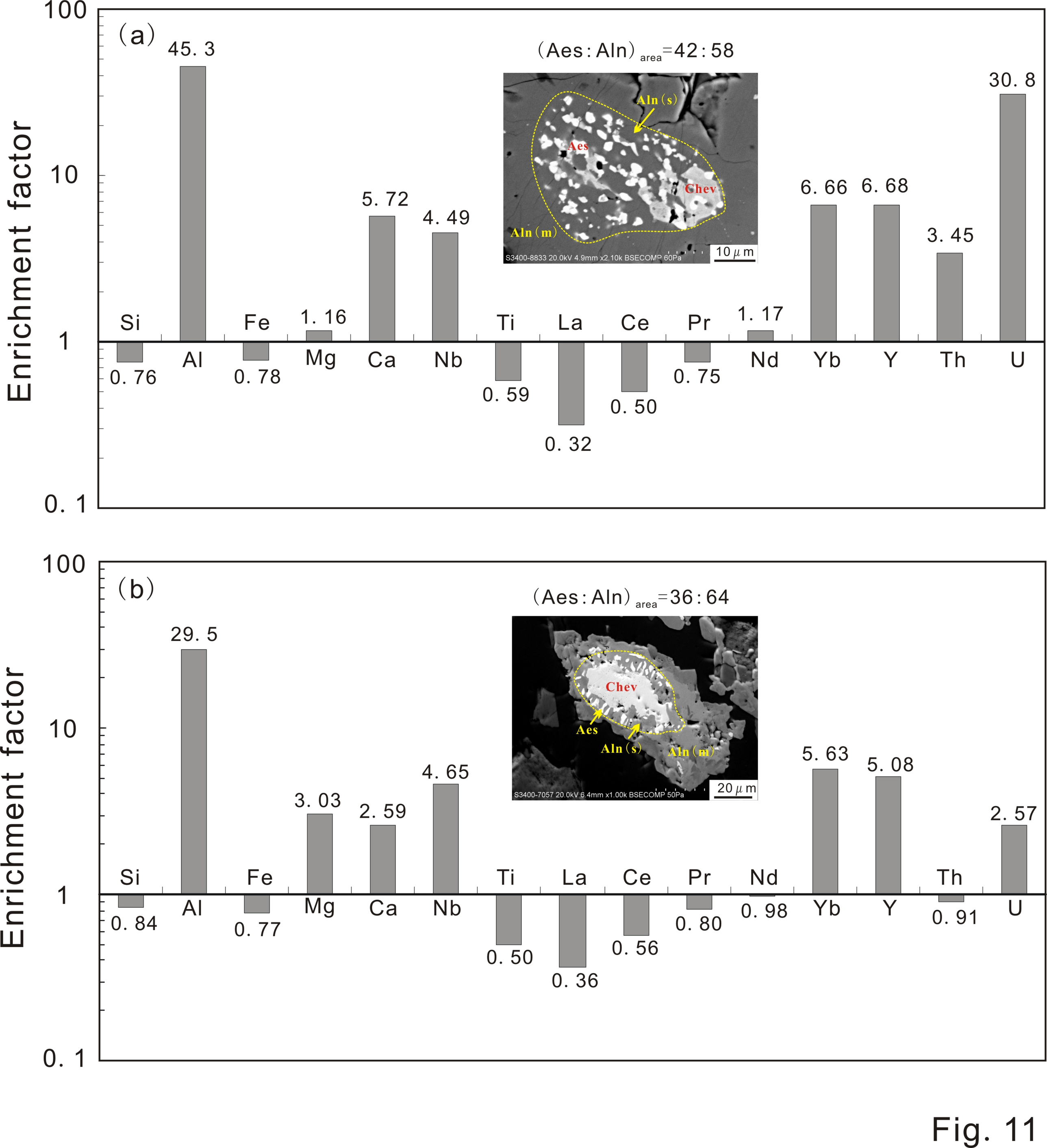
(a)
(Aes:Aln)area=42:58
Aln(s)
Aes
Chev
Aln(m)
S3400-8833 20.0kV 4.9mm x2.10k BSECOMP 60Pa
10 μm
Enrichment factor
100
10
1
0.1
Si 0.76
Al 45.3
Fe 0.78
Mg 1.16
Ca 5.72
Nb 4.49
Ti 0.59
La 0.32
Ce 0.50
Pr 0.75
Nd 1.17
Yb 6.66
Y 6.68
Th 3.45
U 30.8
(b)
(Aes:Aln)area=36:64
Chev
Aes
Aln(s)
Aln(m)
S3400-7057 20.0kV 6.4mm x1.00k BSECOMP 50Pa
20 μm
Enrichment factor
100
10
1
0.1
Si 0.84
Al 29.5
Fe 0.77
Mg 3.03
Ca 2.59
Nb 4.65
Ti 0.50
La 0.36
Ce 0.56
Pr 0.80
Nd 0.98
Yb 5.63
Y 5.08
Th 0.91
U 2.57

Fig. 11

(a) stage Ⅰ: Na alteration

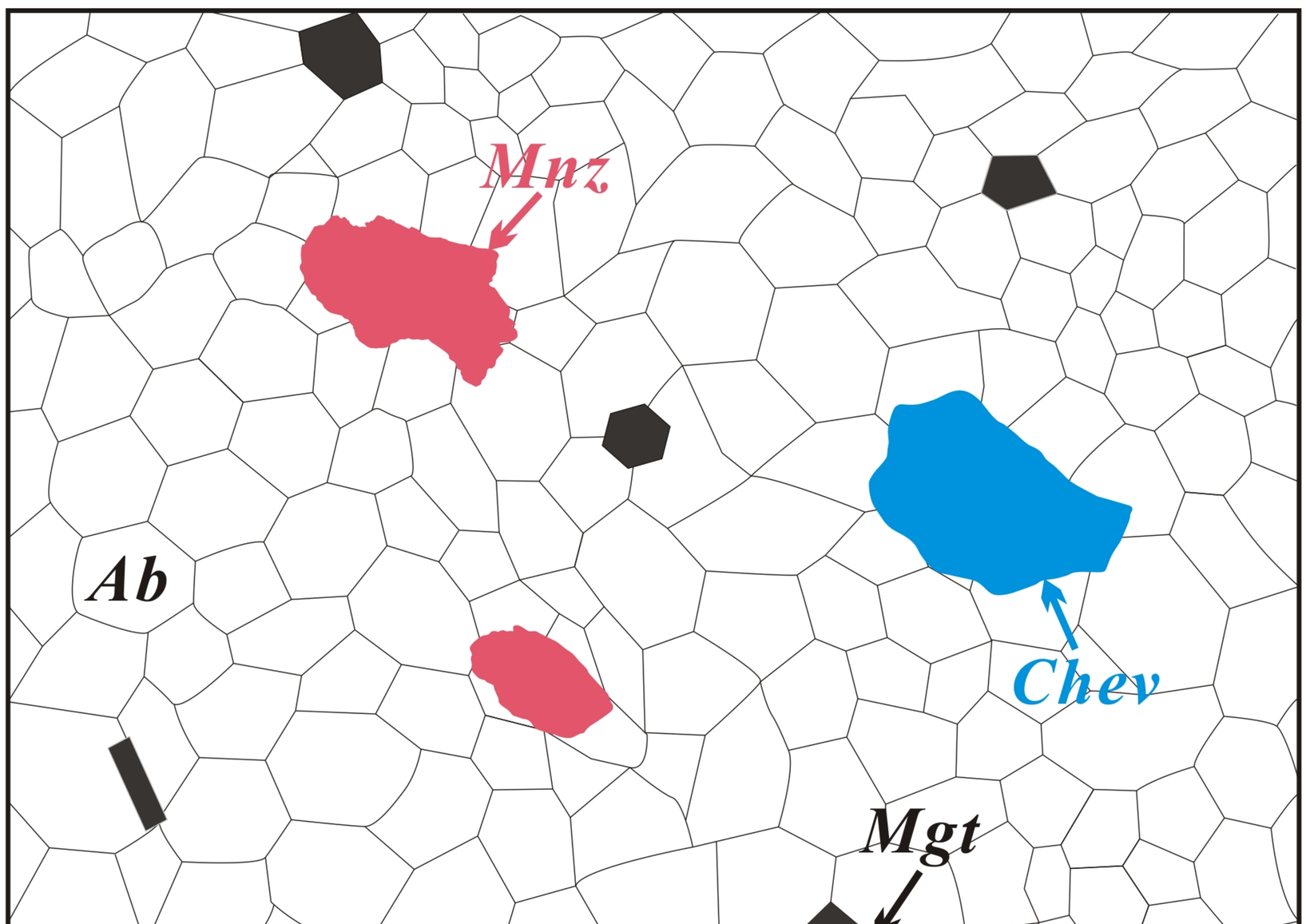

(b) stage Ⅱ: Fe-REE mineralization

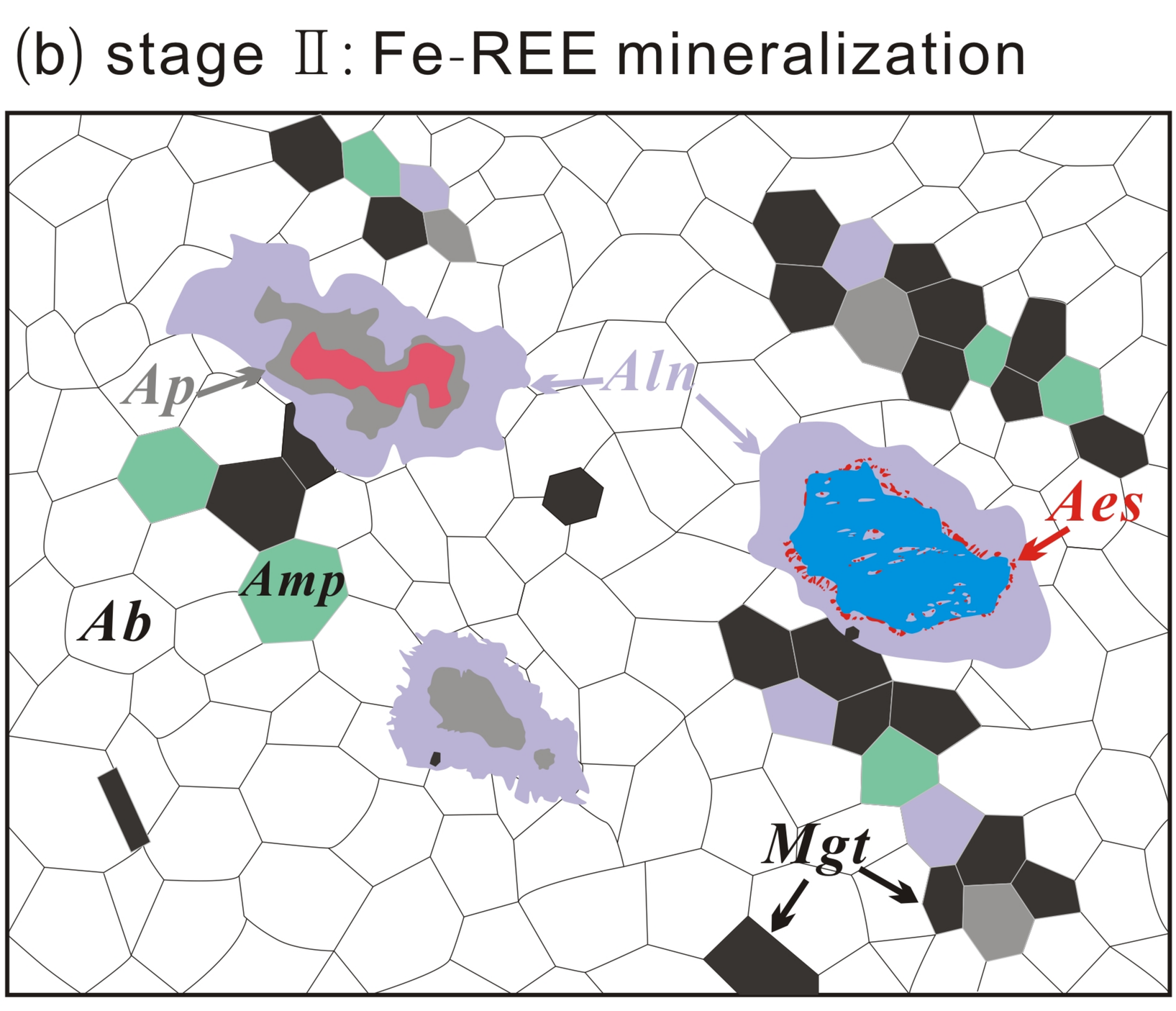

Increasing Ca/Na ratio
Decreasing temperature

(c) stage Ⅲ: Cu-Au mineralization

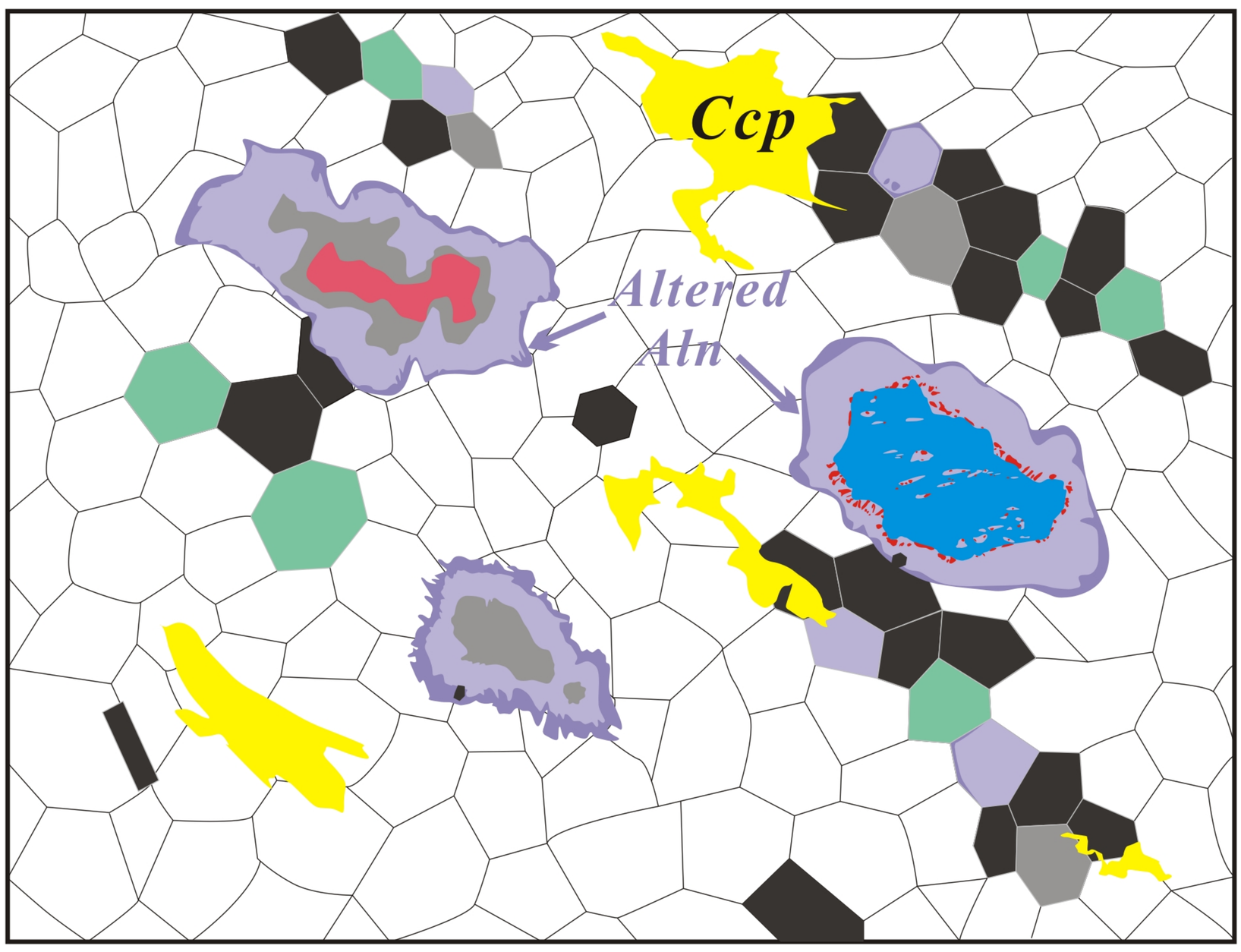

Albite
Monazite-(Ce)
Chevkinite-(Ce)
Allanite-(Ce)
Altered allanite-(Ce)
Magnetite
Fluorapatite
Aeschynite
Amphibole
Chalcopyrite

Fig. 12

Table 1 A list of monazite-(Ce)- and/or chevkinite-(Ce)-bearing samples

Sample	Rock type	Mineralogy
SQ-109	Albitite mass	Stage I: Ab±Mnz±Chev Stage II: Amp(minor) Stage III: Bt±Ccp
SQ-111	Albitite vein	Stage I: Ab±Chev Stage II: Amp±Mgt±Ap Stage III: Bt
SQ-16	Banded ore	Stage I: Ab±Chev Stage II: Mgt+Aln+Amp±Bt Stage III: Ccp+Bt
SQ-18	Massive ore	Stage I: Ab±Chev Stage II: Mgt+Aln+Amp+Bt±Ap Stage III: Ccp±Bt
SQ-19	Banded ore	Stage I: Ab±Chev±Mnz Stage II: Amp±Mgt±Aln Stage III: Ccp+Bt
SQ-25	Massive ore with albitite masses	Stage I: Ab±Chev Stage II: Amp±Mgt±Aln±Bt Stage III: Ccp±Bt
SQ-99	Banded ore	Stage I: Ab+Mnz Stage II: Mgt+Aln+Amp±Bt Stage III: Bt±Ccp
SQ-100	Massive ore	Stage I: Ab±Chev±Mnz Stage II: Mgt+Aln+Amp±Ap Stage III: Ccp+Bt
SQ-101	Banded ore with albitite veins and masses	Stage I: Ab±Chev±Mnz Stage II: Aln±Mgt±Amp±Bt Stage III: Ccp+Bt
SQ-108	Banded ore	Stage I: Ab±Chev Stage II: Mgt+Aln+Amp±Ap Stage III: Ccp+Bt
SQ-110	Banded ore	Stage I: Ab+Chev+Mnz Stage II: Aln(minor) Stage III: Bt±Ccp
LC11-44	Massive ore	Stage I: Ab+Mnz Stage II: Mgt+Aln+Amp±Bt±Ap Stage III: Ccp+Bt

Note: (1) Mineral abbreviations: Ab-albite, Aln-allanite-(Ce), Amp-amphibole, Ap-fluorapatite, Bt-biotite, Ccp-chalcopyrite, Chev-chevkinite-(Ce), Mgt-magnetite, Mnz-monazite-(Ce).
(2) Quartz and minor Ti-, Nb- and U-bearing phases may occur in some samples, but they are not shown in this table.

Table 2 Representative EMP data for minerals

	ommon allanite-(Ce)			**Allanite-(Ce) in corona**			**Allanite-(Ce) mantle around chevkinite-(Ce)**		
Element	Mean(n=23)	Range	Cations	Mean(n=24)	Range	Cations	Mean(n=13)	Range	Cations
P_2O_5	0.01	b.d.l.-0.04	0.001	0.03	b.d.l.-0.09	0.003	0.02	b.d.l.-0.03	0.001
Nb_2O_5	n.d.	n.d.	n.d.	n.d.	n.d.	n.d.	n.d.	n.d.	n.d.
Ta_2O_5	n.d.	n.d.	n.d.	n.d.	n.d.	n.d.	n.d.	n.d.	n.d.
SiO_2	30.08	29.33-30.77	2.900	30.09	29.37-31.42	2.917	29.76	29.01-30.49	2.906
TiO_2	n.d.	n.d.	n.d.	n.d.	n.d.	n.d.	n.d.	n.d.	n.d.
ThO_2	0.05	b.d.l.-0.13	0.001	0.08	b.d.l.-0.20	0.002	0.07	b.d.l.-0.21	0.002
UO_2	0.04	b.d.l.-0.08	0.001	0.04	b.d.l.-0.10	0.001	0.03	b.d.l.-0.08	0.001
Al_2O_3	14.23	12.35-16.40	1.616	14.26	12.70-15.88	1.628	13.35	11.88-14.72	1.535
La_2O_3	8.36	7.17-9.38	0.298	8.77	7.48-10.37	0.314	8.44	7.56-9.10	0.304
Ce_2O_3	13.53	12.64-14.76	0.478	13.59	12.56-14.75	0.482	13.92	13.09-14.40	0.498
Pr_2O_3	0.91	0.36-1.27	0.032	0.92	0.63-1.16	0.033	0.94	0.44-1.07	0.033
Nd_2O_3	1.56	1.28-2.13	0.054	1.73	0.81-2.75	0.060	1.74	1.26-2.26	0.061
Sm_2O_3	n.d.	n.d.	n.d.	n.d.	n.d.	n.d.	n.d.	n.d.	n.d.
Gd_2O_3	n.d.	n.d.	n.d.	n.d.	n.d.	n.d.	n.d.	n.d.	n.d.
Dy_2O_3	n.d.	n.d.	n.d.	n.d.	n.d.	n.d.	n.d.	n.d.	n.d.
Er_2O_3	n.d.	n.d.	n.d.	n.d.	n.d.	n.d.	n.d.	n.d.	n.d.
Yb_2O_3	0.05	b.d.l.-0.19	0.001	0.02	b.d.l.-0.14	0.001	0.04	b.d.l.-0.20	0.001
Y_2O_3	0.06	b.d.l.-0.18	0.003	0.04	b.d.l.-0.13	0.002	0.06	b.d.l.-0.13	0.003
FeO	17.60	16.28-18.91	1.421	17.51	15.47-19.84	1.421	18.83	16.63-20.64	1.540
MnO	0.03	b.d.l.-0.15	0.002	0.03	b.d.l.-0.16	0.003	0.06	b.d.l.-0.15	0.005
MgO	0.84	0.40-1.29	0.121	0.66	0.15-1.24	0.096	0.70	0.38-1.08	0.102
CaO	10.34	9.68-11.34	1.068	9.94	9.26-10.85	1.032	9.52	8.88-10.65	0.996
Na_2O	0.02	b.d.l.-0.14	0.003	0.04	b.d.l.-0.19	0.008	0.06	b.d.l.-0.14	0.012
F	0.19	0.09-0.27		0.17	0.10-0.29		0.18	0.11-0.29	
Cl	0.02	0.01-0.04		0.02	0.01-0.05		0.02	b.d.l.-0.08	
Total	97.84	95.91-99.22	8.000	97.88	95.50-99.26	8.000	97.65	95.29-99.56	8.000

Continued

	Allanite-(Ce) replacing chevkinite-(Ce)			Altered domains in allanite-(Ce)			Common fluorapatite			Fluorapatite in corona		
Element	Mean(n=9)	Range	Cations	Mean(n=15)	Range	Cations	Mean(n=23)	Range	Cations	Mean(n=14)	Range	Cations
P_2O_5	0.02	b.d.l.-0.07	0.001	0.02	b.d.l.-0.04	0.001	40.98	39.58-43.51	2.957	40.82	39.87-41.58	2.954
Nb_2O_5	n.d.	n.d.	n.d.	n.d.	n.d.	n.d.	n.d.	n.d.	n.d.	n.d.	n.d.	n.d.
Ta_2O_5	n.d.	n.d.	n.d.	n.d.	n.d.	n.d.	n.d.	n.d.	n.d.	n.d.	n.d.	n.d.
SiO_2	29.80	29.27-30.15	2.890	33.09	31.19-35.30	2.863	0.28	b.d.l.-0.69	0.024	0.16	b.d.l.-0.47	0.014
TiO_2	n.d.	n.d.	n.d.	n.d.	n.d.	n.d.	n.d.	n.d.	n.d.	n.d.	n.d.	n.d.
ThO_2	0.13	0.02-0.22	0.003	0.03	b.d.l.-0.09	0.001	0.02	b.d.l.-0.09	0.000	0.01	b.d.l.-0.05	0.000
UO_2	0.05	0.01-0.09	0.001	0.22	0.05-0.51	0.004	0.01	b.d.l.-0.05	0.000	0.01	b.d.l.-0.03	0.000
Al_2O_3	13.96	12.93-15.98	1.594	20.84	16.58-22.65	2.122	0.02	b.d.l.-0.26	0.002	0.02	b.d.l.-0.10	0.002
La_2O_3	8.03	7.25-8.55	0.287	3.81	1.94-6.47	0.123	n.d.	n.d.	n.d.	n.d.	n.d.	n.d.
Ce_2O_3	13.34	12.56-13.82	0.474	6.43	3.71-10.41	0.205	n.d.	n.d.	n.d.	n.d.	n.d.	n.d.
Pr_2O_3	0.98	0.82-1.08	0.035	0.39	0.16-0.82	0.012	n.d.	n.d.	n.d.	n.d.	n.d.	n.d.
Nd_2O_3	1.83	1.64-2.17	0.064	0.89	0.52-1.26	0.028	n.d.	n.d.	n.d.	n.d.	n.d.	n.d.
Sm_2O_3	n.d.	n.d.	n.d.	n.d.	n.d.	n.d.	n.d.	n.d.	n.d.	n.d.	n.d.	n.d.
Gd_2O_3	n.d.	n.d.	n.d.	n.d.	n.d.	n.d.	n.d.	n.d.	n.d.	n.d.	n.d.	n.d.
Dy_2O_3	n.d.	n.d.	n.d.	n.d.	n.d.	n.d.	n.d.	n.d.	n.d.	n.d.	n.d.	n.d.
Er_2O_3	n.d.	n.d.	n.d.	n.d.	n.d.	n.d.	n.d.	n.d.	n.d.	n.d.	n.d.	n.d.
Yb_2O_3	0.03	b.d.l.-0.11	0.001	0.02	b.d.l.-0.09	0.000	n.d.	n.d.	n.d.	n.d.	n.d.	n.d.
Y_2O_3	0.07	0.03-0.14	0.004	0.10	b.d.l.-0.23	0.005	n.d.	n.d.	n.d.	n.d.	n.d.	n.d.
FeO	18.53	16.45-20.35	1.504	14.47	13.47-16.84	1.050	0.16	0.03-0.47	0.012	0.12	b.d.l.-0.26	0.009
MnO	0.05	b.d.l.-0.18	0.004	0.05	0.01-0.11	0.004	0.02	b.d.l.-0.04	0.001	0.01	b.d.l.-0.05	0.001
MgO	0.70	0.24-1.43	0.102	0.14	0.05-0.24	0.018	0.01	b.d.l.-0.03	0.001	0.01	b.d.l.-0.02	0.001
CaO	9.85	9.25-10.48	1.023	16.84	13.13-19.08	1.559	55.19	53.96-56.58	5.040	55.35	54.54-56.03	5.070
Na_2O	0.07	b.d.l.-0.14	0.013	0.03	b.d.l.-0.07	0.005	0.02	b.d.l.-0.09	0.003	0.02	b.d.l.-0.09	0.004
F	0.17	0.09-0.26		0.01	b.d.l.-0.06		2.44	1.74-3.46	0.659	3.03	2.55-3.61	0.820
Cl	0.02	0.01-0.04		0.01	b.d.l.-0.02		0.01	b.d.l.-0.05	0.001	0.01	b.d.l.-0.02	0.001
Total	97.57	96.45-99.30	8.000	97.38	94.91-98.97	8.000	98.13	96.21-100.19	8.040	98.31	97.36-99.16	8.055

Continued

	Monazite-(Ce)			Chevkinite-(Ce)			Aeschynite-(Ce)		
Element	Mean(n=21)	Range	Cations	Mean(n=36)	Range	Cations	Mean(n=51)	Range	Cations
P_2O_5	30.08	29.23-30.85	0.995	0.01	b.d.l.-0.07	0.003	0.01	b.d.l.-0.04	0.000
Nb_2O_5	n.d.	n.d.	n.d.	2.61	1.09-5.42	0.251	34.67	21.67-45.95	0.961
Ta_2O_5	n.d.	n.d.	n.d.	0.03	b.d.l.-0.39	0.001	0.13	b.d.l.-1.07	0.002
SiO_2	0.25	0.04-0.47	0.010	18.99	18.59-19.46	4.037	0.14	b.d.l.-1.61	0.009
TiO_2	n.d.	n.d.	n.d.	15.47	11.92-17.25	2.471	22.19	16.01-30.93	1.025
ThO_2	0.26	b.d.l.-0.66	0.002	0.11	b.d.l.-0.33	0.005	0.59	0.02-2.60	0.008
UO_2	0.14	0.04-0.30	0.001	0.10	0.02-0.27	0.005	2.21	0.60-5.01	0.030
Al_2O_3	b.d.l.	b.d.l.-0.03	0.000	0.30	0.07-0.54	0.074	0.02	b.d.l.-0.28	0.001
La_2O_3	23.96	20.72-26.15	0.346	14.98	10.61-16.90	1.175	4.01	1.38-8.16	0.091
Ce_2O_3	37.13	35.94-38.68	0.532	24.85	22.39-27.61	1.934	17.10	8.99-21.67	0.384
Pr_2O_3	2.58	2.26-3.04	0.037	1.92	1.51-2.24	0.149	2.35	1.66-3.52	0.053
Nd_2O_3	4.85	3.89-6.40	0.068	4.69	3.35-6.88	0.356	9.41	5.08-12.28	0.206
Sm_2O_3	n.d.	n.d.	n.d.	n.d.	n.d.	n.d.	0.34	b.d.l.-1.48	0.007
Gd_2O_3	n.d.	n.d.	n.d.	n.d.	n.d.	n.d.	0.57	b.d.l.-1.66	0.012
Dy_2O_3	n.d.	n.d.	n.d.	n.d.	n.d.	n.d.	0.24	b.d.l.-0.96	0.005
Er_2O_3	n.d.	n.d.	n.d.	n.d.	n.d.	n.d.	0.17	b.d.l.-0.58	0.003
Yb_2O_3	0.03	b.d.l.-0.17	0.000	0.05	b.d.l.-0.23	0.003	0.76	0.12-1.58	0.014
Y_2O_3	0.14	0.01-0.58	0.003	0.14	0.01-0.48	0.016	1.08	0.29-3.88	0.035
FeO	0.03	b.d.l.-0.14	0.001	12.67	11.30-13.73	2.255	1.47	0.67-2.91	0.076
MnO	0.00	n.d.	0.000	0.03	b.d.l.-0.08	0.005	b.d.l.	b.d.l.	0.000
MgO	0.01	b.d.l.-0.05	0.001	0.18	0.08-0.32	0.057	b.d.l.	b.d.l.-0.03	0.000
CaO	0.13	b.d.l.-0.52	0.005	1.97	0.86-3.48	0.448	2.35	0.28-6.25	0.154
Na_2O	0.00	n.d.	0.000	0.00	b.d.l.-0.08	0.001	b.d.l.	b.d.l.	0.000
F	0.63	0.50-0.79	0.078	0.44	0.26-0.57	0.295	b.d.l.	b.d.l.-0.05	0.000
Cl	0.05	0.04-0.08	0.004	0.03	0.01-0.09	0.012	0.04	0.02-0.05	0.004
Total	99.99	98.50-101.66	2.001	99.37	98.21-100.99	13.246	99.82	98.00-101.64	3.077

Note: (1) Formula calculation for allanite-(Ce) was based on 12.5 O and 8 cations; for fluorapatite based on 12.5 O; for monazite-(Ce) based on 4 O; for chevkinite-(Ce) based on 22 O and with all Fe as Fe^{2+}; for aeschynite-(Ce) based on 6 O. (2) n.d. denotes not determined; b.d.l. denotes below detection limit. (3) The whole dataset is listed in Supplemental Material.

Table 3 Representative LA-ICP-MS data for minerals

	Common allanite-(Ce)		**Allanite-(Ce) in corona texture**		**Allanite-(Ce) mantled chevkinite-(Ce)**	
	Mean(n=17)	Range	Mean(n=11)	Range	Mean(n=14)	Range
La	71774	62752-88193	75101	61725-88169	71748	57413-84138
Ce	102928	92483-122723	106750	92671-115125	108075	84222-128541
Pr	8063	7310-9292	8531	7409-9174	8897	6823-10588
Nd	20729	18552-22664	22657	18951-25325	24199	18369-28953
Sm	1282	1106-1572	1538	1153-1869	1663	1183-2186
Eu	182	144-271	214	168-294	226	167-355
Gd	473	390-630	603	425-802	603	409-820
Tb	30.4	25.1-43.0	44.6	26.6-66.6	43.8	24.5-63.5
Dy	101	87.6-143	162	93.4-249	157	88.2-235
Ho	14.6	12.8-19.9	23.0	14.0-35.5	22.1	13.1-33.4
Er	34.1	28.0-45.3	50.1	29.5-74.9	49.1	29.9-74.7
Tm	4.59	3.55-6.05	6.52	3.68-10.4	6.54	3.68-10.1
Yb	31.2	22.8-41.3	43.3	24.0-69.4	45.0	23.0-65.8
Lu	4.47	2.92-6.06	6.29	3.71-10.3	6.59	2.72-9.87
Y	374	321-498	581	336-852	552	353-800
Nb	1.22	0.25-4.15	2.97	0.99-7.76	12.2	3.31-43.9
Ta	0.05	b.d.l.-0.10	0.07	0.02-0.18	0.28	0.06-0.84
Ti	3146	770-6523	5957	3229-14470	8313	5160-13501
Zr	3.15	1.09-5.65	3.15	0.91-6.21	3.26	1.50-8.50
Hf	0.12	0.04-0.19	0.17	0.06-0.35	0.22	0.05-0.57
Th	264	121-521	437	180-917	459	287-658
U	158	42.0-332	194	67.8-311	123	43.6-265
Pb	19.8	9.38-39.4	32.9	15.2-66.9	34.3	22.5-48.9
Rb	0.66	b.d.l.-5.06	0.19	b.d.l.-0.33	0.33	b.d.l.-0.81
Sr	121	41.1-262	80.4	33.4-263	105	61.4-230
Ba	1.07	0.05-10.75	0.61	b.d.l.-2.19	0.84	b.d.l.-2.05
Si	n.d.	n.d.	n.d.	n.d.	n.d.	n.d.
Sc	18.7	4.97-51.0	33.5	11.9-67.4	22.1	4.50-46.0
V	118	73.9-165	80.4	44.5-148	112	52.0-190
Cr	25.4	b.d.l.-117	73.6	12.9-118	134	38.7-337
Co	13.1	8.62-19.0	13.9	8.81-21.6	13.3	7.43-23.1
Ni	2.23	0.72-4.04	2.15	0.44-4.64	2.62	b.d.l.-6.01
Cu	0.43	b.d.l.-2.91	0.84	b.d.l.-3.49	0.55	b.d.l.-1.55
Zn	28.2	15.7-38.4	29.2	21.8-44.5	28.8	20.6-33.8
Ga	40.7	27.6-49.7	33.6	31.0-39.6	35.4	29.5-40.7
Ge	171	150-185	187	156-210	196	160-223
As	83.2	74.5-97.9	90.2	75.8-104	97.4	84.8-120
W	0.07	b.d.l.-0.29	0.22	0.05-0.92	0.37	b.d.l.-0.77
Sn	43.1	16.1-66.0	45.8	29.7-92.5	52.4	36.3-88.9

Continued

	Common fluorapatite		Fluorapatite in corona textures	
	Mean(n=9)	Range	Mean(n=13)	Range
La	1611	466-2467	1590	869-3116
Ce	4467	1271-6811	3895	2207-6878
Pr	639	174-991	511	302-965
Nd	2884	774-4533	2237	1301-4382
Sm	489	131-851	356	160-768
Eu	104	31.4-189	77.2	35.9-185
Gd	342	97.8-645	263	104-544
Tb	43.3	12.7-86.7	32.8	13.0-65.8
Dy	241	78.2-492	184	75.7-350
Ho	50.1	18.2-102	38.6	14.9-66.4
Er	146	61.4-299	111	40.9-177
Tm	22.5	10.5-45.9	16.8	5.80-28.0
Yb	159	77.5-330	115	40.0-195
Lu	24.7	12.1-51.7	16.7	5.96-28.8
Y	1460	576-2901	1166	406-2057
Nb	0.31	0.09-0.62	7.44	0.06-65.2
Ta	0.01	b.d.l.-0.02	0.56	b.d.l.-6.08
Ti	1.27	b.d.l.-7.10	28.8	b.d.l.-202
Zr	0.64	0.11-1.31	18.4	b.d.l.-236
Hf	0.02	b.d.l.-0.04	0.47	b.d.l.-5.84
Th	7.29	0.58-16.9	11.4	0.44-53.8
U	98.0	20.4-246	69.0	10.4-208
Pb	2.22	1.53-2.53	2.25	1.30-3.24
Rb	0.28	0.07-1.03	0.50	0.07-4.74
Sr	787	493-1111	701	492-906
Ba	0.23	0.02-0.79	1.32	0.07-8.64
Si	2950	1090-4939	3116	1084-5900
Sc	0.33	0.12-0.71	0.47	0.07-1.81
V	0.65	0.22-1.49	0.44	0.16-1.08
Cr	0.37	b.d.l.-1.34	0.23	b.d.l.-1.69
Co	0.07	b.d.l.-0.23	0.15	b.d.l.-0.61
Ni	0.34	b.d.l.-1.01	0.36	b.d.l.-0.94
Cu	0.30	b.d.l.-1.72	21.80	b.d.l.-279
Zn	0.22	b.d.l.-0.56	0.90	b.d.l.-1.99
Ga	0.42	b.d.l.-0.73	0.52	0.11-1.60
Ge	21.5	6.33-36.4	17.5	8.55-35.4
As	123	40.4-316	60.9	13.2-154
W	1.17	0.31-2.19	1.47	0.15-4.37
Sn	0.15	b.d.l.-0.41	0.52	b.d.l.-3.94

Continued

	Monazite-(Ce)		Chevkinite-(Ce)	
	Mean(n=13)	Range	Mean(n=16)	Range
La	222221	213979-234630	131117	117385-145552
Ce			202708	184903-220674
Pr	25899	25124-26611	17369	15602-19154
Nd	69009	64737-73077	48784	43125-53563
Sm	4350	3843-5181	3470	3007-3973
Eu	608	489-791	553	439-807
Gd	1623	1485-2011	1323	1187-1668
Tb	99.1	83.7-142	104	86.2-138
Dy	315	241-511	396	314-555
Ho	37.4	26.4-65.6	58.5	42.7-81.7
Er	60.9	43.9-108	130	90.1-169
Tm	4.36	3.06-7.73	18.7	13.3-23.5
Yb	14.7	9.25-25.9	152	104-190
Lu	1.17	0.68-1.96	25.3	19.1-32.1
Y	947	705-1596	1325	955-1791
Nb	0.47	0.13-0.76	20495	11905-34815
Ta	0.01	b.d.l.-0.02	207	89.2-357
Ti	0.23	b.d.l.-1.46	n.d.	n.d.
Zr	0.99	0.64-1.47	690	153-1290
Hf	0.02	b.d.l.-0.08	28.4	10.6-53.8
Th	1250	337-2420	1042	562-1899
U	935	340-1536	1437	577-2265
Pb	58.7	16.9-110	70.5	40.0-116
Rb	0.10	b.d.l.-0.54	0.28	0.05-0.90
Sr	11.30	3.89-55.4	261	125-674
Ba	0.15	b.d.l.-0.75	17.1	2.26-73.5
Si	n.d.	n.d.	n.d.	n.d.
Sc	0.04	b.d.l.-0.11	133	61.6-267
V	5.67	1.83-18.4	159	91.2-273
Cr	0.18	b.d.l.-0.91	246	56.6-625
Co	0.05	b.d.l.-0.20	4.55	2.93-7.38
Ni	0.13	b.d.l.-0.70	0.62	b.d.l.-1.41
Cu	15.3	0.13-135	2.51	b.d.l.-11.60
Zn	0.25	b.d.l.-1.17	5.61	3.28-8.06
Ga	34.6	32.3-36.7	23.9	18.6-29.2
Ge	527	488-581	368	317-430
As	466	308-760	190	154-238
W	2.50	0.98-4.09	280	193-358
Sn	0.11	b.d.l.-0.58	241	122-768

Note: (1) n.d. denotes not determined; b.d.l. denotes below detection limit. (2) The whole dataset is listed in Supplemental Material.

Table 4 Results of mass balance calculations for the alteration of monazite-(Ce)

	Mnz	Ap	Aln	Ap-Aln mixed region	Normalized composition	Enrichment factor
$[Ap:Aln]_{area}$ = 21:79						
EMPA data (wt.%)						
Spot No.	SQ99-7	SQ99-4	SQ99-4			
P_2O_5	29.64	41.58	0.02	7.50	18.98	0.64
SiO_2	0.22	0.25	29.97	24.62	62.32	
Al_2O_3	0.00	0.01	15.88	13.03	32.97	
La_2O_3	23.52	0.14	7.48	6.15	15.58	0.66
Ce_2O_3	37.58	0.31	12.56	10.36	26.22	0.70
Pr_2O_3	2.50	0.04	1.00	0.83	2.10	0.84
Nd_2O_3	5.92	0.15	1.76	1.47	3.71	0.63
FeO	0.10	0.26	17.84	14.67	37.14	
MnO	0.00	0.01	0.00	0.00	0.00	
MgO	0.02	0.00	0.88	0.72	1.83	
CaO	0.05	54.77	10.84	18.75	47.45	
Na_2O	0.00	0.00	0.07	0.06	0.14	
LA-ICP-MS data (ppm)						
Spot No.	SQ-99-5	SQ-99-3	SQ-99-4			
Sm	4289	160	1623	1360	3441	0.80
Eu	650	35.3	294	247	626	0.96
Gd	1601	104	675	572	1447	0.90
Tb	100	13.0	57.7	49.6	126	1.25
Dy	324	92.2	223	199	504	1.56
Ho	38.8	24.9	31.0	29.9	76	1.95
Er	63.6	96.1	65.1	70.6	179	2.81
Tm	4.62	17.6	7.95	9.69	24.5	5.31
Yb	16.1	125	52.2	65.3	165	10.3
Lu	1.21	17.2	7.56	9.30	23.5	19.4
Y	967	876	769	788	1995	2.06
Nb	0.34	0.22	1.26	1.08	2.72	8.0
Ta	0.01	0.01	0.03	0.03	0.08	11.9
Ti	0.08	1.13	3647	2991	7569	96929
Zr	0.64	0.18	1.63	1.37	3.47	5.45
Hf	0.04	0.02	0.06	0.06	0.14	3.43
Th	972	1.68	468	384	972	1.00
U	1118	26.8	258	217	548	0.49
Pb	42.8	2.38	35.4	29.4	75	1.74
Rb	0.14	0.07	0.33	0.29	0.73	5.25
Sr	5.79	736	80.5	198	502	87
Ba	0.05	0.40	0.48	0.46	1.17	25.8
Ge	488	9.60	169	140	355	0.73
As	369	30.2	81.9	72.6	184	0.50

Continued

	Mnz	Ap	Aln	Ap-Aln mixed region	Normalized composition	Enrichment factor
[Ap:Aln]$_{area}$ = 31:69						
EMPA data (wt.%)						
Spot No.	sq-99-1	sq-99-1	sq-99-1			
P_2O_5	30.52	41.36	0.00	11.58	22.80	0.75
SiO_2	0.18	0.00	31.03	22.34	43.98	
Al_2O_3	0.00	0.01	14.47	10.42	20.52	
La_2O_3	25.15	0.10	10.37	7.50	14.76	0.59
Ce_2O_3	37.25	0.26	13.67	9.92	19.52	0.52
Pr_2O_3	2.65	0.04	0.78	0.57	1.13	0.43
Nd_2O_3	4.00	0.15	0.94	0.72	1.42	0.35
FeO	0.00	0.07	17.40	12.54	24.70	
MnO	0.00	0.00	0.00	0.00	0.00	
MgO	0.04	0.00	0.15	0.11	0.21	
CaO	0.03	55.79	9.58	22.52	44.34	
Na_2O	0.00	0.04	0.01	0.02	0.03	
LA-ICP-MS data (ppm)						
Spot No.	SQ-99-1	SQ-99-Ap1	SQ-99-1			
Sm	4158	199	1869	1401	2759	0.66
Eu	569	35.9	206	158	312	0.55
Gd	1485	132	802	614	1210	0.81
Tb	89.6	14.2	66.6	51.9	102	1.14
Dy	288	75.7	249	201	395	1.37
Ho	34.3	16.0	35.5	30.0	59.1	1.72
Er	55.5	46.1	74.9	66.8	132	2.37
Tm	4.08	7.47	10.4	9.59	18.9	4.63
Yb	14.1	49.9	69.4	63.9	126	8.90
Lu	1.14	6.96	10.3	9.33	18.4	16.08
Y	851	466	852	744	1465	1.72
Nb	0.45	0.06	0.99	0.73	1.44	3.23
Ta	0.01	0.01	0.04	0.03	0.06	6.03
Ti	0.12	0.33	3923	2825	5562	45271
Zr	1.06	0.31	3.02	2.26	4.45	4.20
Hf	0.02	0.00	0.16	0.12	0.23	10.08
Th	1300	0.44	917	660	1300	1.00
U	1101	10.4	239	175	345	0.31
Pb	56.8	2.34	66.9	48.8	96.1	1.69
Rb	0.08	0.14	0.14	0.14	0.28	3.70
Sr	6.65	684	43.3	223	439	66.01
Ba	0.00	0.07	0.40	0.31	0.61	
Ge	508	8.55	197	144	284	0.56
As	391	121	94.9	102	201	0.51

Continued

	Mnz	Ap	Aln	Ap-Aln mixed region	Normalized composition	Enrichment factor
$[Ap:Aln]_{area}$ = 39:61						
EMPA data (wt.%)						
Spot No.	SQ110-1	SQ110-1	SQ110-5			
P_2O_5	29.57	40.40	0.01	14.15	35.06	1.19
SiO_2	0.25	0.40	30.40	19.90	49.31	
Al_2O_3	0.03	0.10	15.12	9.86	24.44	
La_2O_3	24.79	0.22	8.15	5.37	13.31	0.54
Ce_2O_3	36.28	0.53	13.02	8.65	21.43	0.59
Pr_2O_3	2.59	0.06	0.91	0.61	1.52	0.59
Nd_2O_3	6.30	0.26	2.62	1.79	4.44	0.70
FeO	0.14	0.26	16.00	10.49	25.99	
MnO	0.00	0.00	0.07	0.04	0.11	
MgO	0.00	0.01	0.63	0.42	1.03	
CaO	0.14	54.54	10.63	26.00	64.43	
Na_2O	0.00	0.00	0.00	0.00	0.01	
LA-ICP-MS data (ppm)						
Spot No.	SQ-110-2	SQ-110-1	SQ-110-2			
Sm	4028	247	1564	1103	2733	0.68
Eu	578	53.7	200	149	369	0.64
Gd	1645	181	575	437	1083	0.66
Tb	97.3	26.1	42.4	36.7	90.9	0.93
Dy	298	178	157	164	407	1.37
Ho	35.5	42.7	22.0	29.3	72.5	2.04
Er	59.7	134	47.1	77.6	192	3.22
Tm	4.24	21.1	5.93	11.2	27.9	6.57
Yb	14.3	139	40.7	75.2	186	13.0
Lu	1.14	19.9	6.41	11.1	27.6	24.1
Y	983	1302	547	811	2010	2.05
Nb	0.48	0.57	1.34	1.07	2.66	5.58
Ta	0.02	0.02	0.05	0.04	0.10	5.30
Ti	0.82	0.05	3658	2377	5891	7228
Zr	1.17	0.10	2.69	1.79	4.43	3.79
Hf	0.03	0.02	0.16	0.11	0.28	10.97
Th	337	53.8	180	136	337	1.00
U	1155	208	218	215	532	0.46
Pb	16.9	1.57	15.2	10.4	25.8	1.53
Rb	0.10	0.16	0.14	0.15	0.37	3.58
Sr	9.94	770	65.0	312	773	77.8
Ba	0.09	0.36	0.00	0.13	0.32	3.46
Ge	536	18.9	177	122	302	0.56
As	520	17.6	83.0	60.1	149	0.29

Note: (1) Mnz denotes monazite-(Ce); Ap denotes fluorapatite; Aln denotes allanite-(Ce). (2)The contents of La_2O_3, Ce_2O_3, Pr_2O_3 and Nd_2O_3 for fluorapatite are LA-ICP-MS data.

Table 5 Results of mass balance calculations for the alteration of chevkinite-(Ce)

Element	Chev	Aln	Aes	Aln-Aes mixed region	Enrichment factor
$[Chev:Aes]_{area}$ = 42:58					
Spot No.	SQ-18-6	SQ-18-2	Average of SQ-18-5, SQ-18-6 and SQ-18-7		
P_2O_5	0.02	0.01	0.01	0.01	
Nb_2O_5	3.27	n.d.	36.66	14.66	4.49
Ta_2O_5	0.02	n.d.	0.00	0.00	
SiO_2	18.85	29.69	0.14	14.30	0.76
TiO_2	14.24	n.d.	20.90	8.36	0.59
ThO_2	0.10	0.18	0.62	0.33	3.45
UO_2	0.03	0.07	2.15	0.89	30.80
Al_2O_3	0.14	12.93	0.00	6.21	45.31
La_2O_3	16.77	8.01	3.63	5.29	0.32
$Ce2O_3$	26.04	13.16	16.58	12.95	0.50
$Pr2O_3$	1.86	1.08	2.16	1.38	0.75
Nd_2O_3	3.92	1.78	9.37	4.60	1.17
Sm_2O_3	n.d.	n.d.	0.50		
Gd_2O_3	n.d.	n.d.	0.93		
Dy_2O_3	n.d.	n.d.	0.42		
Er_2O_3	n.d.	n.d.	0.17		
Yb_2O_3	0.06	0.00	1.03	0.41	6.66
Y_2O_3	0.08	0.04	1.33	0.55	6.68
FeO	13.41	20.35	1.59	10.40	0.78
MnO	0.04	0.10	0.00	0.05	1.19
MgO	0.19	0.46	0.00	0.22	1.16
CaO	1.02	10.15	2.37	5.82	5.72
Na_2O	0.00	0.00	0.00	0.00	
F	0.53	0.13	0.00	0.06	
Cl	0.03	0.02	0.04	0.02	
Total	100.38	98.07	100.59	87.31	

Continued

Element	Chev	Aln	Aes	Aln-Aes mixed region	Enrichment factor
[Chev:Aes]$_{area}$ = 36:64					
Spot No.	SQ-110-2	SQ-110-2	Average of SQ-110-3, SQ-110-4 and SQ-110-5		
P_2O_5	0.00	0.00	0.00	0.00	
Nb_2O_5	2.46	n.d.	32.69	11.44	4.65
Ta_2O_5	0.00	n.d.	0.28	0.10	
SiO_2	18.59	30.15	0.03	15.69	0.84
TiO_2	16.77	n.d.	23.75	8.31	0.50
ThO_2	0.19	0.02	0.46	0.17	0.91
UO_2	0.27	0.03	1.97	0.70	2.57
Al_2O_3	0.25	13.92	0.00	7.24	29.54
La_2O_3	15.49	8.08	4.14	5.65	0.36
$Ce2O_3$	23.44	13.18	18.09	13.19	0.56
$Pr2O_3$	1.72	0.95	2.54	1.38	0.80
Nd_2O_3	4.63	2.06	9.89	4.53	0.98
Sm_2O_3	n.d.	n.d.	0.15		
Gd_2O_3	n.d.	n.d.	0.52		
Dy_2O_3	n.d.	n.d.	0.22		
Er_2O_3	n.d.	n.d.	0.17		
Yb_2O_3	0.06	0.03	0.85	0.32	5.63
Y_2O_3	0.08	0.06	1.10	0.42	5.08
FeO	11.66	16.45	1.18	8.97	0.77
MnO	0.06	0.06	0.00	0.03	0.57
MgO	0.14	0.83	0.00	0.43	3.03
CaO	2.34	10.48	1.75	6.06	2.59
Na_2O	0.00	0.04	0.00	0.02	
F	0.45	0.18	0.00	0.09	
Cl	0.06	0.01	0.04	0.02	
Total	98.45	96.45	99.82	85.09	

Note: Chev denotes chevkinite-(Ce), Aln denotes allanite-(Ce), Aes denotes aeschynite-(Ce).